LIVER SEGMENTATION IN 3D CT DATA

by

Serkan Çimen

B.S., Electrical and Electronics Engineering, Boğaziçi University, 2008

Submitted to the Institute for Graduate Studies in
Science and Engineering in partial fulfillment of
the requirements for the degree of
Master of Science

Graduate Program in Electrical and Electronics Engineering
Boğaziçi University
2011

LIVER SEGMENTATION IN 3D CT DATA

APPROVED BY:

Assoc. Prof. Burak Acar (Thesis Supervisor)	.....
Prof. Ayşın Baytan Ertüzün	.....
Assist. Prof. Mehmet Burçin Ünlü	.....

DATE OF APPROVAL: 05.09.2011

ACKNOWLEDGEMENTS

I would like to thank to my thesis supervisor Assoc. Prof. Burak Acar for his guidance during the preparation of this thesis. Enjoyable technical discussions with him always showed the right steps that have to be taken.

I would also like to thank everyone at the Pattern Recognition Lab of the Friedrich-Alexander University of Erlangen-Nuremberg for their hospitality and friendship. Especially, I am grateful to Andreas Wimmer for teaching almost everything about Insight Toolkit in a short period of time.

I also want to thank friends in Bogazici University Speleological Society. Caving with them always helped to regain my motivation.

ABSTRACT

LIVER SEGMENTATION IN 3D CT DATA

Segmentation of liver from 3D abdominal CT data is the basis of analysis of liver which is required to aid diagnosis and treatment of liver cancer. However, common clinical practice for liver segmentation relies on manual segmentation of CT images by the help of radiologist. Generally, this procedure is tedious and time-consuming. Therefore, fast and robust and accurate methods must be devised to automate liver segmentation process. There is a vast literature for automatic, semi-automatic and interactive liver segmentation methods based on various computer vision algorithms. Each of these methods possess some limitations due to highly varying structure of liver. In this thesis, we propose a semi-automatic liver segmentation algorithm based on an effective combination of intensity distribution modeling, probabilistic atlases (PA) and graph cuts. Major contribution of this work is twofold. First of all, a novel PA construction methodology is proposed based on convex hulls of rough initial segmentation and reference manual delineations. Secondly, a new strategy to improve implicit gray level appearance models is proposed. In addition to that, we explain how to embed PA, gray level appearance models into graph cuts. The effectiveness of proposed algorithm was demonstrated in clinical CT images. Evaluation scores show that proposed method provides results comparable with manual segmentation of a human who has adequate training in liver segmentation.

ÖZET

3D BT DATASINDA KARACİĞER BÖLÜTLEMESİ

Karın bölgesinin üç boyutlu bilgisayarlı tomografi görüntüsünde karaciğer bölütlemesi, karaciğer kanserinin teşhis ve tedavisine yardımcı olmak için gerekli olan karaciğer analizinin temelini oluşturur. Karaciğeri bölütlemek için kullanılan yaygın klinik prosedür, radyologların elle yaptığı bölütlemelere dayanır. Dolayısıyla, zahmetli ve zaman alan bu prosedürün hızlı ve hatasız methodlar geliştirerek otomatik hale getirilmesi gerekmektedir. Literatürde, bilgisayarlı görme algoritmalarına dayanan otomatik, yarı otomatik ve etkileşimli karaciğer bölütlemesi üzerine çok sayıda yöntem bulunmaktadır. Karaciğerin yüksek derecede çeşitlilik gösteren yapısı nedeniyle, bu yöntemlerin her biri bir takım sorunlara sahiptir. Bu tezde, parlaklık dağılımı modellemesi, olasılıksal atlas ve grafik parçalama metodlarının birleşimine dayanan yarı otomatik bir karaciğeri bölütleme algoritması sunulmuştur. Önerilen metodun iki temel katkısı bulunmaktadır. İlk olarak, kaba ön bölütleme ve elle yapılan bölütlemelerin dışbükey zarflarının kullanımına dayalı özgün bir olasılıksal atlas oluşturma yöntemi geliştirilmiştir. İkinci olarak, parlaklık değeri görünüm modellerini geliştiren yeni bir yol uygulanmıştır. Bunlara ek olarak, olasılıksal atlas ve parlaklık değeri görünüm modellerinin grafik parçalama metodunun içine nasıl katılacağı anlatılmıştır. Önerilen metodun etkinliği klinikte kullanılan BT görüntüleri kullanılarak değerlendirilmiş ve methodun bu konuda yeterli bir eğitim almış bir insan tarafından yapılmış bölütlemelerle kıyaslanabilir düzeyde sonuç verdiği tespit edilmiştir.

TABLE OF CONTENTS

ACKNOWLEDGEMENTS . . . iii
ABSTRACT . . . iv
ÖZET . . . v
LIST OF FIGURES . . . viii
LIST OF TABLES . . . xii
LIST OF SYMBOLS . . . xiii
LIST OF ACRONYMS/ABBREVIATIONS . . . xvii
1. INTRODUCTION . . . 1
1.1. Liver Anatomy . . . 3
1.2. Problem Definition and Proposed Solution . . . 5
1.3. Literature Review on Liver Segmentation . . . 7
2. BACKGROUND ON EMPLOYED GENERIC METHODS . . . 19
2.1. The Gaussian Mixture Models and the Expectation Maximization Algorithm . . . 19
2.2. Structure Preserving Diffusion Filters . . . 24
2.2.1. Edge Enhancing Diffusion Filter . . . 27
2.3. Graph Cuts . . . 30
2.3.1. Basic Definitions and Formulation . . . 32
2.3.2. Segmentation Energy and Optimum Solution by Graph Cuts . . . 34
2.3.3. Relation to Markov Random Fields . . . 38
3. SEGMENTATION OF 3D CT DATA . . . 42
3.1. Initial Segmentation via Adaptive Thresholding . . . 44
3.2. Probabilistic Atlas Construction . . . 50
3.3. Graph Building . . . 55
3.3.1. The Intensity Term . . . 57
3.3.2. The Probabilistic Atlas Term . . . 59
3.3.3. Boundary Term . . . 60
4. EXPERIMENTS AND RESULTS . . . 69

4.1. Evaluation Methodology 69
4.2. Image Data Sets 73
4.3. Results 74
5. DISCUSSION 79
6. CONCLUSION 85
APPENDIX A: RESULTS ON M1 DATA SET 87
APPENDIX B: RESULTS ON M2 DATA SET 91
REFERENCES 95

LIST OF FIGURES

Figure 1.1. Examples of difficulties of liver segmentation: Ambiguous boundary between liver and (a) stomach, (b) heart; (c) tumor that must be included in segmentation; (c)-(d) highly varying liver shape. . . 2

Figure 1.2. Superior surface of liver. 3

Figure 1.3. Inferior surface of liver. 4

Figure 1.4. Posterior surface of liver. 5

Figure 2.1. Histogram of the samples drawn from a three component GMM. The true Gaussian components are shown in red while the estimations are shown in green after (a) 40, (b) 80 EM iterations. . . 20

Figure 2.2. Expectation Maximization Algorithm. 25

Figure 2.3. Restoration properties of diffusion filters. (a) Test Image, (b) Linear Diffusion, (c) Nonlinear isotropic diffusion, (d) Edge Enhancing Diffusion. 29

Figure 2.4. A simple s/t graph and an example segmentation for a 3×3 image. 32

Figure 3.1. The flowchart of liver segmentation algorithm. 43

Figure 3.2. The flowchart of initial segmentation via adaptive thresholding. . . 45

Figure 3.3. An example of bounding box. Bounding box is described by red lines in (a). A closer look into bounding box is given in (b). 46

Figure 3.4. Effect of edge enhancing diffusion. (a) Before and (b) after edge enhancing diffusion is applied. 47

Figure 3.5. An example of GMM estimates. Estimates are shown in red with corresponding labels above. 49

Figure 3.6. Results after adaptive thresholding and morphological operations. (a) and (c) show adaptive thresholding results. (b) and (d) show the results obtained after morphological operations. 51

Figure 3.7. The flowchart of probabilistic atlas construction. 53

Figure 3.8. An example of the pseudo-convex hull. (a) Initial segmentation and (b) pseudo-convex hull of initial segmentation. 55

Figure 3.9. An example PA constructed with proposed method. (a) Original image and (b) corresponding PA. 56

Figure 3.10. Profiles sampled from the liver boundary. Mean profile is given in red. 62

Figure 3.11. Edge detection failure due to tumor. (a) Liver image and (b) Edge probabilities. 63

Figure 3.12. Normals defined by (a) SDF and (b) solution of the poisson equation. 64

Figure 3.13. Vectors and angles used in boundary term definition. 67

Figure 4.1. Segmentation results for (a) case 1 and (b) case 16. Reference segmentation outline is given in red and segmentation results of our method is given in blue. 77

Figure 5.1. Undersized PA. The outline of the manual segmentation is given by red contour. 80

Figure 5.2. Convex hull computation failure. 80

Figure 5.3. Segmentation failure in left lobe of the liver. The green circle marks the missed part in the left lobe of the liver. 81

Figure 5.4. Part of the tumor inside green contour is missed. 82

Figure 5.5. Boundary probability assignments using (a) SDF and (b) Poisson equation. Segmentation results employing results of (a) and (b) is given in (c) and (d) respectively. 83

Figure 5.6. Boundary probability assignments using (a) noisy and (b) smoothed profiles. 84

Figure A.1. Results on M1 data set. 87

Figure A.1. Results on M1 data set cont. 88

Figure A.1. Results on M1 data set cont. 89

Figure A.1. Results on M1 data set cont. 90

Figure B.1. The results of our method and five top ranking automatic or semi-automatic methods on case 1 of M2 data set. 92

Figure B.2. The results of our method and five top ranking automatic or semi-automatic methods on case 3 of M2 data set. 93

Figure B.3. The results of our method and five top ranking automatic or semi-automatic methods on case 6 of M2 data set. 94

LIST OF TABLES

Table 2.1. Edge weights for graph $\mathcal{G}$. 37

Table 3.1. Edge weights for graph $\mathcal{G}$ according to our proposal. 67

Table 4.1. Segmentation evaluation scores on M1 data set. 76

Table 4.2. Top ranking methods participated in liver segmentation competition of "3D Segmentation in the clinic: a Grand Challenge" workshop. These results are achieved in M2 data set. 77

LIST OF SYMBOLS

A	Assignment Vector
A_p	Assignment to point p
$\hat{A}$	Optimal assignment vector
B	Boundary term
B_{pq}	Boundary penalty between pixels p and q
$\mathcal{B}$	Set of background hard constraints
c	Clique
C_i	Set of i-site cliques
d_i	ith eigenvalue of diffusion tensor
D	Diffusion tensor
e	An arbitrary edge in graph
e_i	ith eigenvalue of structure tensor
E	Energy function
$E_{boundary}$	Boundary energy
$E_{regional}$	Regional energy
E_{prior}	Spatial prior energy
$\mathcal{E}$	Set of edges
F	Set of background random variables
F_p	Random variable defined for pixel p
g	Monotonically decreasing function
$\mathcal{G}$	Graph
h	Spatial unit
H	Linear transformation
I	Image
J	Structure tensor
I_0	Initial Image
L_n	nth manual delineation
$\mathcal{L}$	Set of labels

$\mathcal{M}$	Neighborhood for a set of points
$\mathcal{N}$	Gaussian function
N_k	Effective number of points assigned to Gaussian component k
$\mathcal{O}$	Set of foreground hard constraints
P	Probability function
P_b	Boundary probability
P_v	Probabilistic atlas
$\widehat{P}_v$	Constrained probabilistic atlas
$\mathcal{P}$	Arbitrary set of data elements
R	Regional term
R_p	Regional penalty for point p
S	Source node
$\mathcal{S}$	Arbitrary open region
$\overline{\mathcal{S}}$	Exterior of open region S
$\partial\mathcal{S}$	Boundary of open region S
t	time variable
T	Sink node
T_i	Affine transform for ith manual delineation
$\mathcal{T}$	Open sphere
$\partial\mathcal{T}$	Surface of open sphere $\mathcal{T}$
U	Prior *or* likelihood energy
v_i	ith eigenvector of structure tensor
v_{pq}	vector pointing from pixel p to q
V	Potential function
V_c	Potential function for clique c
$\mathcal{V}$	Set of vertices
w_i	Weight of edge i
Y	Subset of edges
$\hat{Y}$	Feasible cut
$\boldsymbol{z}$	Latent variable vector
z_k	kth element of latent variable vector

Z	Normalizing constant
α	Parameter of monotonically decreasing function
γ	Responsibility function
Δ	Laplacian operator
ϵ_i	Error for measure i
$\overline{\epsilon}_i$	Average user error for measure i
ζ_1	Weight of regional term
ζ_2	Weight of probabilistic atlas term
η	Arbitrary constant
θ_{ini}	Convex hull of initial segmentation
θ_n	Convex hull of nth manual delineation
θ_{pq}	Angle between $\nabla\varphi$ and v_{pq}
Θ	Final score
Θ_i	Score of ith measure
κ	Curvature
λ	Parameter of monotonically decreasing function
Λ	Lagrange multiplier
μ	Mean value of Gaussian function
ν	Lorentzian error norm
ξ	Robust scale of Lorentzian error norm
π	Mixing coefficient of Gaussian function
ρ	Scale of structure tensor
σ	Standard deviation of Gaussian function
Σ	Covariance matrix of Gaussian function
τ	Threshold value
ϕ	Signed distance function
Φ	Flux
φ	Poisson equation solution
Ω	Arbitrary finite grid
$\partial\Omega$	Boundary of Ω

$\overline{\Omega}$	Exterior of Ω

LIST OF ACRONYMS/ABBREVIATIONS

2D	Two Dimensional
3D	Three Dimensional
ASD	Average Symmetric Surface Distance
CT	Computed Tomography
DOF	Degrees of Freedom
EM	Expectation Maximization
GMM	Gaussian Mixture Model
GVF	Gradient Vector Flow
HU	Hounsfield Unit
kNN	k Nearest Neighbor
MAP	Maximum A-Posteriori Estimation
MI	Mutual Information
ML-SSM	Multi-level Statistical Shape Model
MO-SSM	Multi-organ Statistical Shape Model
MRF	Markov Random Field
MSD	Maximum Symmetric Surface Distance
ND	N Dimensional
NN	Neural Netwok
PA	Probabilistic Atlas
PCA	Principal Component Analysis
PDE	Partial Differential Equation
RMSD	Root Mean Square Symmetric Surface Distance
RVD	Relative Volume Difference
SSM	Statistical Shape Model
STP	Standard Pressure and Temperature
TPS	Thin Plate Spline
VOE	Volumetric Overlap Error

1. INTRODUCTION

Cancer is one of the leading causes of death worldwide and responsible for 7.6 million deaths (around 13% of all deaths) in 2008. Among the main cancer types, liver cancer is one of the most frequent cancer type and caused approximately 700000 deaths in 2008 [1]. Therefore, analysis and interpretation of 3D images from various image modalities play a crucial role in taking medical decisions such as diagnosis and treatment of liver cancer. Particularly, surgery planning of interventions (such as resection, transplantation etc.) and treatment planning requires liver volume measurement, the anatomical segments of liver, the vessel topography and the relation of tumors to these structures [2]. In addition to these, analysis can be used for monitoring purposes for patients with liver metastases where the disease is associated with an enlargement of liver [3]. Accurate liver segmentation from 3D image data is the basis of the analysis of liver.

Currently, common clinical practice for liver delineation relies on manual segmentation of computed tomography (CT) images, which is tedious, not reproducible, subjective and time-consuming (about one hour per data set) [4]. Therefore, fast and robust methods must be devised to automate liver segmentation process. However, segmentation of liver tissue remains a challenge because of several shortcomings of abdominal CT images [4]. First, intensities of organs and tissues adjacent to liver are similar to liver tissue especially for boundaries to stomach, heart and subcostal fat of the rib cage. Also, partial-volume effects create ambiguous edges with poor intensity discontinuities. Second, clinical CT images contains severe pathologies like large tumors, cirrhosis and previous resections, which have to be included in segmentation. In addition, veins and fat tissue within liver contributes to inhomogeneous intensity value appearances inside liver, which must be handled with appropriate methods. Third, high variation in liver shape makes it difficult to describe its complex structure for model-based segmentation approaches. Some examples of the difficulties outlined above are shown in Figure 1.1.

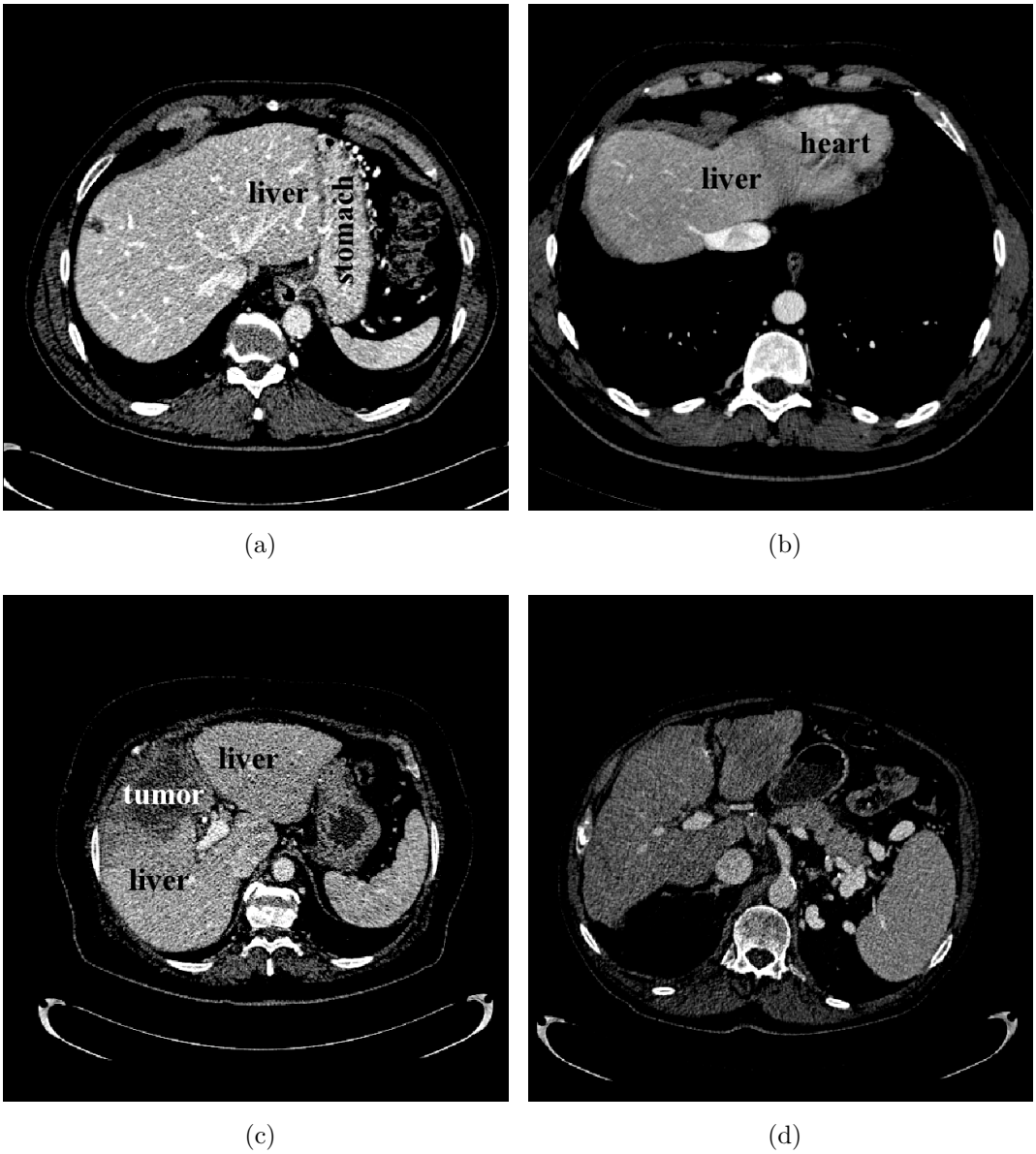

(a) (b)

(c) (d)

Figure 1.1. Examples of difficulties of liver segmentation: Ambiguous boundary between liver and (a) stomach, (b) heart; (c) tumor that must be included in segmentation; (c)-(d) highly varying liver shape.

1.1. Liver Anatomy

In order to propose an efficient liver segmentation algorithm, it is important to understand the location and anatomy of liver. Liver is located in the right upper quadrant of the abdominal cavity lying just below diaphragm. Its shape could be roughly described as a right angled triangular prism which have three surfaces namely superior, inferior and posterior [5].

The superior surface is the convex surface of liver which is fixed to the diaphragm and anterior abdominal wall by a triangular fold of peritoneum named falciform ligament. Also, the middle part of this surface is resting behind the xiphoid process. The diaphragm separates the liver from the lower part of the lungs and the heart. Liver is separated into two parts, namely the right and left lobes by the line of attachment of the falciform ligament as in Figure 1.2.

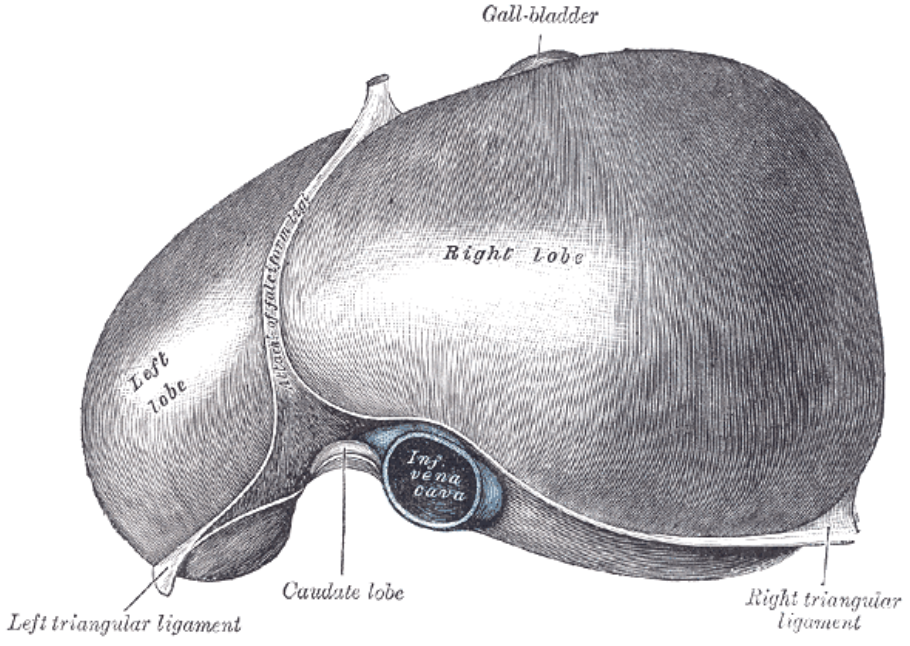

Figure 1.2. Superior surface of liver [5].

The inferior surface is the irregular and concave surface of the liver which is directed downward, backward and to the left. It is adjacent to the stomach, the

duodenum, the right colic flexure, the right kidney and the suprarenal gland. The inferior surface of the left lobe is consisted of gastric impression, moulded over surface of stomach and tuber omentale which is a rounded eminence lying onto the concavity of the lesser curvature of stomach. The inferior surface of the right lobe is divided into two parts by the fossa for the gallbladder. The first shallow part is the colic impression, which is produced by the right colic flexure. The second deeper part is the renal impression, which is shaped by the upper part of the right kidney and lower part of the right suprarenal gland. Medial to these two, there is the duodenal impression caused by a portion of the duodenum. Near that part, caudate process, which connects the right inferior parts of the liver to the caudate lobe is located. The inferior surface parts are shown in Figure 1.3.

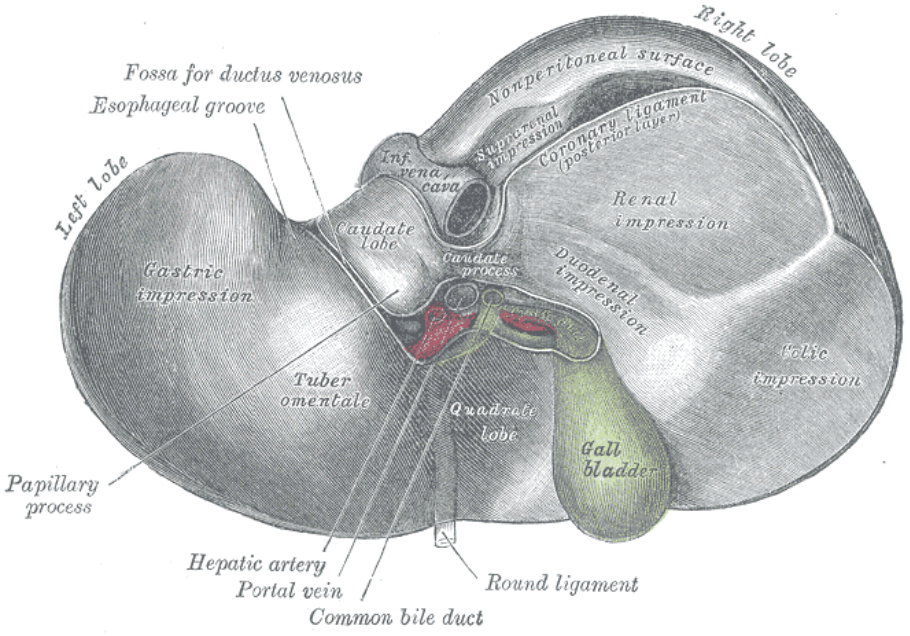

Figure 1.3. Inferior surface of liver [5].

The posterior surface is the rounded surface of liver bounded by the coronary ligament as shown in Figure 1.4. On this surface, the inferior vena cava is located in its fossa between the uncovered area and the caudate lobe. To the right of this fossa and above the renal impression, there is a small triangular area called suprarenal impression which is depressed by the right suprarenal gland. To the left of this fossa,

the caudate lobe is located and bounded by fossa for the ductus venosus on the left.

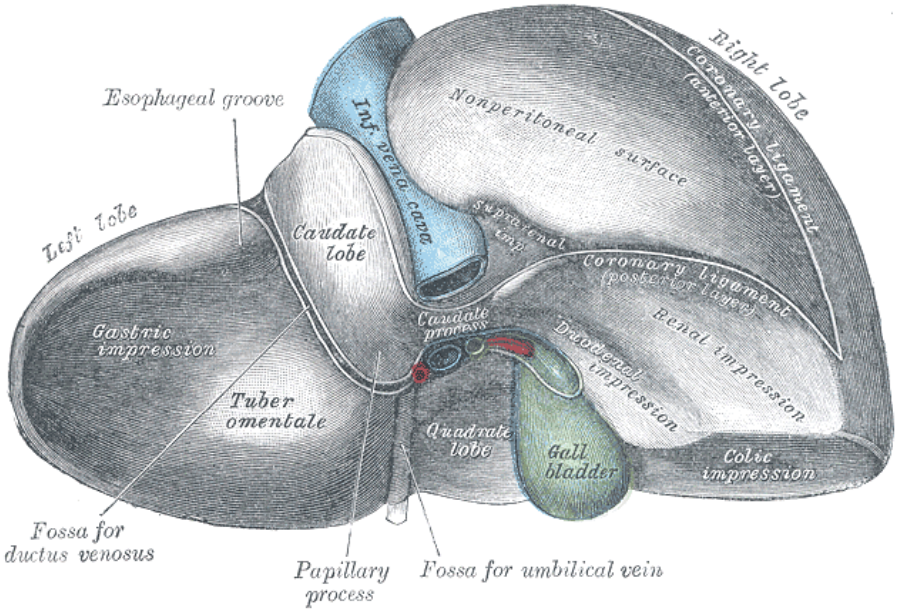

Figure 1.4. Posterior surface of liver [5].

1.2. Problem Definition and Proposed Solution

As we mentioned before, similar intensities between adjacent organs and tissues, dubious boundaries, the pathologies and the complex shape are the challenges of liver segmentation. Due to similar intensities between adjacent organs and tissues and weak boundaries, liver segmentations algorithms suffer from misrecognition of surrounding tissues (segmentation leakage into surrounding tissues) [6–9]. In addition to that, complex shape of the liver can not be modeled statistically even with a large number of training samples [4]. Moreover, inhomogeneous intensity value appearances inside liver makes intensity distribution estimation inside the liver difficult [4]. In order to cope with problems encountered, most of the hybrid liver segmentation methods utilize model driven prior information such as intensity distributions inside liver, shape or location of liver together with data driven information obtained from CT data. In this thesis, we adopted a similar approach and targeted an improved hybrid approach for liver segmentation.

In this thesis, we propose a hybrid liver segmentation algorithm for 3D CT data, which utilizes intensity distribution modeling, probabilistic atlas (PA) as model driven components and boundary terms in graph cuts as data driven components. Because of the fact that intensity values in CT images are known to correlate with different tissue types and there is an expected intensity value for liver [10], we will use intensity distribution modeling. To incorporate prior shape information into segmentation, we will use probabilistic atlases instead of statistical shape models (SSM) since these statistical models can not capture the complex shape of the liver [4] and have no clear anatomical landmark. As the data driven term, we will use boundary information based on gray level appearance model to efficiently deal with leakage problem during segmentation. Finally, graph cuts will be used as the optimization tool since they offer globally optimum solution for binary energy minimization formulations.

The main contribution of this work is twofold. First, we propose a novel way to build PA, based on the convex hulls of initial and reference liver masks and we also explain how to combine PA with graph cuts. In addition to that, we show how to incorporate gray level appearance model proposed in [11] into graph cuts and propose a new method for improving it.

The algorithm presented in this thesis have been evaluated two public real CT data sets (M1 and M2) of liver segmentation competition of "3D Segmentation in the clinic: a Grand Challenge" [12] workshop which is held at the Medical Image Computing and Computer-Assisted Intervention (MICCAI) 2007. In M1 data set, segmentation results that are obtained via leave-one-out cross validation are compared to manual delineations via various metrics based on volumetric overlap and surface distances and our results scored an average of 76.43 points out of 100. Since a score of 75 roughly coincides with human performance [4], our segmentation algorithm is claimed to be clinically acceptable semi-automatic method for liver segmentation. On the other hand, we obtained segmentation results on M2 data set. Since no manual delineations are provided for that data set, we are only able to visually compare our results with other state-of-the-art segmentation methods.

Chapter 2 reviews some generic methods, which are utilized in the proposed segmentation algorithm. In Chapter 3, we describe the proposed method in detail by discussing each component of the segmentation algorithm. Chapter 4 provides segmentation results on real patient data sets with comparisons to the other state-of-the-art methods. Discussions on the segmentation results are given in Chapter 5. We conclude in Chapter 6 with a discussion of the future work.

1.3. Literature Review on Liver Segmentation

Over the past decade, several automatic, semi-automatic and interactive liver segmentation methods are reported in literature. In general, liver segmentation commences with a pre-processing step followed by the main segmentation step. This segmentation step can be divided into three categories namely model driven, data driven and hybrid approaches based on the data terms and the prior information they utilize. After segmentation step, a post-processing step is generally included to correct or to prune the segmentation result.

At the beginning of the liver segmentation systems, several pre-processing steps are utilized to ease segmentation process. These pre-processing steps include resizing CT data [3,13], rotation correction [3,13], applying non-linear filters [14–17], applying diffusion filters [18, 19]. As a final step, liver segmentation systems generally benefit from a single or a sequence of post-processing steps. Boundary regularization via B-splines [14], optimal surface detection [20], laplacian mesh operator [21] and morphological operations [2, 3, 8, 14, 15, 19, 22] to prune or to fill gaps are the examples of such post-processing steps.

In terms of main segmentation step, liver segmentation systems could be broadly divided into three classes namely model driven, data driven and hybrid methods. Model driven approaches commonly try to model prior information like spatial location and shape of liver. Data driven methods utilize the information that is directly available from CT data. However, these two approaches are generally inadequate

to cope with the above-mentioned challenges. Therefore, hybrid methods that offer a combination of both the model driven components and the data driven components are proposed in the literature. Commonly, the hybrid approaches are the most promising methods.

Model driven components that are used in liver segmentation can be divided into two classes namely geometric models and pixel distribution models. Explicit and implicit statistical shape models (SSM) and probabilistic atlases (PA) are examples of geometric models whereas Bayesian voxel classification, graphs cuts and Markov random fields are examples of pixel distribution models.

Short after introduction by Cootes *et al.* [23], SSMs have become a popular tool in medical image analysis. Their robust performance comes from global shape constraints they provide for segmentation process as a prior information. However, SSMs strictly constraint segmentation in the space of allowed shapes learned from training data. Especially for structures with high variation like liver or regions with high curvature, they often lack the flexibility to accurately adapt to the structure of interest. Because of this reason, they mostly followed by a free form deformation step by utilizing deformable models [20,21,24–27]. Another way of accomplishing flexibility is to construct local shape models [28, 29]. SSMs used in liver segmentation differ in initialization, shape correspondence or representation, appearance models and search algorithms.

Following the idea of SSMs, Montagnat *et al.* [30] proposed a deformable model based on 2-simplex meshes. In that model, vertices of mesh experiences both global force from shape constraint and transformation (rigid, affine, cubic b-spline) and local forces from curvature and gradient information. As initialization, a template liver shape is selected and its location is found by using iterative closest point algorithm between template and coarsely segmented liver. In [18], Lamecker *et al.* proposed to build a 3D SSM of liver and connect it to an appearance model based on intensity profiles along liver boundary. In the boundary search step, a voxel is labeled as 'in-

side', 'outside' or 'no decision'. Then a weighted least squares estimation is performed to obtain new shape parameters. In that scheme, the voxels labeled as 'no decision' receives zero weight in order to achieve robustness. Saddi *et al.* [31] used deformable models via non-rigid template matching. In that work, a binary template is aligned to an image by maximizing the intensity distribution of inside and outside. Initialization is obtained by aligning the center of gravities of image and template. Heimann *et al.* [26] proposed a method based on evolutionary algorithm, SSM and a deformable mesh. Initialization of SSMs is done in a multi-resolution fashion via an evolutionary algorithm. In that scheme, a population of shapes is obtained by randomly selecting parameters of SSM and transformation and subsequently all members of this population is evaluated using local appearance model. As local appearance model, they used k-nearest neighbor (kNN) classifier based profile probabilities proposed in [32]. After obtaining an initialization, a deformable mesh is fitted based on internal forces which keeps mesh close to underlying SSM and external forces which drives the mesh towards the best fit data. Best fit data points are selected via graph-based optimal surface detection algorithm [33]. In [27], Kainmueller *et al.* matches a SSM to the image based on heuristic intensity model and refines solution by a deformable mesh. Mesh evolution is guided by three vector fields. The first one utilizes heuristic appearance model, the second one draws each vertex towards the center of its direct neighbors, and the last one ensures the mesh does not leave a narrow band defined around the SSM segmentation result. Seghers *et al.* [34] tries to solve the flexibility problem of SSM by employing local information. Unlike the global shape models, the authors build a statistical model for each edge of the mesh, capturing mean and covariance of the edge vector. In segmentation step a number of candidate points are selected using spherically sampled intensity profiles as appearance model and they are refined by dynamic programming such that candidate minimizes shape and appearance energies. Ling *et al.* [35] proposed a hierarchical SSM that divides mesh into patches to construct a local shape model. In every hierarchy level, both image and landmark points of SSMs are downsampled and SSM is constructed using downsampled mesh. Initialization is obtained through learning based boundary search in which pose parameters and some of SSM parameters are found using marginal space learning [36].

Then, five patches along boundary of liver is defined and using both probability of a point being boundary which is a part of k-th patch and weights of landmarks being in k-th patch boundary localization is done in a coarse-to-fine fashion. In [20], an algorithm based on SSM employing optimal surface detection strategy is presented. After obtaining a rough initialization through generalized Hough transform, candidate points are searched by a strategy based on the intensity at current landmark and gradient information. As the relaxation step, an optimal surface detection algorithm based on graph theory is utilized [33]. In [21], a SSM method which combines learned local constraints with constraints directly obtained from current curvature is presented in order to cope with the drawback of SSM in regions with high curvature.

Geometric deformable models (or active contours) presented by Caselles *et al.* [37] has gained importance in analysis of medical images. In those variational energy minimization methods, the evolution of an initial contour toward the true object boundary is considered as a front propagation problem which can be solved effectively by the use of level set and fast marching methods introduced by Osher and Sethian [38]. In level set formulation, the boundary of a 3D object is embedded as the zero-level set of a time-dependent function and this function is evolved with various speed functions. Speed function is the function that specifies the speed at which the contour evolves along its normal direction. It is also important to point out that these methods are prone to initialization and easily get stuck in some local minima during energy minimization which could lead to incomplete segmentations. Furthermore, prior information could be embedded into level set evolution via implicit versions of SSMs which are calculated in the space of signed distance functions [39]. Tons of effort is devoted to understand implicit shape space and variations of shape priors are used in algorithms based on active contours [39–44].

Saddi *et al.* [45] utilizes an implicit SSM and an appearance model that consists of inside and outside pixel distributions. The segmentation is parameterized with principal component analysis (PCA) coefficients, translation and rotation. The energy to be minimized is defined as the sum of the cost of inside/outside pixel dis-

tributions and the probability of the corresponding PCA coefficients (feasibility of the PCA model). The model feasibility (distribution of PCA coefficients) is modeled by kernel method, which in turn corresponds to manifold learning. Wimmer *et al.* [46] needs several user defined contours and interpolates these contours via radial basis functions in order to obtain a shape model . This shape model actually ensures that level set does not evolve too much from initial contour. In [11], a 2D liver segmentation algorithm, which utilizes an implicit version of appearance models in SSMs is proposed. For all grid points in narrowband around zero level set, boundary profiles are calculated and probabilities are assigned according to learned appearance model. All boundary point candidates are projected back to the zero level set and the boundary point with the highest probability is kept along each path. The obtained probability map is used in GVF and a global shape model estimation. In [47], Wimmer *et al.* proposed an active shape model which is built using non-parametric density estimates. As the boundary model, implicit version of kNN based intensity profile probabilities as in [32] are utilized. Furthermore, shape information is added to level set evoluation via determining shape probability using Parzen density estimation. Unlike previous methods which utilize a statistical model, Song *et al.* [48] creates patient specific b-spline surface models from a pre-segmentation image. Three B-spline based surface models are fitted to heart-liver boundary, liver right lobe boundary and lower liver surface on the pre-segmentation image. The surface models are further deformed to real pre-segmentation boundaries by using graph-based optimal surface detection algorithm [20]. The tissues outside the deformed model are removed from pre-segmentation image and the remaining part used as initialization to level set evolution. In a different work, Florin *et al.* [49] proposed a shape model that captures liver shape variations using a small number of carefully chosen slices. The idea is to select a minimal set of 2D contours along with an interpolation function to reconstruct the whole 3D surface in reference space. In order to achieve the goal, an energy minimization scheme is offered, which takes quality of reconstruction, image support and sensibility of variations in the projections' subspace. After model construction, segmentation of 3D image boils down to segmentation only in key slices. To perform segmentation at key slices, another energy functional based on regional

intensity distribution inside and outside the liver is minimized with respect to set of key slices and transformation.

Another possibility to include both prior shape and spatial location information into segmentation is utilization of probabilistic atlases (PAs). Also, relation of adjacent structures with each other is modeled effectively by multi-class atlases. General procedure for computing PA starts with registering all images in the training set onto a pre-selected image. Afterwards, manual delineations are warped onto the label image of template and averaged to provide a PA. Computation of PA and the way of incorporating it into segmentation are often the distinctions between atlas based segmentation methods. These methods suffer from misrecognition of surrounding tissues which is the primary source of error for PA based methods [6–9].

The first effort to build a PA of abdominal organs is reported by Park *et al.* [6]. In that study, A PA of an abdomen consisting of 4 organs (liver, kidneys, spinal cord) is constructed. Using 32 non-contrast CT, 31 were mapped onto one using thin plane splines (TPS) as warping transform and mutual information (MI) as the similarity measure. Segmentation is done by adding the PA into a Bayesian framework with a Markov random field (MRF) regularization term and solving maximum a posteriori estimation (MAP). In [7], a probabilistic model consisting of two kinds of probability(location and density) is builded. In order to achieve the correctness and accuracy of the atlas, a standard anatomical structure surrounding the liver is defined using spatial relations between liver, bone structure and diaphragm. To obtain this standard, the cross-sectional area of bone frame adjusted to a standard and diaphragm is warped to a plane using TPS. This anatomical structure is used as a reference and all 132 cases are deformed to it. Density probability of liver intensity is assumed Gaussian and calculated using regions under PA. Afterwards, liver is segmented by employing both probabilities. Slagmolen *et al.* [8] proposed to construct PA and corresponding intensity atlas via affine registration based on maximization of mutual information (MI) followed by a nonrigid registration using B-splines which uses MI and surface distance between the segmentations of reference and floating image as

a similarity metric. In that work, PA is not directly build on the image to be segmented. Therefore, an additional step is required to register both intensity atlas and PA onto image of interest and then, PA is thresholded to attain final result. Rixkoort *et al.* [3] proposed a method that combines non-rigid multi-atlas segmentation with voxel classification. In PA building step, 12 clean data (no rotations, high resolution etc.) registered to test case using B-spline model with negative mutual information using Parzen window estimation. A kNN classifier is employed in the second stage. Afterwards, a feature vector which includes gradient and Gaussian derivatives through second order and 3 spatial information features that indicates for each voxel which percentage of an atlas segmentation mass (the sum of all probabilities) is above, next or behind it is computed and several features are discarded via sequential floating forward feature selection. The feature vector is used in a kNN classifier and the result is refined by several post-processing steps. Okada *et al.* [28] proposed a method that utilizes PA and SSM. Registrations for constructing PA are done using manually segmented abdominal cavities using point-based nonrigid registrations. PA is used in voxel based segmentation as described by Zhou *et al.* [7]. In order to gain flexibility in SSM, they proposed multi-level SSM in which landmark points are divided into N sub-shapes at every level and SSMs are computed for those sub-shapes. After getting initialization from PA based segmentation, algorithm searches for boundaries using intensity profiles and fits and SSM to each patch from coarse to fine levels. Boundary search is formulated as an energy minimization which is based on weighted surface distances between initial contour and contour obtained via SSM. Also in finer levels, another term called adhesiveness is included into energy minimization in order to eliminate the inconsistency for the overlap landmarks between patches. Since subsequent multi-level SSM (ML-SSM) fitting could deal with outlier boundaries in a local fashion, SSM parameter estimation is not affected globally and this increased the accuracy of segmentations. In [29], Okada *et al.* further improved the performance of segmentation by introduction of multi-organ SSMs (MO-SSMs) in a similar manner to multi-level-SSM. Spatial normalization for PA and construction of SSMs are handled by defining a hierarchy of organ structures (abdominal cavity, liver and gallbladder/vena cava respectively). During segmentation, first parameters of ML-

SSMs are found for each patch for each organ, then they are refined by MO-SSMs by combining adhesiveness constraints of liver and other structures in the corresponding patches. The algorithm yielded better segmentation in the regions near vena cava and gallbladder since MO-SSM is limited to local region rather than whole space and by this way local variations of theses regions are modeled efficiently. Linguraru *et al.* [9] constructed PA by normalizing organ coordinates relative to the positions of the xiphoid. Then, modified affine transforms between random reference image from database and the rest of images which do not permit scaling found by employing normalized mutual information. This restriction is done to retain a higher level of organ variability in the atlas. In segmentation process, affine transform followed by non-linear registration based on B-splines deforms atlas to the reference image and then atlas is thresholded to obtain final segmentation result. In [50], Li *et al.* propose to build probabilistic liver atlas along with rib cage atlas which has relatively rigid characteristics. By this procedure, a more accurate mapping of probabilistic atlas onto the input CT volume is explored and problems of mapping stemmed from the variability in the liver shape are avoided. In segmentation phase, probabilistic atlas mapped onto image by utilizing rib-cage atlas with affine transformation and procedure described by Zhou *et al.* [7] followed. As a post-processing step, a deformable registration based on level-set motion is performed to gain the missing parts of liver due to mapping of probabilistic atlas.

Graph cuts, presented in [51], are tools for solving some low-level computer vision problems. Since they guarantee global minimum for certain types of energy functions, they swiftly gained popularity in medical image segmentation. They also offer ways to interactively edit the segmentation result, which is a desirable feature for clinical applications. Generally in these methods, a segmentation energy consisting of both regional and boundary terms is embedded into a graph through edge weights and the minimum cut solution is found. Therefore, defining an appropriate energy function is crucial in graph cuts based algorithms.

Beichel *et al.* [52] proposed a graph cut segmentation process with two refinement

steps, which is consisted of high user interaction. Regional term is obtained by user selected seed points. Massoptier *et al.* [17] proposed a graph cut segmentation method which is initialized by adaptive thresholding. Using mean and standard deviation of liver, image is thresholded and biggest connected component is chosen as liver. The far values according to mean and standard deviation are considered as background. The regional term is modeled as Gaussian distribution of liver. In a more recent work, Shimizu *et al.* [53] combines statistical atlas based approach and graph cuts algorithm. In order to accomplish this goal, two novel submodular energies are proposed. One of those is defined by using signed distance from boundary of an estimated shape and encourages that surface normals of segmentation to be parallel to those of estimated shape. Prior shape is estimated by following the procedure based on PA decribed in [6] and than an implicit SSM is fitted as in [39].

Another possibility to model prior information is to model pixel intensity distributions. In [13], Furukawa *et al.* proposed a method that first classifies tissues based on gaussian mixture model (GMM). In [54], a method that iteratively applies multi-resolution multi-class Bayesian classification is proposed. Intensity models for liver, tumor and the other regions are created in the first step. The posteriori probabilities for each voxel is calculated by previously obtained multi-class distribution and using uniform distribution for prior model. Finally MAP rule is applied separately for two main class and results are combined. As final step adaptive morphological operations and GAC is used as a fine-tuning. The three step (Bayesian classification), morphological operations and GAC is used iteratively.

Data driven components include regional terms and edge maps used with level sets, n-links in graph cuts, intensity criteria used with region growing methods and other intensity criteria in rule based systems.

In liver segmentation, design of an appropriate speed function that utilizes image data has utmost importance. Pan *et al.* [55] defined a speed function specific for liver segmentation. The idea is to slow down the evolution of the front as it passes from

edges (incorporate memory into static edge function) and is to use a priori information from other organs (e.g. distance between skin and liver). It is shown that, by using this speed term the contour is able to stop at weak boundaries and at spurious edges between ribs, liver and muscle. Garamendi *et al.* [15] modifies inside and outside regional models of Chan-Vese algorithm [56] in order to use local information around the voxel. Chi *et al.* [57] used a 2.5D gradient vector flow (GVF) [58] snake, which combines the vector field from distance transform with the GVF. Starting from the top slice distance transform vector field attracts snake to the vicinity of boundary, then GVF refines the result. In order to prevent leakage, linear edge enhancement is performed near rib cage. Also voxels of adjacent organs are labeled using 2D k-means clustering with predefined area and non-liver labels are used to block level set evolution. In [13], Furukawa *et al.* refines the results of a classification step via active contours. Active contour evolution is driven by an additional distance term from skin. Lee *et al.* [19] proposed a method based on a region-growing algorithm followed by active contour refinement. Region-growing algorithm grows the seed regions until reaching high gradient values in the boundaries. Also several post-processing steps are included in order to add missed regions to the final result. Massoptier *et al.* [16] proposed an active contour method based on basic image processing techniques (thresholding, morphological operations) and active contours. In [47], region model is build by a cascade of boosted classifiers and the result of classifiers incorporated as a dilatation or erosion of the surface into the level set equation. Kohlberger *et al.* [59] tracked a point on the initial curve by the normal speed at that point. By this tracking mechanism, authors are able to model local intensity distributions and local curvature constraints for every point in the initial level set for all training images. Energy to be minimized is defined locally by intensity distributions and curvature on the tracked points and a global model for shape prior is included.

Edge weights for neighboring pixels utilized in graph cuts constitute another class of data driven components used in liver segmentation. Beichel *et al.* [52] used a boundary term for graphcut obtained from planeless map defined by structure tensor. Massoptier *et al.* [17] used directed edges which favors for brighter tissues are weighted

according to intensity differences as the boundary term. In [53], an energy is proposed to correct undesirable change of regional term due to pathologies and defined as a penalty term equal to distance to ribs.

Region growing methods could provide competitive results [2, 22] compared to more sophisticated counterparts. These methods start from a small region called seed region and new voxels are added to the seed based on some pre-defined data driven criteria. Region growing methods often fails in weak edges and needs to be supported by several pre- or post-processing steps.

Ruskó *et al.* [2] employed an advanced region-growing technique in which a new voxel is added to segmentation if all voxels in 5mm is in the estimated intensity range. In order to prevent leakage to the heart, lung-liver separation is detected and voxels above this separation are given a high intensity value. Moreover, method needs several postprocessing near vena cava and lung. In [60], Ruskó *et al.* improved the previous method by introduction of information from multi-phase CT images. Susomboon *et al.* [61] uses clustering, voxel classification and region growing to segment liver. The expectation maximization (EM) algorithm is used to define intervals for different tissues. For all non-tissue regions Haralick texture features are calculated and fed into a classification and regression tree. The region with highest probability of liver tissue is used as seed region for 2D region growing process. Beck *et al.* [22] proposed a 3D region growing technique based on a nonlinear coupling criterion, which is the weighted intensity difference of a neighborhood to the seed intensity. Weights are assigned by a non-normalized gaussian function of spatial distance and a non-normalized gaussian function of intensity difference. This method needs high level of user interaction (cutting leakages with a virtual knife) to refine segmentation obtained by region growing.

Rule based liver segmentation methods employ intensity based criteria as data driven components. Gao *et al.* [62] proposed 2.5D liver segmentation algorithm based on a set of rules. Histogram analysis and thresholding are used as the heart of the

algorithm. In the regions where thresholding fails boundary, intensity and shape based rules are incorporated to include or exclude these regions. In [63], Schmidt *et al.* proposed a scripting language that defines a set of rules (such as intensity distributions, neighborhood relations, geometric features) in order to successively segment different parts of CT data. Thanks to this language, authors are able to segment background air, lungs and other intrabody air, subcutaneous fat and muscle layer, bones within muscle layer, aorta, spine, heart, and liver. In segmentation, already detected structures are used to assist next step.

Apart from predominant ones, there are some other successful methods for segmenting liver tissue that use data driven components. In [14], Tsai *et al.* proposed a neural network (NN) based method in which regional histograms are used as features. However NN is not adequate to determine liver, thus, an exhaustive postprocessing step is included. Removal of unwanted and isolated parts are handled via a priori information (experimental or manual) about the location and area of liver. Than liver boundary is found and narrowed. In order to smooth boundary, morphological operations (closing) followed by b-spline smoothing is utilized. Schenk *et al.* [64] proposed an semiautomatic segmentation method based on livewire [65]. A few slices (including top and bottom) are segmented via livewire in real time by operator. Then the remaining slices are interpolated from segmented slices using distance transforms of those slices. Furthermore, if segmentation results is not satisfactory, user defined seed points are projected into slice by interpolation and user is given opportunity to remove delete or add new seed points in this slice and to segment using livewire.

2. BACKGROUND ON EMPLOYED GENERIC METHODS

The algorithm proposed in this thesis utilizes several popular tools in computer vision. This section is devoted to explain the idea and the mathematical theory behind these generic methods.

2.1. The Gaussian Mixture Models and the Expectation Maximization Algorithm

In statistics, *density estimation* is defined as modeling a probability distribution of a random variable given a finite set of observations. Because of the fact that there are infinitely many probability distributions that could be responsible for the observed data, the selection of appropriate distribution to model the data set is critical [66]. The observed data could be modeled with a single parametric probability distribution, complex distributions that are formed by basic probability distributions and nonparametric methods.

One possibility to estimate density is to assume a Gaussian distribution, which is governed by mean and variance. However, a single Gaussian distribution is generally not adequate to model complex observations encountered in real life. In order to obtain a correct model for the underlying data, probabilistic models based on linear superpositions of basic distributions such as Gaussians are suggested in literature. These complex distribution models are known as *mixture models* [66] and called *Gaussian mixture models* when the superpositioned probability distributions are consisted of Gaussian distributions. Almost any continuous density can be approximated by adjusting the number of Gaussians, their mean and covariances [66]. A simple example of a Gaussian mixture distribution in one dimension is given in Figure 2.1.

Following the notation in [66], for a D-dimensional vector $\boldsymbol{x}$, the multivariate

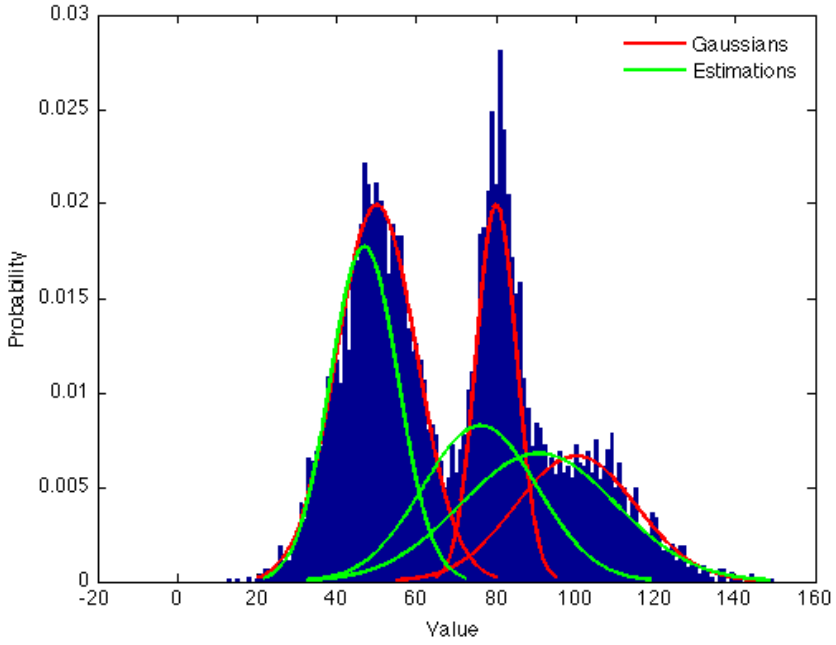

(a)

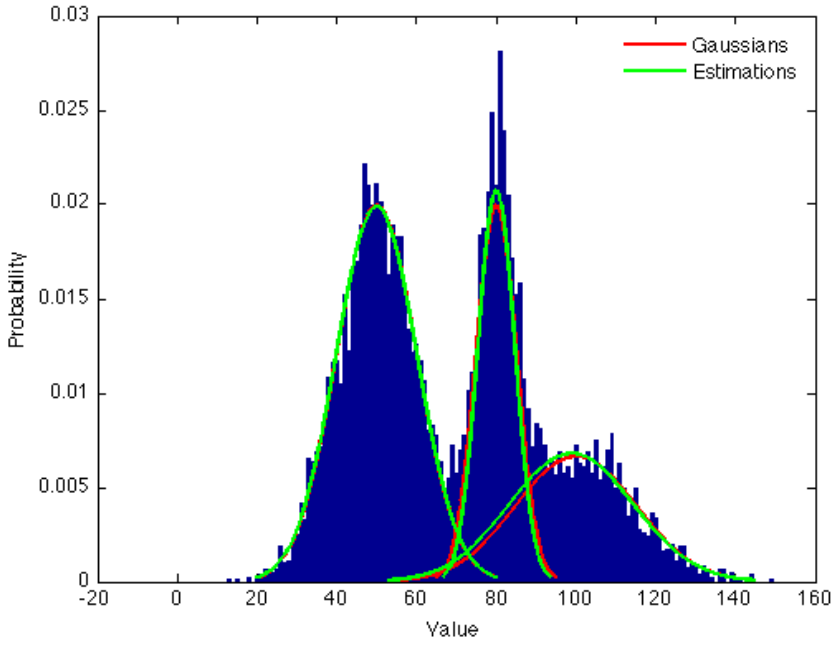

(b)

Figure 2.1. Histogram of the samples drawn from a three component GMM. The true Gaussian components are shown in red while the estimations are shown in green after (a) 40, (b) 80 EM iterations.

Gaussian distribution is of the form

$$\mathcal{N}(\boldsymbol{x}|\boldsymbol{\mu},\boldsymbol{\Sigma}) = \frac{1}{(2\pi)^{D/2}}\frac{1}{|\boldsymbol{\Sigma}|^{1/2}}\exp\left\{-\frac{1}{2}(\boldsymbol{x}-\boldsymbol{\mu})^T\boldsymbol{\Sigma}^{-1}(\boldsymbol{x}-\boldsymbol{\mu})\right\} \tag{2.1}$$

where $\boldsymbol{\mu}$ is a D-dimensional mean vector, $\boldsymbol{\Sigma}$ is a $D \times D$ covariance matrix and $|\boldsymbol{\Sigma}|$ is the determinant of $\boldsymbol{\Sigma}$. A superposition of K Gaussian densities are given as

$$P(\boldsymbol{x}) = \sum_{k=1}^{K}\pi_k\mathcal{N}(\boldsymbol{x}|\boldsymbol{\mu}_k,\boldsymbol{\Sigma}_k) \tag{2.2}$$

where π_k parameter denotes mixing coefficients of Gaussians. Since the integration of $P(\boldsymbol{x})$ must be equal to one, it is easy to show that

$$\sum_{k=1}^{K}\pi_k = 1. \tag{2.3}$$

Furthermore, requirements $P(\boldsymbol{x}) \geq 0$ and $\mathcal{N}(\boldsymbol{x}|\boldsymbol{\mu}_k,\boldsymbol{\Sigma}_k) \geq 0$ imply $\pi_k \geq 0$ for all k. Together with Equation 2.3, we obtain an interval for mixing coefficients such that

$$0 \leq \pi_k \leq 1. \tag{2.4}$$

To ease the discussion, let us introduce an K-dimensional binary latent variable $\boldsymbol{z}$ in which a particular element z_k is equal to 1 and all other elements are equal to zero. Note that the values of z_k satisfy $z_k \in \{0,1\}$ and $\sum_k z_k = 1$. Let the marginal distribution over $\boldsymbol{z}$, $P(\boldsymbol{z})$, is defined in terms of mixing coefficients such that

$$P(z_k = 1) = \pi_k \tag{2.5}$$

which could be written as

$$P(\boldsymbol{z}) = \prod_{k=1}^{K}\pi_k^{z_k}. \tag{2.6}$$

In a similar manner, the conditional distribution of $\boldsymbol{x}$ given a particular value for $\boldsymbol{z}$ is given as a Gaussian distribution

$$P(\boldsymbol{x}|z_k = 1) = \mathcal{N}(\boldsymbol{x}|\boldsymbol{\mu}_k, \boldsymbol{\Sigma}_k) \tag{2.7}$$

which could also be written as

$$P(\boldsymbol{x}|\boldsymbol{z}) = \prod_{k=1}^{K} \mathcal{N}(\boldsymbol{x}|\boldsymbol{\mu}_k, \boldsymbol{\Sigma}_k)^{z_k}. \tag{2.8}$$

The marginal distribution of $\boldsymbol{x}$ could be obtained by summing the joint distribution $P(\boldsymbol{x}, \boldsymbol{z}) = P(\boldsymbol{z})P(\boldsymbol{x}|\boldsymbol{z})$ over all possible values of $\boldsymbol{z}$, such that

$$P(\boldsymbol{x}) = \sum_{\boldsymbol{z}} P(\boldsymbol{z})P(\boldsymbol{x}|\boldsymbol{z}) = \sum_{k=1}^{K} \pi_k \mathcal{N}(\boldsymbol{x}|\boldsymbol{\mu}_k, \boldsymbol{\Sigma}_k). \tag{2.9}$$

Therefore, we obtained an equivalent formulation of Equation 2.2 which involves an additional latent variable. From a different point of view, Equation 2.9 states that for every observed data point x_k there is a corresponding latent variable z_k.

Moreover, the conditional probability of $\boldsymbol{z}$ given $\boldsymbol{x}$, $P(\boldsymbol{z}|\boldsymbol{x})$, could be computed via Bayes' theorem and given as

$$\begin{aligned} \gamma(z_k) = P(z_k = 1|\boldsymbol{x}) &= \frac{P(z_k = 1)P(\boldsymbol{x}|z_k = 1)}{\sum_{j=1}^{K} P(z_j = 1)P(\boldsymbol{x}|z_j = 1)} \\ &= \frac{\pi_k \mathcal{N}(\boldsymbol{x}|\boldsymbol{\mu}_k, \boldsymbol{\Sigma}_k)}{\sum_j \pi_j \mathcal{N}(\boldsymbol{x}|\boldsymbol{\mu}_j, \boldsymbol{\Sigma}_j)}. \end{aligned} \tag{2.10}$$

This conditional probability, $\gamma(z_k)$, can be viewed as the responsibility of component k for observing $\boldsymbol{x}$.

In order to model observations, $\{x_1, \ldots, x_n\}$, in terms of mixtures of Gaussians, one must estimate parameters π_k, μ_k, Σ_k for all k such that the log of the likelihood

function is maximized [66]. Log of the likelihood function is defined as

$$\ln P(\boldsymbol{x}|\boldsymbol{\pi}, \boldsymbol{\mu}, \boldsymbol{\Sigma}) = \sum_{n=1}^{N} \ln \left\{ \sum_{k=1}^{K} \pi_k \mathcal{N}(x_n|\boldsymbol{\mu}_k, \boldsymbol{\Sigma}_k) \right\}. \tag{2.11}$$

Setting the derivatives of Equation 2.11 with respect to μ_k to zero, we get

$$-\sum_{n=1}^{N} \frac{\pi_k \mathcal{N}(x_n|\boldsymbol{\mu}_k, \boldsymbol{\Sigma}_k)}{\sum_j \pi_j \mathcal{N}(x_n|\boldsymbol{\mu}_j, \boldsymbol{\Sigma}_j)} \boldsymbol{\Sigma}_k (x_n - \boldsymbol{\mu}_k) = 0. \tag{2.12}$$

Rearranging terms we obtain

$$\boldsymbol{\mu}_k = \frac{1}{N_k} \sum_{n=1}^{N} \gamma(z_{nk}) x_n \tag{2.13}$$

where

$$N_k = \sum_{n=1}^{N} \gamma(z_{nk}). \tag{2.14}$$

It is important to note that mean $\boldsymbol{\mu}_k$ for the component k is calculated by taking a weighted mean of all the points in the data set. The weighting factor for a data point is given by the responsibility of the component k for generating that data point, x_n. N_k could be viewed as the effective number of points assigned to component k.

Similarly, if we set the derivatives of Equation 2.11 with respect to $\boldsymbol{\Sigma}_k$ to zero and rearrange terms to obtain $\boldsymbol{\Sigma}_k$, we get

$$\boldsymbol{\Sigma}_k = \frac{1}{N_k} \sum_{n=1}^{N} \gamma(z_{nk})(x_n - \boldsymbol{\mu}_k)(x_n - \boldsymbol{\mu}_k)^T. \tag{2.15}$$

Again, every point is weighted by the posterior probability to estimate the covariance.

Finally, log of the likelihood function given in Equation 2.11 must be maximized with respect to π_k with the constraint given in Equation 2.3. To accomplish this goal,

one needs to use a Lagrange multiplier and maximizes

$$\ln P(\boldsymbol{x}|\boldsymbol{\pi}, \boldsymbol{\mu}, \boldsymbol{\Sigma}) + \Lambda \left(\sum_{k=1}^{K} \pi_k - 1 \right). \tag{2.16}$$

The derivative of the quantity given in Equation 2.16 is given by

$$\sum_{n=1}^{N} \frac{\mathcal{N}(x_n|\boldsymbol{\mu}_k, \boldsymbol{\Sigma}_k)}{\sum_j \pi_j \mathcal{N}(x_n|\boldsymbol{\mu}_j, \boldsymbol{\Sigma}_j)} + \Lambda = 0. \tag{2.17}$$

Solving Equation 2.17 for Λ gives $\Lambda = -N$. Using this result, rearranging terms gives us

$$\pi_k = \frac{N_k}{N}. \tag{2.18}$$

Thus, the mixing coefficient of the component k is computed as the average responsibility which that component k takes for generating data points.

It is important to note that Equations 2.13, 2.15 and 2.18 does not provide a closed form solution for maximizing the log of the likelihood function due to the responsibilities $\gamma(z_{nk})$ depend on the parameters that are supposed to be estimated. However, expectation maximization (EM) proposed in [67] is capable of finding a solution. EM algorithm is summarized in Figure 2.2. It is also proven in [67] that every update to the parameters together with expectation and maximization steps is guaranteed to increase the value of the log likelihood function.

2.2. Structure Preserving Diffusion Filters

Diffusion is a well known physical phenomenon and defined as the spread of particles from regions of higher concentration to regions of lower concentration without creating or destroying mass [68]. The equilibration property of this physical observation is governed by the mathematical expression called *Fick's Law*, which is stated

1. Initialize the means $\boldsymbol{\mu}_k$, covariances $\boldsymbol{\Sigma}_k$ and mixing coefficients π_k and evaluate the initial value of the log likelihood $\ln P(\boldsymbol{x}|\boldsymbol{\pi}, \boldsymbol{\mu}, \boldsymbol{\Sigma})$.

2. Expectation step Compute the responsibilities using current responsibilities.

$$\gamma(z_{nk}) = \frac{\pi_k \mathcal{N}(x_n|\boldsymbol{\mu}_k, \boldsymbol{\Sigma}_k)}{\sum_j \pi_j \mathcal{N}(x_n|\boldsymbol{\mu}_j, \boldsymbol{\Sigma}_j)}.$$

3. Maximization step Estimate new parameters using current responsibilities.

$$\begin{aligned}
\boldsymbol{\mu}_k^{new} &= \frac{1}{N_k} \sum_{n=1}^{N} \gamma(z_{nk}) x_n \\
\boldsymbol{\Sigma}_k^{new} &= \frac{1}{N_k} \sum_{n=1}^{N} \gamma(z_{nk})(x_n - \boldsymbol{\mu}_k^{new})(x_n - \boldsymbol{\mu}_k^{new})^T \\
\pi_k &= \frac{N_k}{N} \\
\text{where} \qquad N_k &= \sum_{n=1}^{N} \gamma(z_{nk}).
\end{aligned}$$

4. Evaluate the log likelihood $\ln P(\boldsymbol{x}|\boldsymbol{\pi}, \boldsymbol{\mu}, \boldsymbol{\Sigma})$ with new parameters and check the convergence of the parameters or the log likelihood. If convergence criterion is not satisfied, **return to step 2**.

Figure 2.2. Expectation Maximization Algorithm.

as

$$\Phi = -D \cdot \nabla I. \tag{2.19}$$

Equation 2.19 states a concentration gradient ∇I causes a flux Φ, to neutralize this gradient, with a magnitude that is proportional to the ∇I. The relation between ∇I and Φ is expressed by the *diffusion tensor*, which is a positive definite symmetric matrix. The case where Φ and ∇I is parallel is named as *isotropic*. In such a case, the diffusion tensor could be given by a positive scalar valued *diffusivity* g. On the contrary, Φ and ∇I are often not parallel in *anisotropic* diffusion.

The concentration change with time that diffusion causes without creating or destroying mass is given by *Fick's second law* or *continuity equation* and defined as

$$\partial_t I = -\text{div } \Phi \tag{2.20}$$

where t denotes time.

If we write Fick's Law into the continuity equation, we obtain *diffusion equation*

$$\partial_t I = \text{div } (D \cdot \nabla I). \tag{2.21}$$

This equation is generally encountered in the transport processes such as heat, food, population dynamics etc. In computer vision, pixel intensity can be considered as a local concentration value. Thus, image function $I(x, y)$ can be processed analogous to concentration function. Also, it is important to clear the confusing terminology of diffusion filters in computer vision [68]. Diffusion is called *homogeneous* if diffusion tensor is constant in entire domain and *inhomogeneous* if diffusion tensor is space-dependent. Diffusion filters also differentiate from each other in terms of the feedback used during process. Often, the diffusion tensor is a function of the differential structure of the evolving image itself and this type of diffusion is called *nonlinear*. If the

diffusion tensor does not depend on the evolving image, then diffusion is called *linear*.

Suppose one could obtain current estimates of the locations of the region boundaries at the time scale t. Then it could be possible to obtain sharper boundaries by encouraging smoothing within region instead of smoothing across regions. In order to accomplish this goal, diffusion tensor have to be set to one in the interior of regions and zero on the boundary estimates [69].

2.2.1. Edge Enhancing Diffusion Filter

In some situations, it could be desirable to bias the flux towards the orientation of interesting features [68]. In such a case, scalar diffusivity remains incapable and a diffusion tensor that leads to anisotropic filters has to be introduced. In order to achieve this goal, one may not only consider the magnitude of the edge estimate but also its direction. For this reason, an orthonormal system of eigenvectors of the diffusion tensor D may be constructed such that eigenvectors reflect the estimated edge structure.

Edge enhancing diffusion filter [68] aims to smooth an image within a region and block diffusion across boundaries. To this end, *structure tensor* of the image is computed for every pixel in image as

$$J_\rho(\nabla I_\sigma) = \mathcal{N}(0,\rho) * (\nabla I_\sigma \cdot \nabla I_\sigma^T) \tag{2.22}$$

where ∇I_σ denotes the derivatives computed by derivatives of Gaussian with standard deviation σ and $\mathcal{N}(0,\rho)$ is a Gaussian with mean zero and standard deviation ρ. Structure tensor J_ρ depicts the predominant orientations in the vicinity of investigated point and also reveals the degree to which those orientations are coherent [70]. Besides, structure tensor is a symmetric positive semidefinite matrix, which is invariant to the sign changes in gradient [70]. It should be noted that since we are only interested in edge enhancing properties, we may set integration scale ρ to zero.

Suppose e_1, e_2 with $e_2 \geq e_2$ are the eigenvalues of the structure tensor J_ρ and v_1, v_2 are the corresponding orthonormal eigenvectors. Since we want diffusion to respect the structures in the image, the diffusion tensor must be selected in a way that it shares the same set of eigenvectors v_1, v_2 of J_ρ. The choice of corresponding eigenvalues d_1, d_2 should inhibit diffusion in the direction of dominant orientation and allow diffusion to take place if there is no prominent structure. Weickert [68] proposed the following set of eigenvalues:

$$\begin{aligned} d_1(e_1) &= g(e_1), \\ d_2 &= 1 \end{aligned} \tag{2.23}$$

with

$$g(s) = \begin{cases} 1 & (s \leq 0), \\ 1 - \exp\left(\frac{-\eta_m}{(s/\lambda)^m}\right) & (s > 0). \end{cases} \tag{2.24}$$

where η_m and λ are constants. The value of constant η_m is calculated so as to make flux $\Phi(s) = sg(s)$ increasing for $s \in [0, \lambda]$ and decreasing for $s \in [\lambda, \infty]$. It is reported that the choice $m = 4$ (which implies $\eta_4 = 3.31488$) gives visually good results [68].

In Figure 2.3a, an image consisted of a triangle and rectangle, which is degraded by noise is shown. Result obtained by linear diffusion, $t = 80$, is shown in Figure 2.3b. It is observed that linear diffusion filtering is capable of removing noise, however, it also blurs and dislocates the edges. The result when applying isotropic nonlinear diffusion equation

$$\partial_t I = \text{div}\ (g(\|\nabla I_\sigma\|^2) \cdot \nabla I) \tag{2.25}$$

with parameters $\lambda = 3.5$, $\sigma = 3$, $t = 80$ is given in Figure 2.3c. Isotropic nonlinear diffusion does not lead to correspondence problems. However, the noise in the edges are also preserved because of the reduced diffusivity along boundaries. Finally, the

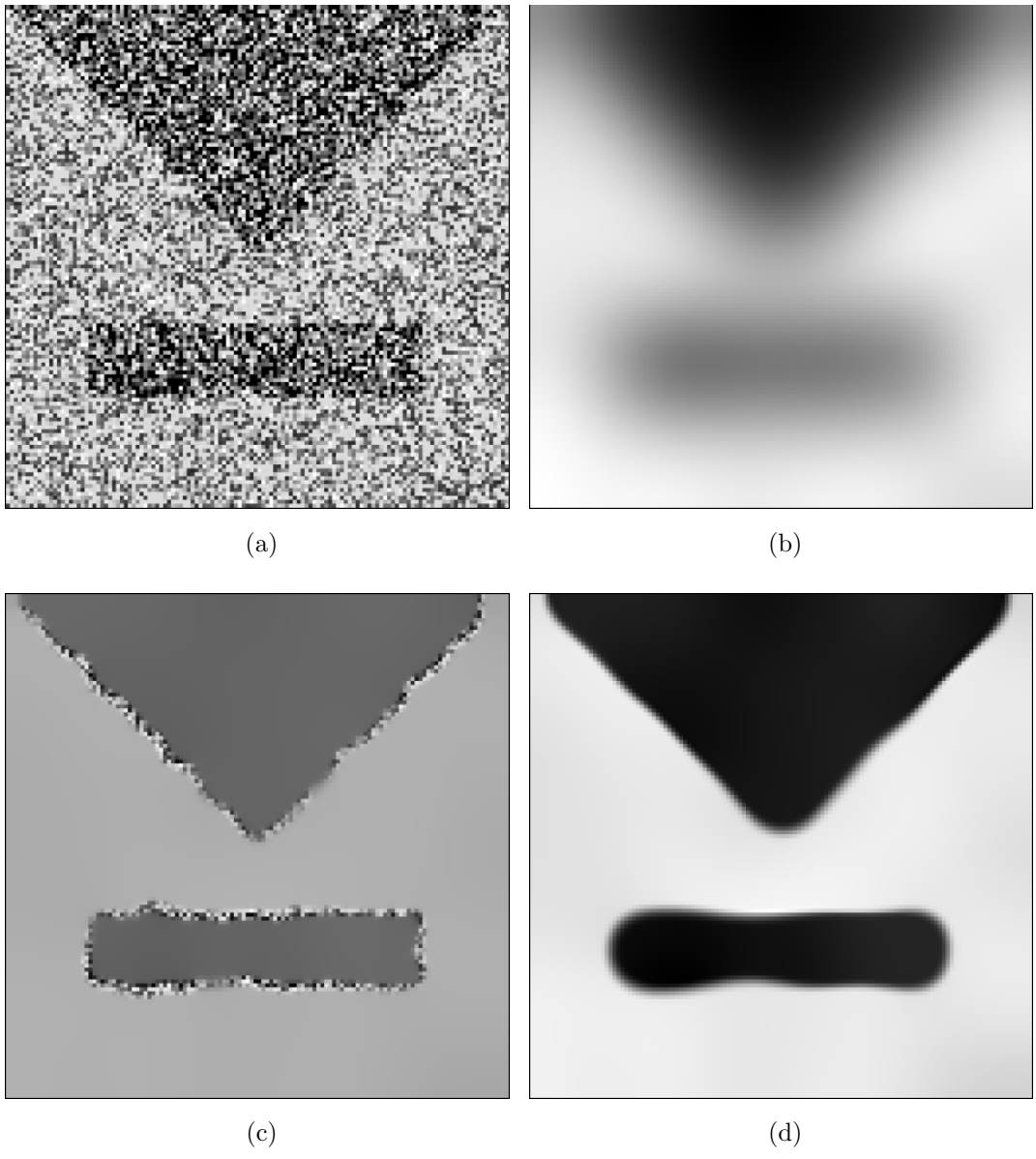

(a) (b)

(c) (d)

Figure 2.3. Restoration properties of diffusion filters [68]. (a) Test Image, (b) Linear Diffusion, (c) Nonlinear isotropic diffusion, (d) Edge Enhancing Diffusion.

result obtained via edge enhancing diffusion with $\lambda = 3.5$, $\sigma = 3$, $t = 80$ is given in Figure 2.3d. It reveals that edge enhancing diffusion possesses the advantages of both methods. However, because of the smoothing along the edges, corners get rounded than nonlinear isotropic case.

2.3. Graph Cuts

Computer vision research deviated from heuristic design to systematic investigation of mathematical models since 1960's [71]. As a result of that active research, many of the computer vision problems could be modeled in terms of energy minimization formulations. In the last decade, combinatorial graph cut algorithms were proven to be a useful multidimensional optimization tool for some kinds of energy functions and were applied to a variety of computer vision problems [72].

Energy based optimization methods could be classified in terms of the type of energy function and the optimization tool they use [73]. The majority of energy based methods could broadly be divided into two with respect to the domain of energy functions. To be more precise, they could be divided as an optimization of a functional defined on a continuous contour or surface and optimization of a cost function defined on a discrete set of variables [73]. The former group of techniques formulates segmentation in the domain of continuous functions $\mathbb{R}^{\infty}$ and generally optimized via finite differences or finite elements. The methods in this group includes snakes [74], region competition [75], geodesic active contours [37] and other methods based on level sets [38]. These methods employ several model specific and contextual information as regional and boundary terms, some of which are geometrically motivated [37]. However, most of the times, variational optimization techniques for these methods only guarantee to converge to a local minima of the energy function. On the contrary, the latter group of methods either directly formulate the problem as combinatorial optimization in finite dimensional space on $\mathbb{Z}^n$ or minimizes some discrete energy function whose minima approximates solution of some continuous problem. These types of methods propose to minimize an energy function defined over a finite set

of integer valued variables which are associated with graph nodes corresponding to image pixels or control points [73]. Apart from graph cut methods, all combinatorial algorithms use discrete variables whose values denote the direction of a segmentation boundary path along graph. Intelligent scissors [76], live-wire [65] are examples of path based methods. These path based methods are limited to 2D applications since object boundary in higher dimensions could not be described by a path [73].

Before the introduction of s/t graph cuts [77] for object segmentation, exact minimization by computing a global optima is possible for some 2D segmentation methods. Because of that reason, 3D segmentation problems that are often formulated via variational techniques or ad-hoc approximations are based on the results of globally optimum 2D methods. Global solutions are preferable because of their robustness. In addition to that, global solutions can reveal the suitability of cost functions to a specific task, since no numerical problems are introduced during optimization [73].

Graph cuts offer a globally optimal object segmentation method for N-dimensional (ND) images. They can optimize discrete energies which can enforce piecewise smoothness while preserving sharp discontinuities in the same manner as Mumford-Shah [78] functionals [73]. In [73], it is shown how to employ visual cues such as regional and boundary terms, shape information and topological constraints into the binary graph cut framework. Moreover, it is shown in [79] how graph cuts and geodesic active contours [37] are connected to each other. They show that the discrete cut metrics on a grid can approximate any continuous Riemannian metric that are used to approximate geometric functionals such as area, length and flux. In addition to that, the connection between graph cuts and level sets is established in [80]. They developed a novel integral approach for solution to the surface propagation partial differential equations (PDEs) based on graph cuts.

2.3.1. Basic Definitions and Formulation

A graph which is defined as $\mathcal{G} = \langle \mathcal{V}, \mathcal{E} \rangle$ consists of a set of nodes or vertices $\mathcal{V}$ and a set of edges $\mathcal{E}$ connecting neighboring nodes. Undirected graphs are graphs where each pair of connected nodes is described by a single edge $e = \{p, q\} \in \mathcal{E}$. A simple 2D example of an undirected graph is given in Figure 2.4.

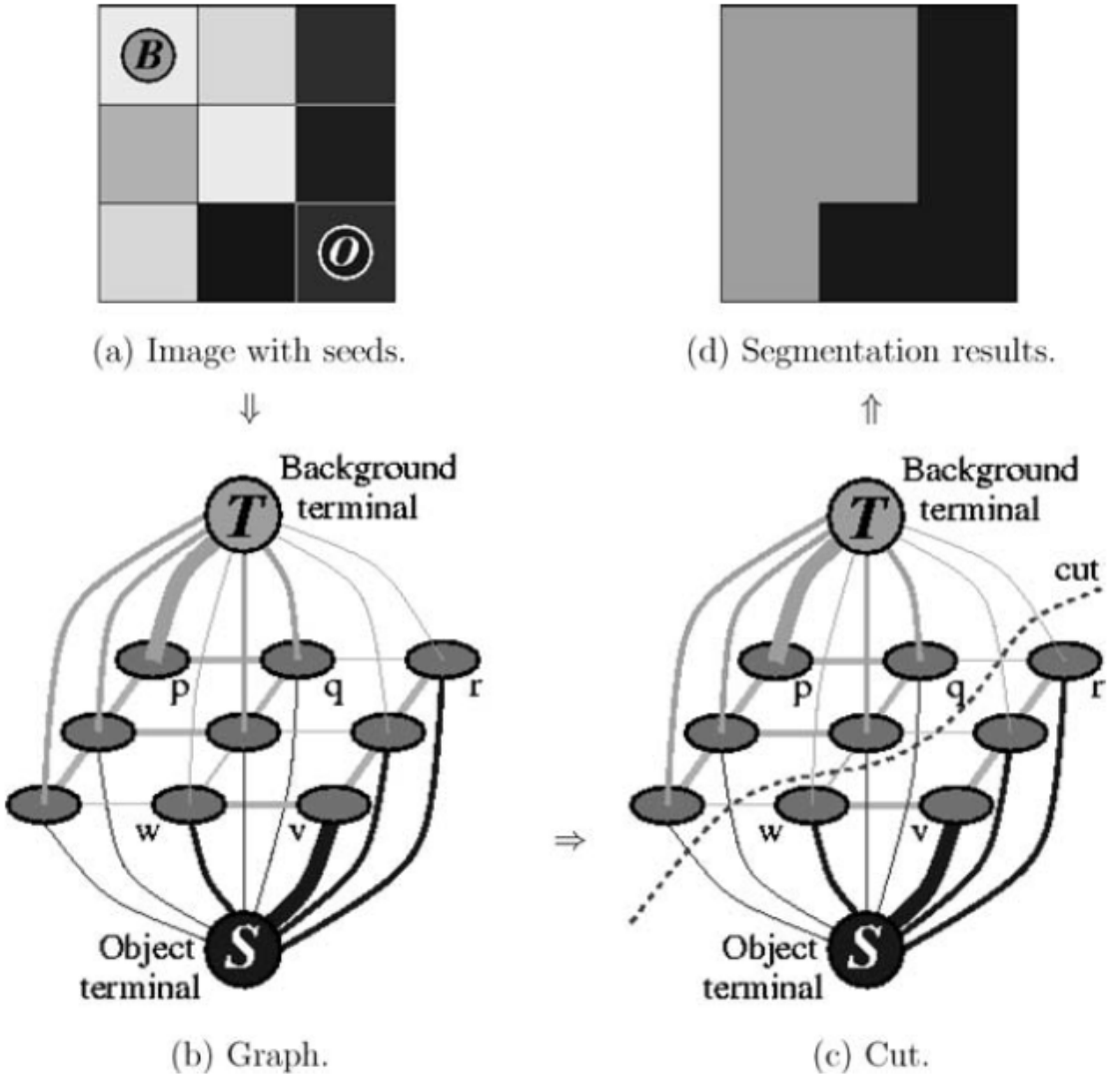

Figure 2.4. A simple s/t graph and an example segmentation for a 3×3 image [73].

The nodes set $\mathcal{V} = \{S, T\} \cup \mathcal{P}$ is comprised of two special terminal nodes, which

are called the *source*, S, and the sink, T, and a set of non-terminal nodes $\mathcal{P}$, which represent pixels (or voxels) of image. Source and sink nodes represent *object* and *background* respectively. Moreover, neighboring pixels are connected to each other via edges to form a ND grid. These edges are named *n-links* where n represents neighbor. It is important to note that neighborhood is arbitrary and may include diagonal or other kinds of n-links. Edges that connect a non-terminal nodes to terminal nodes are named *t-links*. Every edge in the graph, $e \in \mathcal{E}$, is given some non-negative weight w_e. In Figure 2.4, edge weights are shown by the thickness of edges.

An s/t cut on the graph is defined as the subset of edges $Y \subset \mathcal{E}$ such that the terminal nodes s and t are completely separated on the induced graph $\mathcal{G}(Y) = \langle \mathcal{V}, \mathcal{E} \setminus Y \rangle$. A cut partitions the nodes into two disjoint subsets and divides image into object and background segments as shown in Figure 2.4.

The cost of a cut is defined as the sum of costs of the edges that the cut severs

$$|Y| = \sum_{e \in Y} w_e. \tag{2.26}$$

The *minimum cut* problem is defined as finding a cut that has the minimum cost among all [73].

According to a well-known result of combinatorial optimization, minimum s/t cut problem can be solved efficiently in polynomial time by finding maximum flow from source s to sink t [81]. This result is also known as the max-flow/min-cut theorem. To give the intuition behind, suppose the edges denote the directed pipes with capacities equal to edge weights. Then the maximum amount of water that could be sent from source to sink saturates some pipes and the saturated pipes divide the edges into two disjoint parts [72].

2.3.2. Segmentation Energy and Optimum Solution by Graph Cuts

In order to segment an image by graph cuts, an energy function must be formulated in terms of visual cues and this energy function must be embedded on a graph via n-links and t-links. Following [73], $\mathcal{P}$ denotes an arbitrary set of data elements such as pixels and $\mathcal{M}$ represents some neighborhood system of all unordered pairs $\{p, q\}$. For example, $\mathcal{M}$ can be consisted of all unordered pairs of pixels under a standard 8-neighborhood. In addition to that, $A = \{A_1, \ldots, A_p, \ldots, A_{|P|}\}$ is a vector which contains assignments A_p to pixels p in $\mathcal{P}$, thus A defines a segmentation. A segmentation cost function is formulated by forcing soft constraints on boundary, B(A), and region, R(A), properties of A as

$$E(A) = \zeta \cdot R(A) + B(A) \tag{2.27}$$

where

$$R(A) = \sum_{p \in \mathcal{P}} R_p(A_p) \tag{2.28}$$

$$B(A) = \sum_{\{p,q\} \in \mathcal{M}} B_{p,q} \cdot \delta_{A_p \neq A_q} \tag{2.29}$$

and

$$\delta_{A_p \neq A_q} = \begin{cases} 1 & \text{if } A_p \neq A_q, \\ 0 & \text{if } A_p = A_q. \end{cases} \tag{2.30}$$

In Equation 2.27, the relative importance between boundary and region terms are determined by the coefficient $\zeta \geq 0$. The regional term $R(A)$ represents the penalties for assigning every pixel p to object and background. Regional terms that are based on intensities of individual pixels are commonly used as proposed in [73]. Such a $R(.)$

is given as

$$R_p(\text{“}obj\text{”}) = -\ln P(I_p|\text{“}obj\text{”}) \quad (2.31)$$

$$R_p(\text{“}bkg\text{”}) = -\ln P(I_p|\text{“}bkg\text{”}) \quad (2.32)$$

where “obj” and “bkg” denote object and background respectively. Moreover, boundary term, $B(A)$, penalizes the discontinuities of segmentation A. For this purpose, coefficient $B_{p,q} \geq 0$, i.e. the corresponding n-link weight between nodes p and q, must be large when pixels are similar and close to zero when pixels are different. Therefore, a similarity measure have to be encoded in $B_{p,q}$, which could be based on local intensity gradient, Laplacian zero-crossing, gradient direction or other feature [73]. Generally, intensity based boundary penalties like

$$B_{p,q} \propto \exp\left(-\frac{(I_p - I_q)^2}{2\sigma^2}\right) \cdot \frac{1}{dist(p,q)}, \quad (2.33)$$

are utilized [73] where $dist(p,q)$ denotes Euclidean distance between pixels p and q.

In addition to the above soft constraints, it may sometimes be necessary to embed topological hard constraints into the segmentation energy. By utilizing hard constraints, some image pixels may be forced to be a part of the object or background. This procedure could successfully reduce the search space during minimization, thus supports the segmentation when regional properties of object and background are not distinct [73]. By hard constraints, the flexibility of interaction is also introduced in the segmentation process, since high level contextual information is provided. Following [73], suppose that $\mathcal{O} \subset \mathcal{P}$ and $\mathcal{B} \subset \mathcal{P}$ denotes the subset of pixels that are known to be a part of object and background respectively. These subsets does not overlap, $\mathcal{O} \cap \mathcal{B} = \emptyset$. Energy minimization problem defined in Equation 2.27 is constrained with

$$\forall p \in \mathcal{O} \ : \quad A_p = \text{“}obj\text{”}, \quad (2.34)$$

$$\forall p \in \mathcal{B} \ : \quad A_p = \text{“}bkg\text{”}. \quad (2.35)$$

Segmentation energy defined in Equation 2.27 with hard constraints given in Equations 2.34 and 2.35 have to be encoded in a s/t graph such that every feasible cut corresponds to a value of the energy function. As discussed in [73], assume that a graph $\mathcal{G} = \langle \mathcal{V}, \mathcal{E} \rangle$ is created with nodes corresponding to image pixels $p \in \mathcal{P}$. Two additional virtual nodes S and T describing object and background are also added to the graph. Therefore our vertices set becomes

$$\mathcal{V} = \mathcal{P} \cup \{S, T\}. \tag{2.36}$$

Each pixel p is connected to both source and sink terminals via t-links, $\{p, S\}$ and $\{p, T\}$. Furthermore, every pixel, p, is connected to its neighboring pixels, q, via n-links in a neighborhood $\mathcal{M}$. Thus, we obtain a set of edges $\mathcal{E}$ as

$$\mathcal{E} = \mathcal{M} \bigcup_{p \in \mathcal{P}} \{\{p, S\}, \{p, T\}\}. \tag{2.37}$$

In order to complete the graph building, one must also define edge weights for edge set $\mathcal{E}$. Following [73], edge weights could be given as in Table 2.1. K in Table 2.1 is defined as

$$K = 1 + \max_{p \in \mathcal{P}} \sum_{q:\{p,q\} \in \mathcal{M}} B_{p,q}. \tag{2.38}$$

In [73], it is also proven that the the minimum cut $\hat{Y}$ on graph $\mathcal{G}$ defines a segmentation $\hat{A}$, which is globally optimum. Suppose that $\mathcal{F}$ defines all *feasible* cuts such that

(i) Y severs exactly one t-link for each p,

(ii) $\{p, q\} \in Y$ if and only if p and q are linked to different terminals,

(iii) $\{p, T\} \in Y$ if $p \in \mathcal{O}$,

(iv) $\{p, S\} \in Y$ if $p \in \mathcal{B}$.

Table 2.1. Edge weights for graph $\mathcal{G}$.

Edge	**Weight (cost)**	**For**
$\{p, q\}$	$B_{p,q}$	$\{p, q\} \in \mathcal{M}$
$\{p, S\}$	$\lambda \cdot R_p(\text{“}bkg\text{”})$	$p \in \mathcal{P}, \quad p \notin \mathcal{O} \cup \mathcal{B}$
	K	$p \in \mathcal{O}$
	0	$p \in \mathcal{B}$
$\{p, T\}$	$\lambda \cdot R_p(\text{“}obj\text{”})$	$p \in \mathcal{P}, \quad p \notin \mathcal{O} \cup \mathcal{B}$
	0	$p \in \mathcal{O}$
	K	$p \in \mathcal{B}$

It is easy to show that the minimum cut on $\mathcal{G}$ is feasible, i.e. $\hat{Y} \in \mathcal{F}$. From the definition of minimum cut, we know that $\hat{Y}$ separates the terminals, thus it must sever at least one t-link for each pixel. On the other hand, $\hat{Y}$ can not severe both t-links for the sake of optimality. In other words, $\hat{Y}$ is not optimal in such a case since one t-link could be returned while keeping two terminal nodes separate. In addition to that, a minimum cut must sever n-link $\{p, q\}$ if p and q are connected to different terminal nodes because it must separate terminals. In order to be minimal, $\hat{Y}$ also should not severe any unnecessary n-links if p and q are connected to the same terminal. The requirements for n-links are guaranteed because the constant K is greater than the sum of all n-links' costs for any given pixel p. To give an example, suppose $p \in \mathcal{O}$ and $\hat{Y}$ severs $\{p, S\}$ that has a cost K. However, it would be minimal if $\hat{Y}$ restores $\{p, S\}$ and severs $\{p, T\}$ and all n-links from p, since the cost of n-links together are lower than K.

Moreover, one can extract a unique segmentation $A(C)$ for any feasible cut $Y \in \mathcal{F}$ such that

$$A_p(C) = \begin{cases} \text{“}obj\text{”}, & \text{if } \{p, T\} \in Y \\ \text{“}bkg\text{”}, & \text{if } \{p, S\} \in Y. \end{cases} \tag{2.39}$$

Using the weights in Table 2.1, the definition of feasible cuts $\mathcal{F}$ and Equation 2.39, cost of any cut Y could be written as

$$\begin{aligned} |Y| &= \sum_{p \notin \mathcal{O} \cup \mathcal{B}} \lambda \cdot R_p(A_p(Y)) + \sum_{\{p,q\} \in \mathcal{M}} B_{p,q} \cdot \delta_{A_p(Y) \neq A_q(Y)} && (2.40) \\ &= E(A(Y)) - \sum_{p \in \mathcal{O}} \lambda \cdot R_p(\text{“}obj\text{”}) - \sum_{p \in \mathcal{B}} \lambda \cdot R_p(\text{“}bkg\text{”}) && (2.41) \\ &= E(A(Y)) - const. && (2.42) \end{aligned}$$

In addition to that, Equation 2.39 determines one-to-one correspondence between the set of all feasible cuts $\mathcal{F}$ and the set of all assignments $\mathcal{H}$ that satisfy hard constraints given in Equations 2.34 and 2.35. Using Equation 2.42, the segmentation energy that is obtained by minimum cut could be written as

$$\begin{aligned} E(\hat{A}) &= |\hat{Y}| + const = \min_{Y \in \mathcal{F}} |Y| + const \\ &= \min_{Y \in \mathcal{F}} E(A(Y)) = \min_{A \in \mathcal{H}} E(A). && (2.43) \end{aligned}$$

In other words, the segmentation $\hat{A} = A(\hat{Y})$ defined by the minimum cut $\hat{Y}$ as in Equation 2.39 minimizes the segmentation energy given in Equation 2.27 among all segmentations satisfying the constraints given in Equations 2.34 and 2.35 and therefore, it is the optimal solution [73].

2.3.3. Relation to Markov Random Fields

Approaching the problem from a different standpoint, segmentation could be considered as a Bayesian labeling problem. In such a case, the optimal solution is given as the maximum a posteriori (MAP) probability estimation and is calculated by minimizing a posterior energy [71]. In other words, our goal is to estimate the best possible segmentation based on prior knowledge and observations.

Formally, as proposed in [71], assume that set $\mathcal{P} = \{1, \ldots, m\}$ denotes a set of sites corresponding to image pixels p. Also, let $\mathcal{L}$ correspond to a set of labels. Let

$F = \{F_p \mid p \in \mathcal{P}\}$ constitute a family of random variables defined on $\mathcal{P}$. Then, a joint event $\{F_1 = f_1, \ldots, F_m = f_m\}$ which is abbreviated as $F = f$ where $f = \{F_p \mid p \in \mathcal{P}\}$ describes a realization of F and is named as a configuration. Furthermore, suppose that we know a priori probabilities, $P(f)$, of configurations, and the likelihood densities,$P(I|f)$ of observations, where I denotes observations. The best estimate one could obtain in this case is the one that maximizes MAP. This posterior probability is calculated by Bayes' theorem

$$P(f|I) = \frac{P(I|f)P(f)}{P(I)} \tag{2.44}$$

where P(I) is the density function of I. However, it is difficult, sometimes even impossible, to model the joint probability $P(f)$. Luckily, Markov random field (MRF) theory simplifies the analysis to a great extent.

Adopting the notation in [71], let $\mathcal{M}$ define a neighborhood system for $\mathcal{P}$ as

$$\mathcal{M} = \{\mathcal{M}_i \mid \forall i \in \mathcal{P}\} \tag{2.45}$$

where $\mathcal{M}_i$ is the set of sites neighboring to i for which $i \notin \mathcal{M}_i$ and $i \in \mathcal{M}_j \iff j \in \mathcal{M}_i$. A *clique*, c, is a subset of $\mathcal{P}$ which contains a single site or a number of neighboring sites. The set of single-site cliques, two-site cliques, ..., is denoted by C_1, C_2, ... and the collection of all cliques is denoted by $C = C_1 \cup C_2 \ldots$. In order F to define a MRF on $\mathcal{P}$ with respect to $\mathcal{M}$, two conditions must be satisfied.

(i) *Positivity*: $P(F = f) > 0$, for all configurations,
(ii) *Markovianity*: $P(F_i = f_i | F_j = f_j,\ j \in \mathcal{P},\ j \neq i) = P(F_i = f_i | F_j = f_j,\ j \in \mathcal{M})$.

Markovianity condition states that the probability of a local event at i conditioned on all remaining events in $\mathcal{P}$ is equal to that conditioned on the events at the immediate neighbors of i. Moreover, according to Hammersley-Clifford theorem [82], F is an MRF on $\mathcal{P}$ with respect to $\mathcal{M}$ if and only if $P(F = f)$ is a Gibbs distribution with

respect to $\mathcal{M}$. Therefore, the prior probability, $P(f)$, could be written as

$$P(f) = \frac{1}{Z} \times \exp^{-U(f)/T} \tag{2.46}$$

where Z is a normalizing constant, T is a global control parameter called temperature and $U(f)$ is the *prior energy*. The prior energy is defined with respect to $\mathcal{M}$ and is of the form

$$U(f) = \sum_{c \in C} V_c(f) = \sum_{\{i\} \in C_1} V_1(f_i) + \sum_{\{i,j\} \in C_2} V_2(f_i, f_j) + \dots \tag{2.47}$$

with possible higher order terms. Note that the joint probability $P(f)$ may completely be specified by an appropriate selection of prior potentials $V_c(f)$ for all $c \in C$. Now, suppose likelihood $P(I|f)$ could be expressed as

$$P(I|f) = \frac{1}{Z_r} \times \exp^{-U(I|f)} \tag{2.48}$$

where $U(I|f)$ is called the *likelihood energy*. Then the posterior probability is a Gibbs distribution

$$P(f|I) = \frac{1}{Z_E} \times \exp^{-E(f)} \tag{2.49}$$

with *posterior energy*

$$E(f) = U(f|I) = U(f)/T + U(I|f). \tag{2.50}$$

Therefore, the MAP solution $\hat{f}$ could be found by

$$\hat{f} = \arg\min_f U(f|I). \tag{2.51}$$

Greig *et al.* [51] formulated the problem of restoration of binary images as a

Bayesian labeling problem and solved it using MAP-MRF framework. In that work, they showed that an appropriate selection of likelihood and prior energies could turn the problem into an energy minimization problem given in Equation 2.50 which is of the form given in Equation 2.27. They also showed that the energies of this kind could efficiently be minimized via s/t graph cuts. Recently, following the ideas of Greig *et al.* [51], Boykov *et al.* [83] showed how to use s/t graph cuts to obtain a MAP solution for a MRF that includes more than two labels.

3. SEGMENTATION OF 3D CT DATA

In this chapter, we are going to explain our liver segmentation algorithm, which is a combination of intensity distribution modeling, PAs and graph cuts. Each component of segmentation algorithm will be discussed in detail and the rationale behind the components and the comparison of components with other methods will be given.

First step in our segmentation algorithm is to find a rough initial segmentation of liver. Rough initial segmentation will be beneficial throughout the segmentation process, it is especially needed for the computation of PA and the calculation of boundary terms for graph cuts. In addition to that, our conservative initial segmentation serves as foreground hard constraints in graph cut segmentation. For this purpose, we have proposed an adaptive thresholding based on intensity distributions of the CT data. Intensity distribution modeling and adaptive thresholding will be discussed in Section 3.1.

As the intermediate step, we will discuss how to construct our novel probabilistic atlas with both initial segmentation and manual liver delineations in Section 3.2. PA calculated with our novel method is essential for supplying spatial information into segmentation. In that section, we will also overview other PA creation methods and compare them with our method.

Afterwards, we will continue by defining an energy minimization problem for liver segmentation. We will formulate the segmentation as an MRF on the grid of pixels in Section 3.3. In that section, we will also show how a convenient selection of terms in energy minimization formulation may lead to incorporate regional, spatial and boundary information into the segmentation process. Intensity, probabilistic atlas and boundary terms and their formulations will be explained in detail in Section 3.3.1, 3.3.2 and 3.3.3 consecutively. A flowchart of the overall algorithm is given in Figure 3.1.

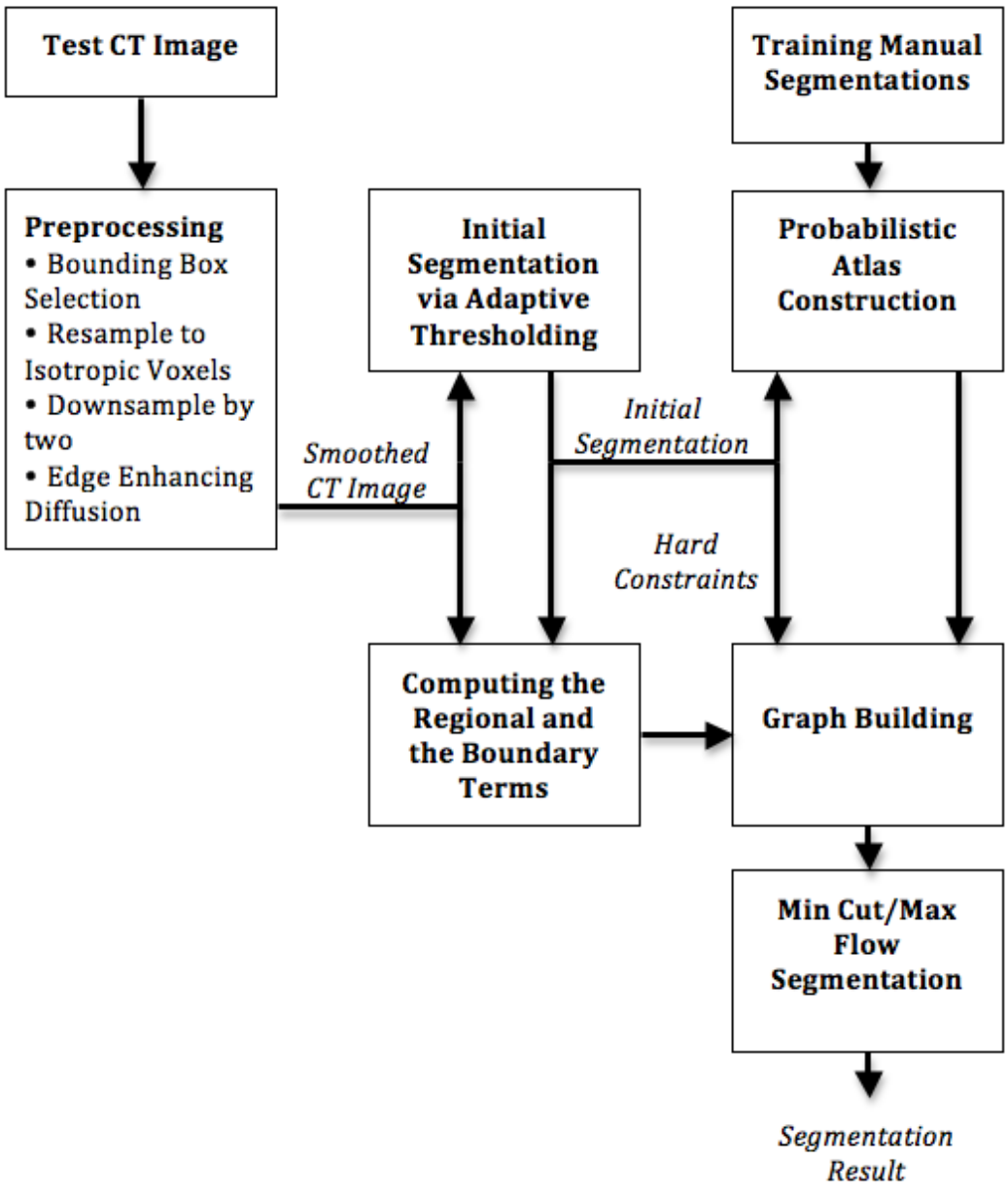

Figure 3.1. The flowchart of liver segmentation algorithm.

3.1. Initial Segmentation via Adaptive Thresholding

As we mentioned earlier, prior knowledge about shape and location of liver could be advantageous for assisting liver segmentation. Even a rough estimate of shape and location could be facilitated in more advanced methods. In our algorithm, it is used for defining the set of hard constraints in graph cut segmentation, personalized PA construction and edge map construction via boundary profile classification. For this purpose, a conservative initial segmentation of liver is needed. This conservative segmentation must not leak onto surrounding tissues since we do not want to introduce error from the beginning. In other words, our initial segmentation must have high specificity. In order to obtain an initialization, low level image processing algorithms such as thresholding is utilized. However, due to similar intensity values between adjacent organs, results of thresholding often have leakage. Thus, basic thresholding does not give intended results. In this section, we are going to explain in detail the applied adaptive thresholding whose adaptivity is formulated in terms of boundary estimates.

The intensity values of CT images are measured in terms of the Hounsfield scale. A Hounsfield unit (HU) is a measure of radiodensity which is defined as a linear mapping of the original attenuation coefficient measurement onto the radiodensity of distilled water at a standard pressure and temperature (STP) and radiodensity of air at STP. Radiodensity of distilled water at STP and radiodensity of air at STP is considered to be 0 and -1000 HU respectively. The attenuation coefficient for some structures and elements inside body is known. The voxel CT values defined in HU of air, fat, water, muscle, contrast material and bone are approximately known to be -1000 HU, -120 to -80 HU, 0 HU, 40 HU, 130 HU, 500 to 3000 HU respectively [84]. Therefore, it is possible to roughly extract a structure or an organ from CT images solely by utilizing the intensity values. Therefore, we propose to delineate healthy liver parenchyma via adaptive thresholding to obtain a conservative initial segmentation. A block diagram explaining the flowchart of initial segmentation is given in Figure 3.2.

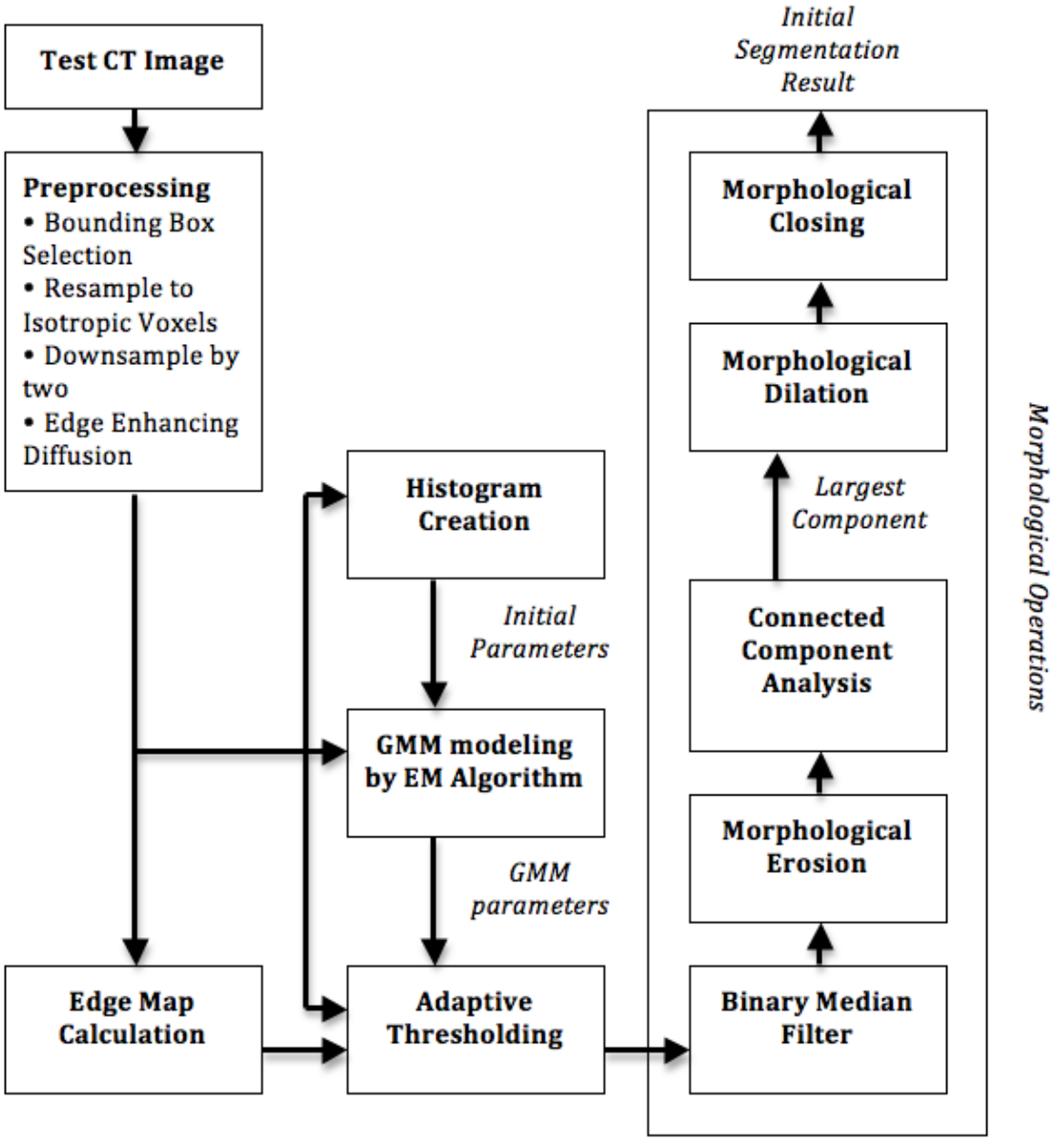

Figure 3.2. The flowchart of initial segmentation via adaptive thresholding.

As the first step of our initialization, a bounding box that contains the right part of the abdomen is selected manually. This bounding box defines a region of interest that completely encapsulates liver and partially gets rid of irrelevant structures inside abdomen. An example of a bounding box is shown in Figure 3.3. This step is necessary to get a reasonable conservative segmentation of the liver via thresholding the voxel values, where the thresholds are determined from a GMM model of the distribution of intensity values of voxels. Also, the size of the bounding box is further reduced by downsampling data by two. However, the inter-slice distance between two axial slices is already deficient in size and data loss may occur during downsampling unless precautions are taken. To solve this problem, the CT data in the bounding box is resampled with linear interpolation so that the voxel size became isotropic before downsampling.



(a) (b)

Figure 3.3. An example of bounding box. Bounding box is described by red lines in (a). A closer look into bounding box is given in (b).

The estimation of intensity distributions must not be effected by noise that is present in CT images. Moreover, we also need sharp boundaries across organs since we are going to utilize the edge estimates for adaptive thresholding. Therefore, not only to smooth the downsampled image but also to enhance the boundaries, we applied a 3D version of the edge enhancing diffusion filter described in Section 2.2.1. In three

dimension, the eigenvalues of diffusion tensor become

$$\begin{aligned} d_1(e_1) &= g(e_1), \\ d_2 &= 1, \\ d_3 &= 1 \end{aligned} \tag{3.1}$$

with $g(.)$ given in Equation 2.24. An example showing both the downsampled image and the result of edge enhancing diffusion filter is given in Figure 3.4.

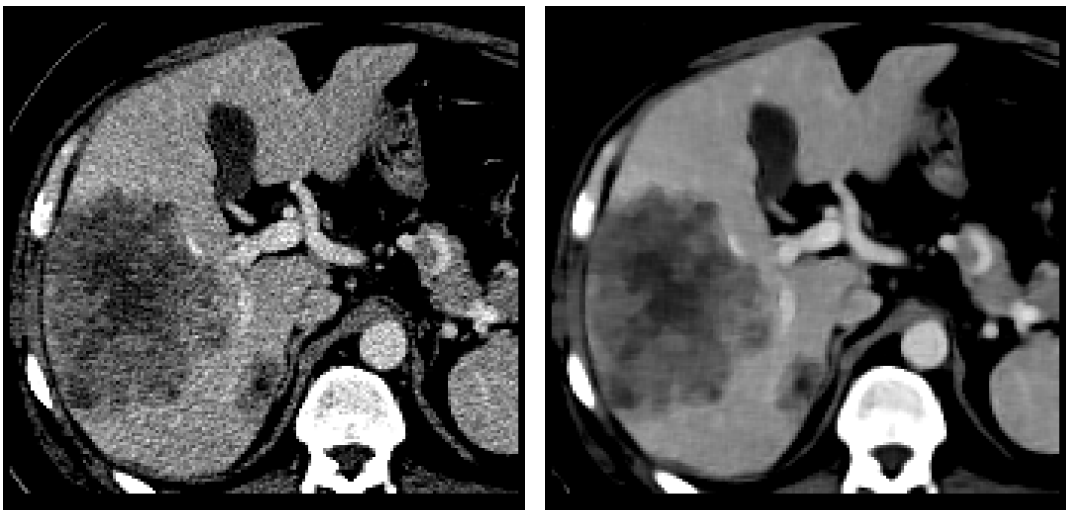

(a) (b)

Figure 3.4. Effect of edge enhancing diffusion. (a) Before and (b) after edge enhancing diffusion is applied.

Although the deviation of intensity values among different patients for some tissues or materials (such as water, fat, air) is small, generally it is not the case for organs such as liver, heart, kidneys and structures inside these organs such as tumors and veins. In order to obtain a personalized estimate of distribution of the intensity values in the edge enhanced data, we model the intensity value distribution inside the bounding box with a five component GMM. We decided to label these five components as gallbladder, soft tissue, liver, vessel and bone based on a priori information about HU values of these structures [10].

After edge enhancing diffusion, we created a histogram of intensity values in the smoothed image between minimum voxel intensity and maximum voxel intensity. Since it is known that liver is the largest organ on the right of the abdomen, the peak in the histogram is caused by liver and can easily be identified between 0 and 200 HU. The corresponding peak is named as *liver-peak*. The gallbladder contains liquid, so its intensity value is approximately zero and the intensity value of soft tissue lies in between the intensity values of gallbladder and liver. Thus the corresponding peaks are identified. Investigating the histogram, it is observed the frequency values get sufficiently small after some intensity value. We have selected an *upper-bound* value and defined as the intensity value where the corresponding frequency value gets below a certain threshold. The intensity values of vessel and bone are between intensity value of liver and upper-bound with latter having a greater intensity value. Thus, the remaining two peaks are identified. Also, we defined a *lower-bound* value and set it to zero since there can be no voxels that belongs to tissue and have a intensity value lower than zero. It is crucial to point out that the distribution we want to model via GMM includes only those voxels with intensity values between lower-bound and upper-bound. According to the above observation, the EM algorithm is initialized manually and component estimates are found. Each component is labeled according to the initial estimates of mean intensity values of five components. An example distribution and Gaussian component estimates are shown in Figure 3.5.

Along with GMM modeling, the edge estimates are computed with

$$g(\|\nabla I\|) = \frac{\eta}{1 + \left(\frac{\|\nabla I\|}{\lambda}\right)^{(1+\alpha)}} \tag{3.2}$$

where $\|\nabla I\|$ denoting the magnitude of gradient of the image $\alpha > 0$, η and λ are constants. The function $g(\|\nabla I\|)$ is called the *edge map* of the image and has an approximate value of zero near edges and one if there is no edge information. In our convention, the value of the function $g(\|\nabla I_p\|)$ is named as *edgeness* at voxel p. We have chosen a small $\lambda = 4$ so that we get small values for edgeness if the gradient

magnitude is small. In other words, both sharp and weak boundaries are treated likewise. It is important to note that the so called edge map is blind to the organs or structures.

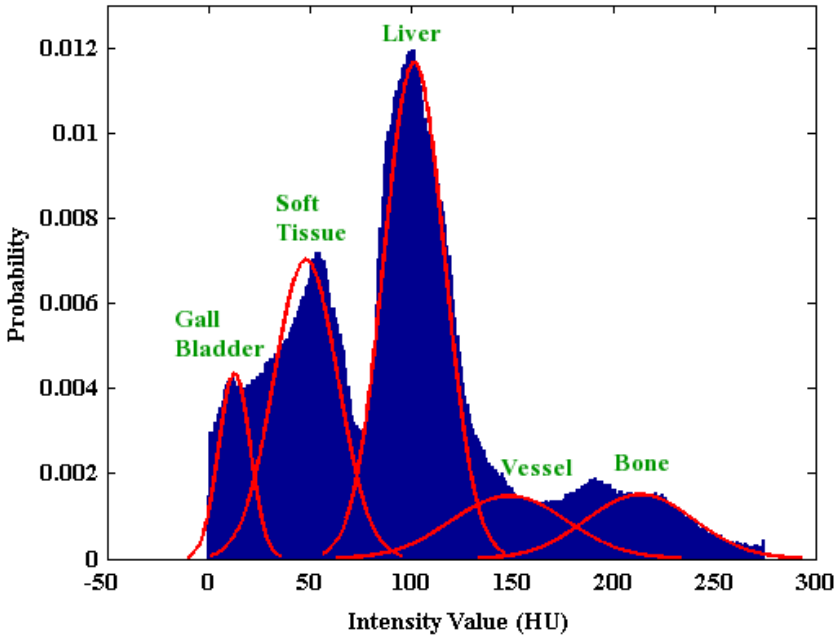

Figure 3.5. An example of GMM estimates. Estimates are shown in red with corresponding labels above.

Afterwards, to delineate only the healthy liver tissue, we used spatially varying adaptive thresholding. The spatial adaptivity is defined in terms of the above edge estimates. Formally, we selected two static threshold values, τ_{low} and τ_{high} based on GMM component estimates such that

$$\tau_{low} = \mu_{liver} - 1.5 \times \sigma_{liver}, \tag{3.3}$$

$$\tau_{high} = \mu_{liver} - 3.0 \times \sigma_{liver}. \tag{3.4}$$

As one could note, the low threshold value is more strict than the high threshold value to get a highly specific conservative segmentation since the intensity values of soft tissue and liver is generally much closer than intensity values of liver and vessels.

Moreover, in order to prevent leakage into adjacent organs, thresholding must respect the boundaries even if gradient response is not high. To satisfy the above requirements, the spatial adaptivity is introduced via two adaptive threshold values such that

$$\tau_{low_adaptive}(I_p) = \mu_{liver} - ((\mu_{liver} - \tau_{low}) \times g(\|\nabla I_p\|)), \quad (3.5)$$

$$\tau_{high_adaptive}(I_p) = \mu_{liver} + ((\tau_{high} - \mu_{liver}) \times g(\|\nabla I_p\|)). \quad (3.6)$$

The selection of $\tau_{low_adaptive}$ and $\tau_{high_adaptive}$ could be interpreted as narrowing the thresholding interval near edges, so as to include only the voxels that we are confident about in the segmentation. Results of adaptive thresholding is given in Figure 3.6c for a healthy liver and in Figure 3.6a for a tumorous liver.

As the post-processing step, we applied a set of morphological operations. First, a binary median filter of radius $3\times3\times3$ is applied to emend ragged thresholding results. Then, a morphological opening operation is performed with a radius $4 \times 4 \times 4$. In that morphological opening, we also employed a connected component analysis between the morphological erosion and dilation. During that operation, we selected the largest binary component as the liver and erased the other small components before dilation. As the final step, we used a morphological closing operation of radius $1 \times 1 \times 1$ in order to fill small gaps in the final result. Results after morphological operations are shown in Figure 3.6d for a healthy liver and in Figure 3.6b for a tumorous liver.

3.2. Probabilistic Atlas Construction

Both shape and spatial information about liver is integrated into the segmentation task via probabilistic atlases. There is a vast body of literature on liver probabilistic atlases that mainly focus on two aspects of PAs [3,6–9,28,29,50]: The construction of PA and the incorporation of PA into segmentation. The solutions for the former problem are mainly divided into two groups. In the first group of algorithms, PA is constructed by registering all images in the training set onto a pre-selected image or onto the image to be segmented. In this step several measures such as mutual infor-

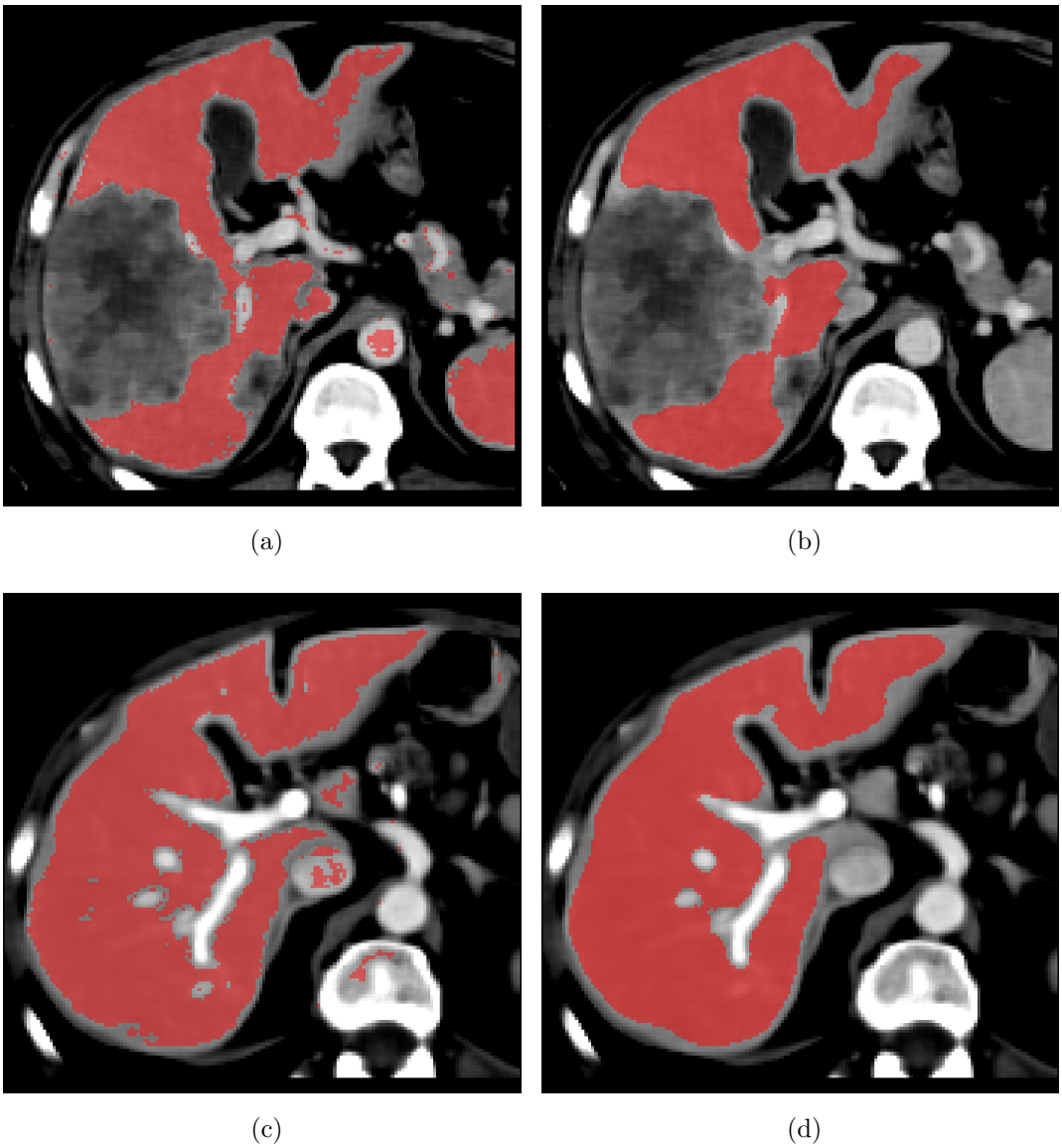

(a) (b)

(c) (d)

Figure 3.6. Results after adaptive thresholding and morphological operations. (a) and (c) show adaptive thresholding results. (b) and (d) show the results obtained after morphological operations.

mation (MI) [6], normalized MI [3], surface distance penalty [8] are used along with various nonrigid transforms like thin plate spline (TPS) [6], B-Spline [3, 8]. Then, if a pre-selected image is used, manual segmentations are transformed onto the label of this image and averaged to obtain a PA. If training images are directly registered onto the image to be segmented, manual segmentations are warped and averaged to get PA. In the second group of algorithms, training images are registered onto a standard anatomical structure that have rigid characteristics. Some of these anatomical structures are bone-diaphragm dual [7], abdominal cavity [28], average liver shape [29], rib cage [50], and xiphoid [9]. In this class of algorithms, point based registration are broadly used [6, 7, 28, 29]. In addition to that, Linguraru *et al.* [9] use proximal anatomical structures just to normalize organ coordinates and nonrigid B-spline transform with MI is used afterwards. A different approach is also presented in [50]. In this work, manual segmentations of both liver and rib-cage is used instead of intensity images to construct a PA.

Depending on the construction strategy, the results of PA based segmentation methods reveal several problems. First of all, it has been suggested that the variability of training images could further be exploited by registering each training subject to test subject separately [85]. Although this reasoning is proven to be true, the PAs constructed in this way are still incapable of segmenting unusual cases [3]. This problem could be surpassed by decreasing the degrees of freedom (DOF) of the transformation employed, since the variance of the atlas increases as we decrease the DOF of the transform [6]. The second problem encountered during PA construction is the local failure of intensity based registrations, where similar intensity values of different organs are close to each other [8]. In order to avoid these pitfalls, we propose a construction strategy that registers binary pseudo-convex hulls of both initial segmentation and manual delineations via affine transformation. A flowchart of the novel PA construction is given in Figure 3.7.

As mentioned in Section 1.1, shape of the liver could be described by a right angled triangular prism that have three surfaces. The superior and posterior sur-

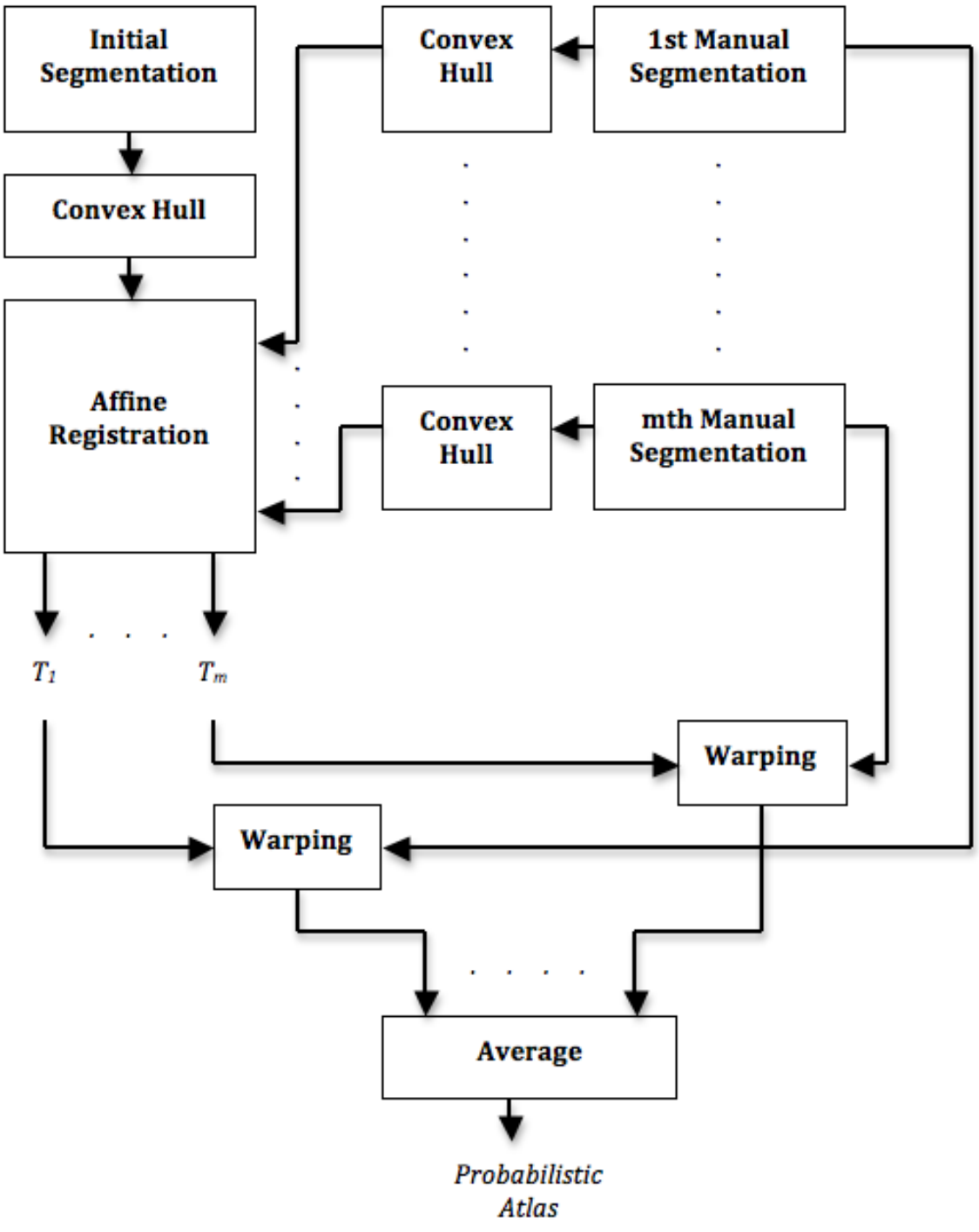

Figure 3.7. The flowchart of probabilistic atlas construction.

faces have definite characteristics such that they are mainly convex surfaces. On the contrary, the inferior surface is uneven due to impressions and fossae introduced by surrounding organs and structures. Our idea for constructing PA is to register manual delineations onto the initial segmentation by only the help of surfaces with rigid characteristics. By using manual delineations instead of intensity images, we are also able to evade the local failure problems. Furthermore, the inferior surface of liver is needed to be amended so that eminences and cavities does not effect the registration process. In order to achieve this goal, we propose to correct initial segmentation result to obtain a convex hull of it. Formally, suppose that we have m training manual delineations, $\{L_n\}$, along with their convex hulls, $\{\theta_n\}$, where $n = 1 \dots m$. One way to obtain convex hull is to use min flow [86]. Suppose that a binary mask is represented by signed distance function ϕ such that interior of binary mask has negative values and exterior has positive values. Min flow is defined as the evolution of the embedding level set function, ϕ, with

$$\phi_t = \min(\kappa, 0)|\nabla\phi| \tag{3.7}$$

where κ denotes the mean surface curvature. This equation moves concave regions with positive speed in normal direction to outwards. Along with that it also suppresses the evolution of convex regions. The motion would stop as soon as the convex hull is obtained. Therefore, the convex hull is attained while preserving the structure of convex regions. We could use an identical motion to get convex hull of the initial segmentation θ_{ini}. Since we stop evolution after a fixed number of iterations, we obtain pseudo-convex hulls. An example of initial segmentation and its corresponding pseudo-convex hull is shown in Figure 3.8.

Furthermore, let Ω be the finite grid where the initial segmentation is defined. An affine transform that warps θ_n onto θ_{ini} is a map $T_n : \Omega \mapsto \mathbb{R}^3$ such that $T_n(\boldsymbol{x}) = H\boldsymbol{x}+\boldsymbol{y}$ for all $\boldsymbol{x} \in \mathbb{R}^3$ where H is a linear transformation of $\mathbb{R}^3$ and $\boldsymbol{y}$ is any translation vector. In order to find parameters of T_n, we employed a gradient descent optimization scheme with regular step sizes and used mean squared pixel-wise difference between

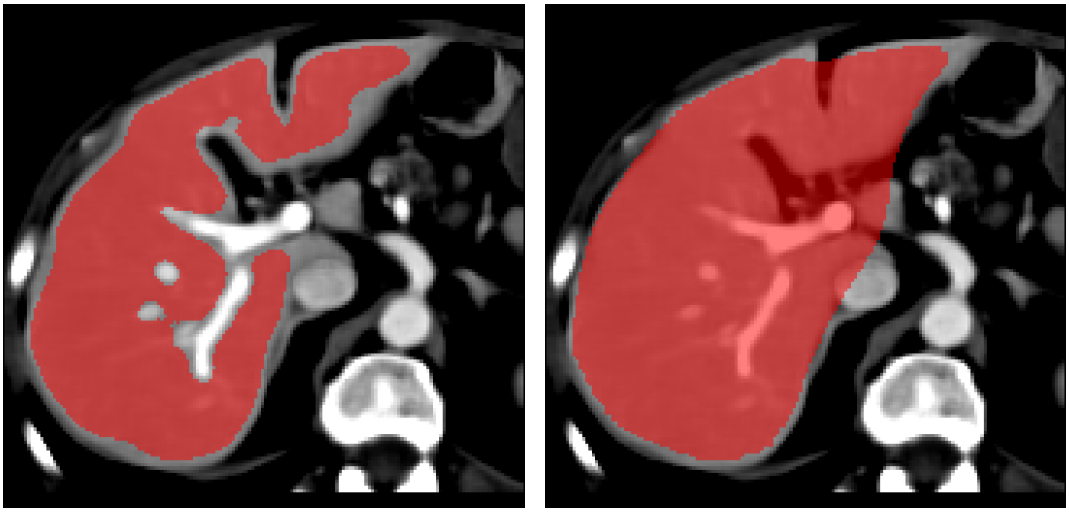

(a) (b)

Figure 3.8. An example of the pseudo-convex hull. (a) Initial segmentation and (b) pseudo-convex hull of initial segmentation.

binary masks (θ) as the metric.

After obtaining all transformations that warps θ_n onto θ_{ini}, we performed these transformations onto L_n and averaged the transformed manual delineations $T_n(L_n)$ to construct the PA. A probabilistic atlas calculated with our novel strategy is given in Figure 3.9.

3.3. Graph Building

To segment liver via graph cuts, segmentation problem must be formulated in terms of energy minimization. As already discussed in Section 2.3.3, defining the segmentation as a Bayesian labeling problem is a reasonable candidate for this purpose. In addition to that, in this section we will also show that it inherits ways to incorporate regional, boundary and a priori shape information.

Recalling the notation in Section 2.3.3, let set $\mathcal{P} = \{1, \ldots, m\}$ denote a set of sites corresponding to image pixels p. Also, let $\mathcal{L}$ correspond to the of labels $\{0, 1\}$

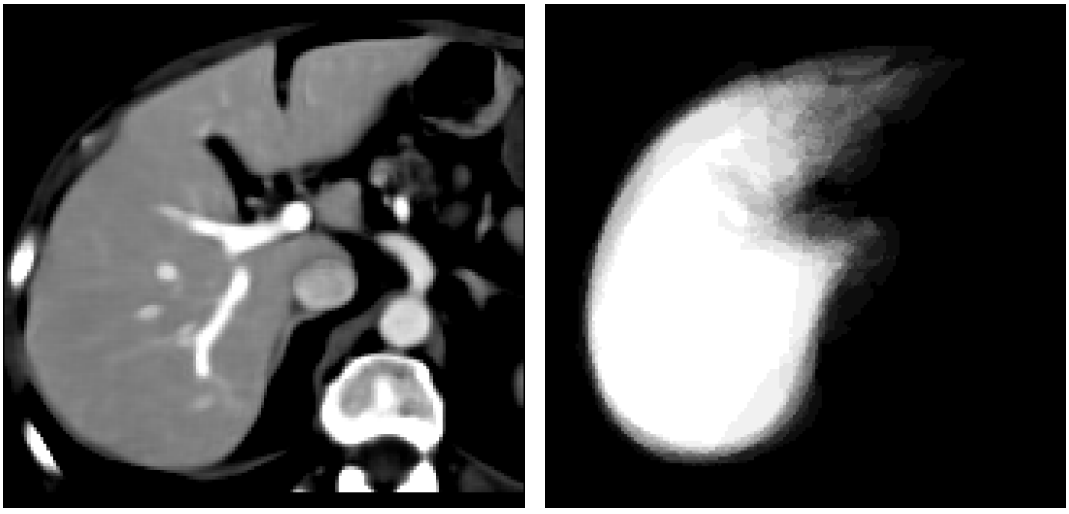

(a) (b)

Figure 3.9. An example PA constructed with proposed method. (a) Original image and (b) corresponding PA.

that denote background and foreground respectively. $F = \{F_p \mid p \in \mathcal{P}\}$ constitutes a family of random variables defined on $\mathcal{P}$. Then, a joint event $\{F_1 = f_1, \ldots, F_m = f_m\}$ which is abbreviated as $F = f$ where $f = \{F_p \mid p \in \mathcal{P}\}$ describes a realization of F. Furthermore, suppose that we know a priori probabilities, $P(f)$, of configurations (segmentations), and the likelihood densities, $P(I|f)$ of observations, where I denotes the observations (voxel intensities). It is discussed that the best estimate one could obtain in this case is the one that maximizes MAP. This posterior probability is calculated by Bayes' theorem and proportional to

$$P(f|I) \propto P(I|f)P(f). \tag{3.8}$$

We also know that the MAP solution $\hat{f}$ to Equation 3.8 is given by minimizing the posterior energy

$$\hat{f} = \arg\min_f \left(-\ln P(I|f) - \ln P(f)\right) \tag{3.9}$$

$$\hat{f} = \arg\min_f \left(E_{regional}(I,f) + E_{boundary}(I,f) + E_{prior}(f)\right). \tag{3.10}$$

In order to solve the above equation, one must model the likelihood and the prior probabilities.

Assume that the joint probability $P(f)$ is modeled with a MRF on $\mathcal{P}$ with a neighborhood system $\mathcal{M}$. Therefore, as discussed in Section 2.3.3, $P(f)$ is of the form

$$P(f) = \frac{1}{Z} \times \exp^{-\sum_{c \in C} V_c(f)/T} \tag{3.11}$$

where Z is a normalizing constant, T is a global control parameter called temperature and $\sum_{c \in C} V_c(f)$ is the prior energy. The joint probability $P(f)$ represents our prior knowledge about the labeling problem. Therefore any information that is known beforehand could be integrated to posterior energy in terms of cliques. In our case, a priori spatial location of liver comes from probabilistic atlas. It is defined as

$$E_{prior}(f) = \sum_{c \in C} V_c(f) = \sum_{p \in C_1} V_1(f_p). \tag{3.12}$$

We will show that by an appropriate selection of prior potential V_1, we will be able to integrate spatial information. This issue will be discussed in detail in Section 3.3.2.

Modeling of likelihood term $P(I|f)$ is another source of concern. $P(I|f)$ represents the likelihood of observations. In our situation, I denotes the observed intensities and $P(I|f)$ tries to model intensity distribution of liver, together with any structure it may encapsulate. We will discuss this term more in Section 3.3.1. Also, $P(I|f)$ tries to model boundary information which will be further discussed in Section 3.3.3.

3.3.1. The Intensity Term

The regional energy $E_{regional}$ in Equation 3.10 is a function of the total likelihood for all voxels. Assuming that the observed voxel values are independent for all $p \in \mathcal{P}$,

image likelihood could be written as the product of likelihoods of single voxels:

$$P(I|f) = \prod_{p \in (\mathcal{P})} P(I_p|f_p). \tag{3.13}$$

Then the regional energy term in Equation 3.10 could be rewritten as

$$E_{regional}(I, f) = -\sum_{p \in (\mathcal{P})} \ln P(I_p|f_p). \tag{3.14}$$

Given that a voxel has a foreground label, $f_p = 1$, it could belong to liver parenchyma, vessel or tumor. Because of this reason, $P(I_p|f_p = 1)$ could be modeled using the corresponding GMM components that will be discussed below. However, we do not possess the intensity distribution of tumor explicitly. Instead, we know that intensities of tumor generally lies somewhere between the intensities of soft tissue and gallbladder. In any case, including tumor distribution into regional energy could lead to misclassification between tumor and soft tissue, thus this procedure could cause leakage onto soft tissue. Therefore, we propose to use a two component GMM whose components correspond to liver tissue and vessel. The distribution parameters of both Gaussians are supplied by the EM step in initial segmentation. On the other hand, given that a voxel has a background label, $f_p = 0$, we need to model a complex distribution. To abstain from this situation, we simply define $P(I_p|f_p = 0) = 1 - P(I_p|f_p = 1)$. To summarize our proposal, $P(I_p|f_p)$ is given by

$$\begin{aligned} P(I_p|f_p = 1) &= \frac{\pi_{liver}}{\pi_{liver} + \pi_{vessel}} \exp^{\left(-\frac{1}{2}\frac{(\mu_{liver} - I_p)^2}{\sigma^2_{liver}}\right)} \\ &\quad + \frac{\pi_{vessel}}{\pi_{liver} + \pi_{vessel}} \exp^{\left(-\frac{1}{2}\frac{(\mu_{vessel} - I_p)^2}{\sigma^2_{vessel}}\right)} \end{aligned} \tag{3.15}$$

$$P(I_p|f_p = 0) = 1 - P(I_p|f_p = 1) \tag{3.16}$$

where π_{liver}, π_{vessel}, μ_{liver}, π_{vessel}, σ_{liver} and σ_{vessel} were determined by the EM algo-

rithm in initialization step.

3.3.2. The Probabilistic Atlas Term

By constraining ourselves into one and two site cliques $E_{prior}(f)$ term in Equation 3.10 becomes

$$E_{prior}(f) = -\ln P(f) = \sum_{p \in C_1} V_1(f_p) \tag{3.17}$$

E_{prior} is defined by one site clique potentials and represents the spatial distribution of the class labels. Therefore, PA could be integrated into segmentation energy by the help of E_{prior}. The PA assigns some probability value to every voxel location p. In other words, every voxel is given a value for probability of being foreground. Therefore, we could define one site clique potential as

$$V_1(f_p) = -\ln P_v(p) \tag{3.18}$$

where $P_v(p)$ denotes the value of the probabilistic atlas at voxel p. Note that if $P_v(p) = 0$, then voxel v must belong to background to minimize the energy function and vice versa. In other words, when $P_v(p) = 0$, our segmentation must be inside the region defined by voxels $\{p \mid p \in P_v(p) \neq 0\}$. Therefore, certain values of probabilistic atlas could constrain our segmentation. To avoid such situation, we simply limit the values of $P_v(p)$ into an interval defined by two threshold, i.e.,

$$\widehat{P}_v(p) = \begin{cases} \tau_{vote_low}, & \text{if } P_v(p) < \tau_{vote_low} \\ P_v(p), & \text{if } \tau_{vote_high} \leq P_v(p) \leq \tau_{vote_high} \\ \tau_{vote_high}, & \text{if } P_v(p) > \tau_{vote_high} \end{cases} \tag{3.19}$$

With this definition E_{prior} becomes

$$E_{prior}(f) = -\sum_{p \in \mathcal{P}} \ln \widehat{P}_v(f_p). \tag{3.20}$$

3.3.3. Boundary Term

The second term in Equation 3.10 namely $E_{boundary}$ is defined over two site cliques and models the relation between neighboring pixels. Therefore, it is a natural candidate to incorporate boundary properties of segmentation. Following the suggestion in [73], we defined the two cite clique potential as

$$V_2(f_p, f_q) = B_{p,q} \cdot \delta_{f_p \neq f_q} \tag{3.21}$$

where δ function is defined in Equation 2.30. In accordance with this definition, we can rewrite the $E_{boundary}$ as

$$E_{boundary}(f) = \sum_{\{p,q\} \in \mathcal{M}} B_{p,q} \cdot \delta_{f_p \neq f_q} \tag{3.22}$$

where $\mathcal{M}$ denotes the neighborhood. Thus integrating boundary information boils down to defining $B_{p,q}$ term in the above equation.

According to the definition of boundary energy, $B_{p,q}$ must be close to zero when there is a meaningful discontinuity in the image. Generally, these discontinuities in an image are evaluated with their derivative responses. Gradient magnitude of the image is a popular choice for edge detection. In fact, any measure that is based on intensity differences could be used. With that observation, most of the graph cut based methods rely on the boundary energy suggested in [73] and given in Equation 2.33. A different and interesting edge detection approach is presented in [52]. In that study, gradient tensor for every voxel is calculated with local gradients and non-linearly averaged to obtain a structure tensor. A surfaceness measure is defined in terms of the eigenvalues of the structure tensor and minimum surfaceness measure is assigned as the cost of the graph link between neighboring voxels. Although this procedure has edge enhancement properties to some extent, it is still based on the gradient information in the beginning and gradients are weak in ambiguous edges between organs that have similar intensity values.

To approach the problem from a different view, one could consider edge detection schemes in SSMs. A common method to sample intensity profiles in the direction of the normal vector of the surface at each landmark point for all training images. Then, assuming a normal distribution, mean and variances of training profiles are calculated. For a test profile, the probability of being in the boundary is computed using the Mahalanobis distance [18]. It is claimed that ordering of gray values in the boundaries gain importance between structures with similar intensities [87], therefore intensity profile based methods outperforms gradient based methods. However, optimality of this procedure is criticized, since complex distributions of profiles are often present in medical images. Profiles sampled from the liver boundary is shown in Figure 3.10. To overcome this shortcoming, k-nearest neighbor (kNN) appearance models are proposed [32] as a non-linear option. Along with true boundary profiles, additional non-edge false profiles are sampled at positions shifted along the edge normals. Then, k nearest neighbors of query profile in the training set are found using L_2 norm. Boundary probabilities are assigned by calculating the percentage of true edge profiles among k. In other words, estimated probability at voxel p is given by

$$P_b(p) = \frac{\text{number of true edge profiles}}{k}. \tag{3.23}$$

On the other hand, the intensity profiles mentioned above paragraph are calculated on the surface of SSM and it is not straightforward to utilize this procedure in any other method. Luckily, an implicit counterpart is proposed in [11]. In that work, a narrowband around the current zero level set of the signed distance function (SDF), ϕ, is created. Then, for every pixel in the narrowband a profile orientation is extracted from ϕ as the normal direction, $\nabla\phi$, of SDF. Afterwards, the query profiles are sampled in the profile directions and probabilities are estimated using the kNN appearance model. Finally, all boundary candidates are projected back via gradient descent (or ascent) onto the current level set. For each point in current level set, only the point with the highest probability is kept. Although this procedure is reason-

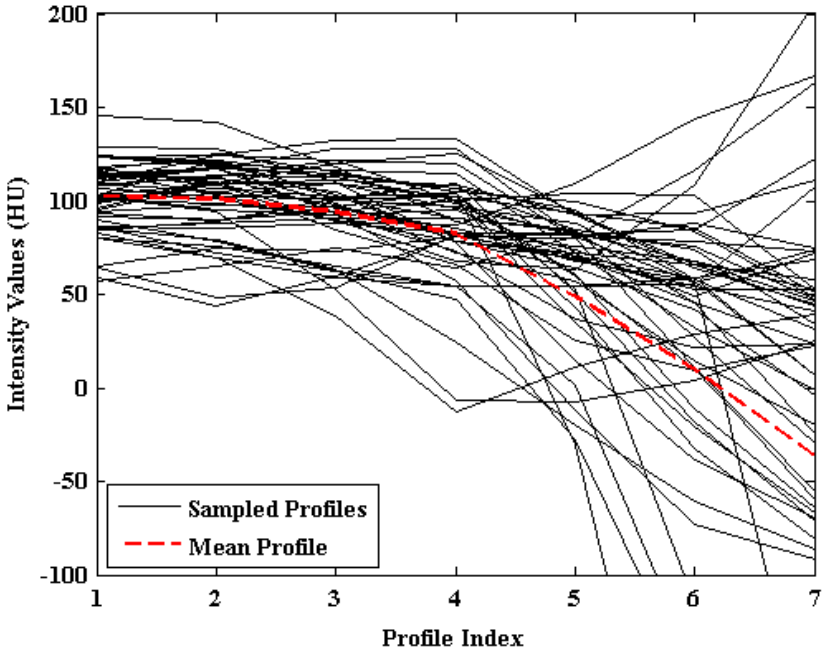

Figure 3.10. Profiles sampled from the liver boundary. Mean profile is given in red.

able for iterative level set based methods, it is still not eminent how to utilize kNN appearance model in graph cut segmentation.

In order to utilize the procedure depicted in [11], we need an initial segmentation from which profile orientations could be extracted. Fortunately, initial segmentation is already calculated and a SDF ϕ_{ini} could be calculated such that interior of binary mask has negative values and exterior has positive values. However, with this setup, we are unable to detect edges of liver surface if there is a tumor on the boundary of the liver. An example of this situation is given in Figure 3.11. It is clear from Figure 3.11, that no prominent edge response is obtained from tumorous surface of the liver. This problem occurs because of the reason that both our initial segmentation and SDF is deficient in those regions. Thus, the isosurfaces of SDF does not coincide with the surface of the liver as intended. In other words, SDFs propagate the deficient parts of zero level set throughout the domain. Therefore, the concavity caused by the tumor in initial segmentation is propagated to liver boundary. As a result, extracted

profile orientations does not reflect the structure of the liver surface. An example of normals of SDF function is given with the liver surface in Figure 3.12a. Note that in order not to introduce any error from profile orientations, normals that define profile orientations and liver surface normals must be parallel to each other.

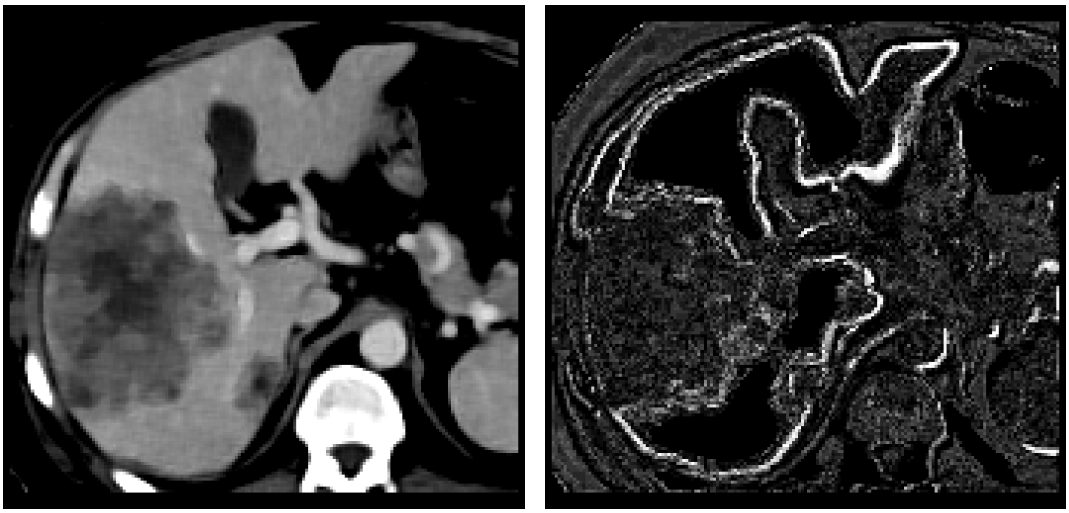

(a) (b)

Figure 3.11. Edge detection failure due to tumor. (a) Liver image and (b) Edge probabilities.

Recently, a novel implicit shape representation based on Poisson equation is proposed [88]. In that study, it is shown that the solution of the Poisson equation with a given shape (the initial segmentation in our case) as the boundary reveals the expected time for a symmetric random walk to reach the shape boundary. By the smoothness properties of random walks, the variations in the boundaries attanuated at an exponential rate unlike the signed distance transform. Therefore, Poisson equation based shape representation could be an alternative for obtaining profile directions.

Following [88], let $\varphi(x, y, z)$ represent the expected random walk hitting time for a particle starting inside an open region $\mathcal{S}$ in order o reach any point in the boundary of $\mathcal{S}$, $\partial\mathcal{S}$. Thus, $\varphi(x, y, z) = 0 \quad \forall(x, y, z) \in \partial\mathcal{S}$. At every point in $(x, y, z) \in \mathcal{S}$, $\varphi(x, y, z)$ is equal to the average value of its immediate six neighbors plus a constant. This constant denotes the amount of time required to get to an immediate neighbor.

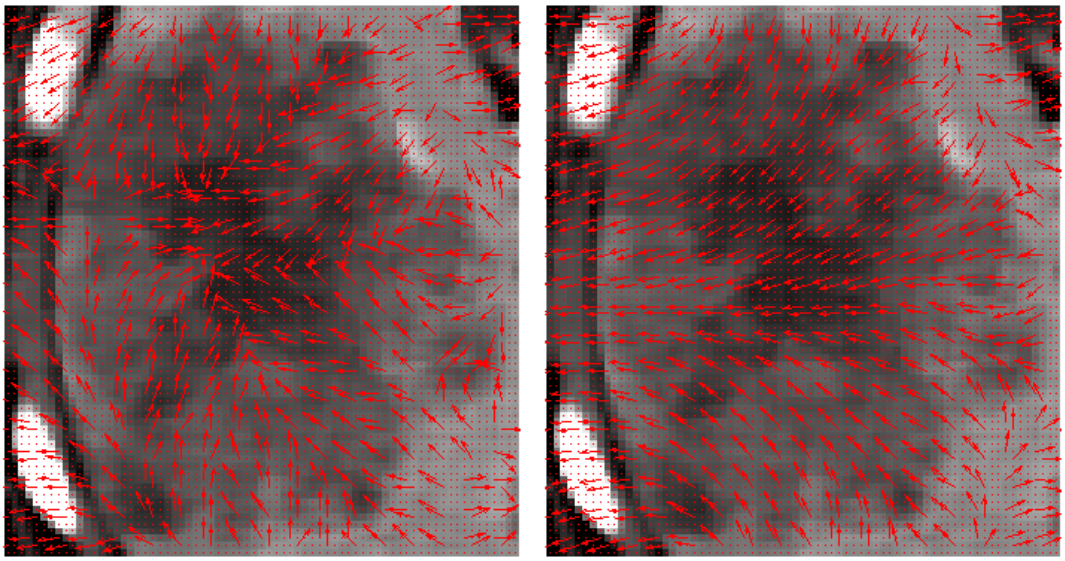

(a) (b)

Figure 3.12. Normals defined by (a) SDF and (b) solution of the poisson equation.

In other words,

$$\begin{aligned}\varphi(x,y,z) = 1 + \frac{1}{6}\Big(&\varphi(x+h,y,z) \quad + \quad \varphi(x-h,y,z) \\ &\varphi(x,y+h,z) \quad + \quad \varphi(x,y-h,z) \\ &\varphi(x,y,z+h) \quad + \quad \varphi(x,y,z-h)\Big)\end{aligned} \tag{3.24}$$

which is the discrete for of the Poisson equation

$$\Delta\varphi(x,y,z) = -\frac{6}{h^2} \tag{3.25}$$

where $\Delta\varphi$ represents the Laplacian of φ and h denotes a spatial unit. Without loss of generality, h could be set as one and Equation 3.25 could be rewritten with boundary condition as

$$\begin{aligned}\Delta\varphi(x,y,z) &= 6 \qquad \forall(x,y,z) \in \mathcal{S} \\ \varphi(x,y,z) &= 0 \qquad \forall(x,y,z) \in \partial\mathcal{S}\end{aligned} \tag{3.26}$$

On the exterior of the shape, random walk analogy fails and Poisson equation has infinitely many solutions as pointed out in [89]. Therefore, we need an external boundary condition. One could enforce Neumann boundary conditions on $\partial\Omega$, where Ω denotes the finite grid that image is defined. However, this choice results in undesirable behaviour of gradient at the image boundaries [89]. Following the idea in [89], we selected an open sphere $\mathcal{T} \supset \overline{\Omega}$ centered at the centroid of Ω and solve the Poisson equation defined as

$$\begin{aligned} \Delta\varphi(x,y,z) &= -6 \qquad \forall(x,y,z) \in \mathcal{T} - \overline{\mathcal{S}} \\ < \nabla\varphi(x,y,z), n(x,y,z) > &= 0 \qquad \forall(x,y,z) \in \partial\mathcal{T} \\ \varphi(x,y,z) &= 0 \qquad \forall(x,y,z) \in \partial\mathcal{S} \end{aligned} \tag{3.27}$$

where $n(x,y,z)$ is the outward normal vector to the surface $\partial\mathcal{T}$ at (x,y,z). In other words, Poisson Equation is solved via Neumann boundary conditions defined on a sphere.

Calculating φ is achieved in linear time by multigrid algorithms [88]. In this work, we extended this multigrid solver such that it calculated φ inside region $\mathcal{T} - \overline{\mathcal{S}}$. For this purpose we calculate the approximate normals on the surface of T and defined a correspondence between interior and exterior surface voxels according to normal direction. During multigrid solver iterations, we copied interior voxels to exterior voxels whenever Neumann conditions on $\mathcal{T}$ is necessary. By this way, the gradient of the solution in the direction of normal vectors of $\partial\mathcal{T}$ remained as zero.

The isocontours of φ is given in Figure 3.12b reveal that Poisson equation based shape representation is a better candidate for selecting profile orientations. These orientations could be selected in a similar manner and defined as the normal direction of the Poisson equation's solution, i.e. $\nabla\varphi$.

The integration of probabilities calculated with kNN appearance model into graph cut framework is another challenge as edgeness values are computed for nodes

of the graphs, not edges. The most straightforward solution is to give the minimum of the probabilities of neighboring voxels to $B_{p,q}$. However, this configuration gives possibly under-segmented results since the boundary of the liver surface is not included in the segmentation. Another possibility is to utilize probabilities calculated with kNN appearance model along with intensity difference based edge detectors. Following the idea [90], $B_{p,q}$ could be defined as

$$B_{p,q} = \eta B^I_{p,q} + (1-\eta) B^B_{p,q} \tag{3.28}$$

where η is a constant. $B^B_{p,q}$ and $B^I_{p,q}$ are given as

$$\begin{aligned} B^B_{p,q} &= \min(-\ln(P_b(p)), -ln(P_b(q))) \\ B^I_{p,q} &= 1/(1+\nu) \end{aligned} \tag{3.29}$$

where ν is the Lorentzian error norm and defined as

$$\nu(p,q) = \ln\left(1 + \frac{1}{2}\left(\frac{|I_p - I_q|}{\xi}\right)^2\right) \tag{3.30}$$

where I_p and I_q denotes image intensity at voxels p and q and ξ is the robust scale. However, this proposal includes two additional parameters into segmentation process. In order to avoid this situation, we propose to define $B_{p,q}$ as

$$\begin{aligned} B_{p,q} &= -\ln(P_b(p)) \qquad \text{if } \cos\theta_{pq} \geq \cos\theta_{qp} \\ B_{p,q} &= -\ln(P_b(q)) \qquad \text{if } \cos\theta_{pq} < \cos\theta_{qp} \end{aligned} \tag{3.31}$$

where θ_{pq} is the angle between the gradient vector of underlying Poisson representation, $\nabla\varphi$ and a vector, v_{pq}, connecting points p, q. These vectors and angles are illustrated in Figure 3.13.

According to intensity, the probabilistic atlas and the boundary term definitions,

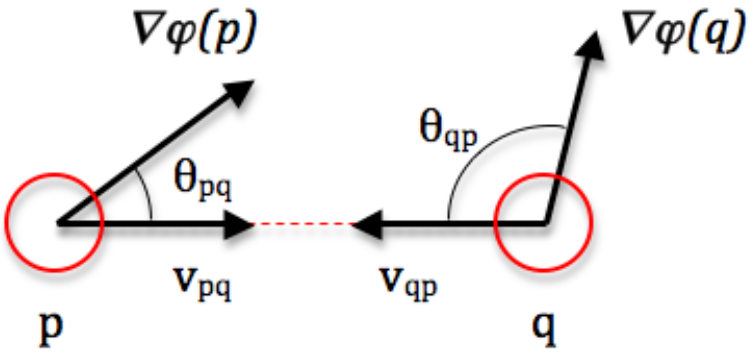

Figure 3.13. Vectors and angles used in boundary term definition.

we have the following overall energy function

$$E(f) = -\zeta_1 \cdot \sum_{p \in \mathcal{P}} \ln P(I_p|f_p) - \zeta_2 \cdot \sum_{p \in \mathcal{P}} \ln \widehat{P}_v(f_p) + \sum_{\{p,q\} \in \mathcal{M}} B_{p,q} \cdot \delta_{f_p \neq f_q} \tag{3.32}$$

where ζ_1 and ζ_2 are introduced parameters that control the relative weighting of corresponding terms. Note that Equation 3.32 is in the form of Equation 2.27. Therefore, we could embed this energy function in a graph $\mathcal{G}$ such that minimum cut of the graph corresponds to global minimum value of the energy function. Moreover, we applied morphological erosion of radius $2 \times 2 \times 2$ to our initial segmentation and utilized the interior region of this binary mask as foreground hard constraints. Edge weights for our formulation is given in Table 3.1.

Table 3.1. Edge weights for graph $\mathcal{G}$ according to our proposal.

Edge	**Weight (cost)**	**For**
$\{p, q\}$	$B_{p,q}$	$\{p, q\} \in \mathcal{M}$
$\{p, S\}$	$-\zeta_1 \cdot \ln P(I_p\|f_p = 0) - \zeta_1 \cdot \widehat{P}_v(f_p = 0)$	$p \in \mathcal{P}, \quad p \notin \mathcal{O} \cup \mathcal{B}$
	∞	$p \in \mathcal{O}$
$\{p, T\}$	$-\zeta_1 \cdot \ln P(I_p\|f_p = 1) - \zeta_1 \cdot \widehat{P}_v(f_p = 1)$	$p \in \mathcal{P}, \quad p \notin \mathcal{O} \cup \mathcal{B}$
	0	$p \in \mathcal{O}$

As we discussed in Section 2.3.1, minimum s/t cut of graph $\mathcal{G}$ could be calculated in polynomial time with max-flow algorithms. Our implementation of the segmentation method uses a new version of max-flow which is proposed in [91].

4. EXPERIMENTS AND RESULTS

In this chapter we explain our evaluation methodology, describe the details of data sets, give our results and compare them against the results of state-of-the-art methods.

4.1. Evaluation Methodology

In order to assess the performance of the segmentation, discrepancies between resulting delineations and reference segmentations must be measured via appropriate metrics. In general, these metrics are based on volumetric overlap and surface distances, that differ from each other in terms of how the overlap and the surface distances are computed. Besides, depending on the problem, some metric categories could be favored over the other. For example, while measuring tumor volumes, measures based on volumetric error are more feasible rather than surface distance measures. Since both the determination of liver volume and the accuracy of the boundaries are major concerns, several measures from both categories have to be used. By this way, each single measure straightens out different aspects of segmentation quality. Volumetric errors could convey information about sensitivity and specifity of segmentation while surface errors could give information about deviation from boundary. Thus, in order to achieve a better estimate of overall segmentation quality multiple measures must be employed [4].

However, it is not clear how to combine multiple measures in order to obtain a total score and rank several segmentation results. Organizers of "3D Segmentation in the clinic: a Grand Challenge" [12] workshop offer a way to solve this problem by transforming the result ϵ_i of each error measure i to a gauged scores $\Theta_i \in [0, 100]$ and

averaging all values to one final score Θ [4]

$$\Theta = \frac{1}{N}\sum_{i=1}^{N}\Theta_i. \tag{4.1}$$

Moreover, calibrated scores Θ_i have to be defined accordingly. To accomplish this goal, a second person who have sufficient training in liver segmentation but not experienced in radiology was asked to segment all images manually. This procedure resulted in average user errors $\bar{\epsilon}_i$ for each measure. The performance of second rater is defined as 75 out of 100 points and calibrated scores for each measure i is calculated by

$$\Theta_i = \max\left(100 - 25\frac{\epsilon_i}{\bar{\epsilon}_i}, 0\right). \tag{4.2}$$

Scores from different measures could be combined as described by 4.1. According to the above definitions, a score of 100 points corresponds to perfect overlap with reference segmentation, whereas a score of 75 is roughly considered as human performance. Therefore, a segmentation algorithm that approximately scores 75 is adequate for clinical purposes. Also one should note that in Equation 4.2, a single segmentation with large errors are truncated to zero to avoid biasing final score critically. In other words, a deviation from reference more than four times as high as the second rater considered as a complete failure [4].

In this thesis, we identically selected 5 measures defined in [4], so as to compare our results with other methods. Below, these measures are described in detail.

(i) *Volumetric Overlap Error:* The volumetric overlap error (VOE) is one of the most popular metrics for evaluating segmentation accuracy. Between two sets of voxels $\mathcal{P}_A$ and $\mathcal{P}_B$, it is defined as:

$$VOE = 100 \times \left(1 - \left(\frac{|\mathcal{P}_A \cap \mathcal{P}_B|}{|\mathcal{P}_A \cup \mathcal{P}_B|}\right)\right). \tag{4.3}$$

The VOE is zero for perfect segmentation and 100 for segmentation and reference

does not overlap.

(ii) *Relative Volume Difference:* The relative volume difference (RVD) is defined between two set of voxels $\mathcal{P}_A$ and $\mathcal{P}_B$ which correspond to segmentation and reference respectively as

$$RVD = 100 \times \left(\frac{|\mathcal{P}_A| - |\mathcal{P}_B|}{|\mathcal{P}_B|} \right). \tag{4.4}$$

Because of the reason that this measure is not symmetric, it is not a metric. The RVD is zero if both volumes have same number of voxels. It is crucial to point out that this does not indicate that volumes are identical or actually overlap with each other. Therefore, it is important not to employ RVD to evaluate segmentation solely by itself. In combination with other measures, RVD shows whether a method tends to over- or under-segment. For this reason, results obtained by RVD are signed numbers but to compute corresponding score, the absolute value is used.

(iii) *Average Symmetric Surface Distance:* The average symmetric surface distance (ASD) is one of the broadly used measures. It is calculated from surface voxels of two segmentations $\mathcal{P}_A$ and $\mathcal{P}_B$ and is given in millimeters. If a voxel has at least one non-object voxel in its 18-neighborhood, then the voxel is labeled as a surface voxel. For each surface voxel in $\mathcal{P}_A$, the Euclidean distance to the closest surface voxel in $\mathcal{P}_B$ is calculated. In order to provide symmetry, distances from $\mathcal{P}_B$ to $\mathcal{P}_A$ is also calculated. Then, ASD is defined as the average of all calculated distances. For a perfect overlap, this measure is zero. Specifically, let $S(\mathcal{P}_A)$ denote the set of surface voxels of $\mathcal{P}_A$. The shortest distance of an arbitrary voxel v to $S(\mathcal{P}_A)$ is defined as

$$d(v, S(A)) = \min_{s_{\mathcal{P}_A} \in S(\mathcal{P}_A)} \|v - s_{\mathcal{P}_A}\| \tag{4.5}$$

where $\|.\|$ denotes the Euclidean distance. The ASD is then given by

$$ASD(\mathcal{P}_A, \mathcal{P}_B) = \frac{1}{|S(\mathcal{P}_A)| + |S(\mathcal{P}_B)|} \left(\sum_{s_{\mathcal{P}_A} \in S(\mathcal{P}_A)} d(s_{\mathcal{P}_A}, S(\mathcal{P}_B)) + \sum_{s_{\mathcal{P}_B} \in S(\mathcal{P}_B)} d(s_{\mathcal{P}_B}, S(\mathcal{P}_A)) \right). \quad (4.6)$$

(iv) *Root Mean Square Symmetric Surface Distance:* The root mean square symmetric surface distance (RMSD) is a similar metric to ASD. It is also based on surface distances and given in millimeters. Instead of calculating Euclidean distances directly as in the calculation of ASM, the root of averaged squared distances are computed. To be more clear, RMSD is defined as:

$$RMSD(\mathcal{P}_A, \mathcal{P}_B) = \sqrt{\frac{1}{|S(\mathcal{P}_A)| + |S(\mathcal{P}_B)|}} \times \sqrt{\sum_{s_{\mathcal{P}_A} \in S(\mathcal{P}_A)} d^2(s_{\mathcal{P}_A}, S(\mathcal{P}_B)) + \sum_{s_{\mathcal{P}_B} \in S(\mathcal{P}_B)} d^2(s_{\mathcal{P}_B}, S(\mathcal{P}_A))}. \quad (4.7)$$

For a perfect segmentation, RMSD becomes zero. Since RMSD punishes large deviations from true contour stronger than ASD, it naturally complements ASD.

(v) *Maximum Symmetric Surface Distance:* The maximum symmetric surface distance (MSD) given in millimeters and computed in a similar manner to previous surface distance based metrics. For each surface voxel in $\mathcal{P}_A$, the Euclidean distance to the closest surface voxel in $\mathcal{P}_B$ is calculated and vice versa. Then, maximum value among them yields MSD and defined as follows

$$MSD(A, B) = \left\{ \max_{s_{\mathcal{P}_A} \in S(\mathcal{P}_A)} d(s_{\mathcal{P}_A}, S(\mathcal{P}_B)), \max_{s_{\mathcal{P}_B} \in S(\mathcal{P}_B)} d(s_{\mathcal{P}_B}, S(\mathcal{P}_A)) \right\}. \quad (4.8)$$

For a perfect segmentation, MSD is zero. In the applications in which the worst case error is more important than average errors, this measure detects outliers and obtains true maximum error.

4.2. Image Data Sets

We evaluated our approach using two different public data sets. The data sets we used are two (M1 and M2) data sets of liver segmentation competition of "3D Segmentation in the clinic: a Grand Challenge" [12] workshop which is held at the Medical Image Computing and Computer-Assisted Intervention (MICCAI) 2007 Conference in Brisbane, Australia. For the workshop, organizers provided a total of 30 3D images. 20 of them (M1 data set) are used to train and test algorithms and they are available with their corresponding reference expert segmentations. The remaining 10 of them (M2 data set) do not have reference segmentations and are used as the test set in the competition. All data are available online through competition website.[1]

MICCAI data set is collected from different clinics, therefore CT images are scanned via various machines with 4, 16 and 64 detector rows of different manufacturers. All of 30 images are enhanced with contrast agent and acquired in the central venous phase. Machine and protocol used varied pixel spacing from 0.55 to 0.8 mm in x/y direction and inter-slice distance between 1 and 3 mm. Also for one of the protocols, patients need to lie on their side, thus entire anatomy is rotated around $z-$axis. Most of the images are pathologic and include tumors, metastasis and cysts in different sizes.

To obtain the reference segmentations, expert radiologists manually delineated liver parenchyma working slice-by-slice in transversal view. In this process, radiologists used intensity based seeded region grower to generate initial segmentation. Further, leakage and inaccurate boundaries are refined by drawing manual cut lines by employing freehand tools. The whole liver tissue including all internal structures such as vessels and tumors are included in the liver mask during manual segmentations. A vessel is considered as a part of liver, if it is completely surrounded by liver tissue. If a vessel is partially enclosed by liver (often the case where large veins - vena cava and portal vein enter or leave the liver), only the parts surrounded by liver

[1] http://sliver07.isi.uu.nl/index.php, accessed at August 2011.

tissue are included in segmentation, i.e. the convex hull of the liver shape in that area is added to liver mask. In order to avoid inconsistency between transversal slices, a binary median filter of $3 \times 3 \times 3$ size is performed as a post-procesing step. To reduce inconsistency a bit more, a single expert examined the results and corrected them if necessary.

4.3. Results

To segment the CT images in M1 and M2 data sets, we manually selected bounding boxes. Moreover, the initialization of EM algorithm is achieved based on the histogram observations given in Section 3.1. We have chosen initial mean values as

$$\begin{aligned} \mu_{gallbladder} &= lower_bound; \\ \mu_{soft_tissue} &= \mu_{liver} - ((\mu_{liver} - \mu_{gallbladder}) \times 0.5), \\ \mu_{liver} &= liver_peak, \\ \mu_{vessel} &= \mu_{liver} + ((upper_bound - \mu_{liver}) \times 0.33), \\ \mu_{bone} &= \mu_{liver} + ((upper_bound - \mu_{liver}) \times 0.66), \end{aligned} \tag{4.9}$$

initial variances as

$$\sigma_i^2 = 625 \qquad \forall i, \tag{4.10}$$

and initial component weights as

$$\begin{aligned} \pi_{gallbladder} &= 0.2, \\ \pi_{soft_tissue} &= 0.3, \\ \pi_{liver} &= 0.4, \\ \pi_{vessel} &= 0.05, \\ \pi_{bone} &= 0.05. \end{aligned} \tag{4.11}$$

The initialization values for variances and proportions are determined empirically. For calculation of edge estimates during adaptive thresholding we have used the edge map function given in Equation 3.2 with $\eta = 1$, $\alpha = 1$, $\lambda = 4$. For probabilistic atlas probabilities, we set $\tau_{vote_low} = 0.05$ and $\tau_{vote_high} = 1$. Therefore, only the regions where all the registrations of reference segmentations agree could constrain our segmentation. To estimate boundary probabilities, we have sampled intensity profiles of length 7 with 1 mm spacing. Additional false profiles are sampled with an offset of ± 1 mm and ± 3 mm. For calculating probabilities, we empirically decided to use $k = 20$ nearest neighbors. Besides, the relative weights for intensity term and probabilistic atlas term is experimentally determined and selected as $\zeta_1 = 0.05$ and $\zeta_2 = 0.01$.

During the evaluation on M1 data set, we have employed leave-one-out cross-validation. Therefore, we have chosen an image from the data set as test subject and the rest is used for training. The scores obtained on M1 data set are summarized in Table 4.1. According to the results in Table 4.1, there is no image that our algorithm completely fails. Also, our method is able to segment liver structure with an average surface distance of 1.05 which is highly accurate for clinical purposes. However, slightly high VOE indicates a possible over- or under-segmentation. It is also worth noticing that we have scored a relatively low MSD with low variance across different patients. This could possibly reveal that we have not missed any prominent tumor in the data set. Visual results for the worst case (case 1) and a tumorous case (case 16) is given in Figure 4.1. The visual results for whole M1 data set is given in Appendix A.

In addition to that, we also present scores of top ranking methods that participate in liver segmentation competition of "3D Segmentation in the clinic: a Grand Challenge" [4] workshop in Table 4.2. Please note that these results were achieved in M2 data set, whose reference segmentations are not available. The highlighted team, Lara, corresponds to second rater which is mentioned in Section 4.1. Although the results in Table 4.2 are obtained in M2 data set, it is still gives a rough comparison,

Table 4.1. Segmentation evaluation scores on M1 data set.

Case	**VOE**	**RVD**	**ASD**	**RMSD**	**MSD**	**Total**
1	8.56	-1.16	1.84	3.73	33.45	63.78
2	4.83	-1.30	1.01	1.78	17.59	80.24
3	4.93	-1.01	1.04	2.28	26.88	76.51
4	6.21	-2.41	0.97	2.41	23.87	74.78
5	5.24	-0.94	0.96	2.41	24.47	77.00
6	5.66	2.00	0.99	2.23	25.67	75.60
7	4.85	-1.31	0.77	1.36	19.19	82.14
8	6.92	1.33	1.44	2.86	29.28	70.38
9	6.61	2.68	1.09	2.76	26.47	71.93
10	5.91	1.79	1.00	1.85	17.82	78.70
11	5.38	0.82	1.07	2.81	25.42	75.15
12	5.45	2.02	0.99	2.31	24.87	75.74
13	7.84	2.49	1.43	2.37	18.13	72.76
14	4.17	-1.38	0.86	1.65	15.22	82.40
15	4.00	-1.38	0.67	1.58	19.86	82.49
16	4.60	-1.57	1.10	2.25	26.90	75.94
17	5.44	0.50	0.98	2.14	19.62	79.25
18	4.43	-1.77	0.72	1.28	13.06	84.05
19	5.02	-2.17	0.98	2.66	29.79	73.71
20	4.75	-2.62	1.04	2.25	22.99	76.04
All	5.54	1.6	1.05	2.25	23.03	**76.43**

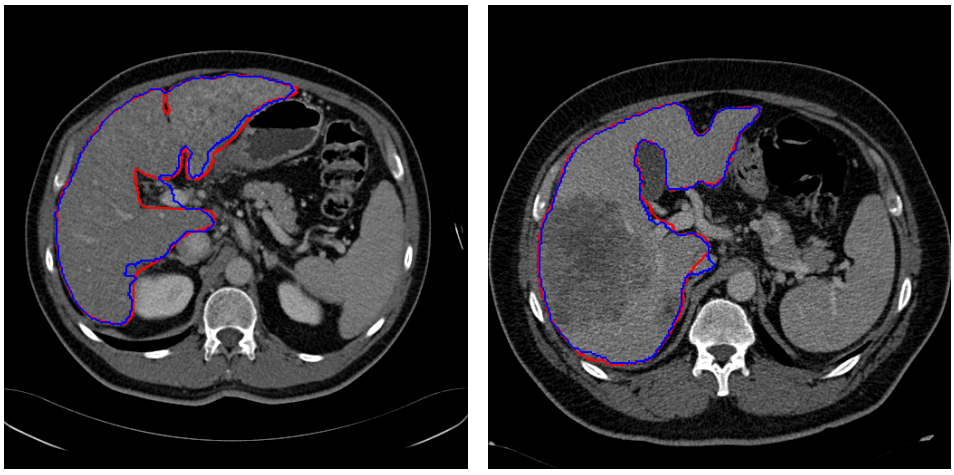

(a) (b)

Figure 4.1. Segmentation results for (a) case 1 and (b) case 16. Reference segmentation outline is given in red and segmentation results of our method is given in blue.

Table 4.2. Top ranking methods participated in liver segmentation competition of "3D Segmentation in the clinic: a Grand Challenge" [12] workshop. These results are achieved in M2 data set.

Position	**Team**	**System**	**Score**
1	LME Erlangen	Semi-automatic	84.55
2	LiverPlanner [52]	Interactive	82.09
3	Eccet [22]	Interactive	77.92
4	ZIB-Charite [27]	Automatic	77.35
5	LME Erlangen [47]	Automatic	76.78
6	LiverV [92]	Semi-automatic	76.42
7	amcmil [19]	Semi-automatic	75.45
	Lara	**Interactive**	**75.14**
8	LME Erlangen [11]	Automatic	74.02
9	VMGPU	Interactive	72.88
10	vislib [48]	Semi-automatic	70.05

since data sets are originated form the same source. Since reference segmentation are not available for M2 data set, we did not provide numerical performance evaluation of our method for this data set. However, we have presented visual segmentation results in Appendix B in comparison with other automatic or semi-automatic segmentation methods.

5. DISCUSSION

The scores obtained on M1 data set show that our method could segment the liver structure with high accuracy. Since a score of 75 roughly coincides with human performance, we could claim that our method is clinically acceptable. With regard to results presented in Table 4.2, our method ranks in top ten over entire methods. Also, our methods is in top five if semi-automatic and automatic methods are considered alone. However, it is crucial to note that these are only approximate rankings, since we did not evaluate our method with the same data set unlike the methods in the table. Although the scores are obtained on a different data set, they still allow a rough comparison since data sets come from same source. Furthermore, it is also necessary to point out that there are only a few fully automatic methods that achieved a high ranking. Although our system is a semi-automatic method with current implementation, it requires minimal user interaction only at the beginning during the selection of the bounding box. Therefore, our method could be easily converted to automatic method by just utilizing anatomical prior knowledge. One possible way to automatize bounding box selection is determining lung and air regions by simple thresholding, since HU values of air is below than the HU values of any other structure of interest. Then, one could constrain segmentation region in x/y direction with the boundary to the air region. Furthermore, we could constrain in z direction, since lungs are adjacent to liver from above and liver has a priori size in millimeters.

In reference to the scores of our algorithm, one could argue about the under-segmentation tendency of our method due to low sensitivity values. This problem could be stemmed from probabilistic atlas, since it tends to become undersized due to its construction. An example of this situation is shown in Figure 5.1. In this figure, a constructed PA is given with manual segmentation and it is observed that PA lies mostly in manual segmentation. Actually, initial segmentation results could not propagate to boundaries because of spatially varying adaptivity defined in terms of gradients. In parallel with this under-segmentation during initialization, we obtain

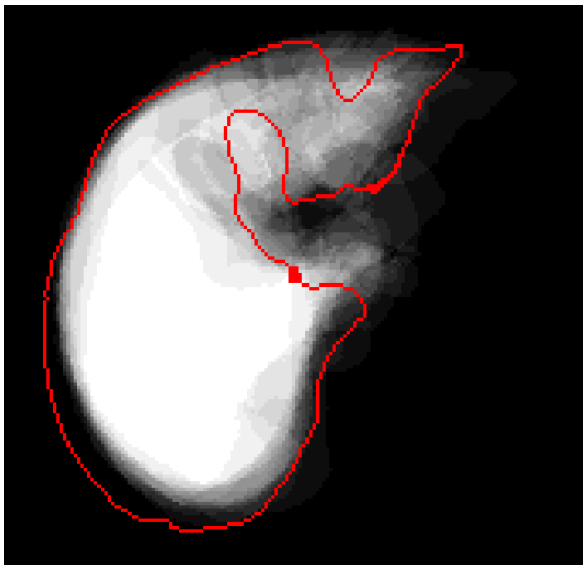

Figure 5.1. Undersized PA. The outline of the manual segmentation is given by red contour.

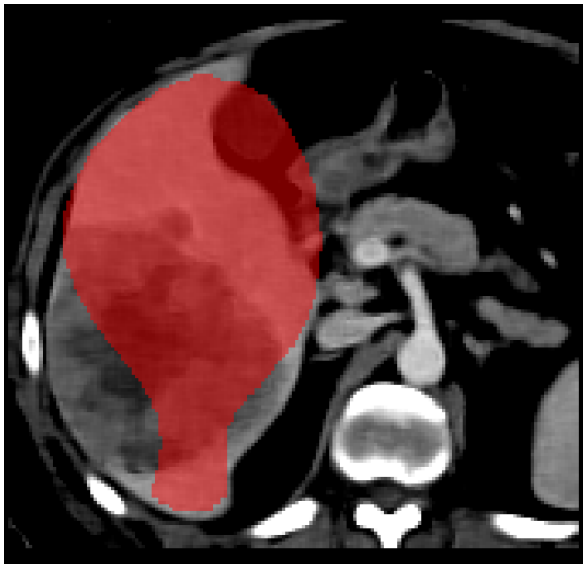

Figure 5.2. Convex hull computation failure.

undersized convex hulls and as a result this is transfered to probabilistic atlas. In addition to that, convex hull computation fails for cases which includes large tumors. An example is given in Figure 5.2. This is caused by the numerical implementation of min flow. For such cases, PA could grow to the intended size if a better convex hull is available. Therefore, a different convex hull algorithm or a different numerical implementation of current algorithm will be a better choice for our proposal.

Another problem originated from PA is the under-segmentation of high curvature regions of the left lobe. An example result is given in Figure 5.3. In those regions, PA is unable to model the structure because of the high variation of the left lobe and global optimum solution cuts these regions form segmentation. Increasing the relative weight of the intensity term can be a solution. However, this effects segmentation problem globally and can lead to exclusion of tumors. Therefore, interchanging the roles of the intensity term and PA term locally can provide a solution.

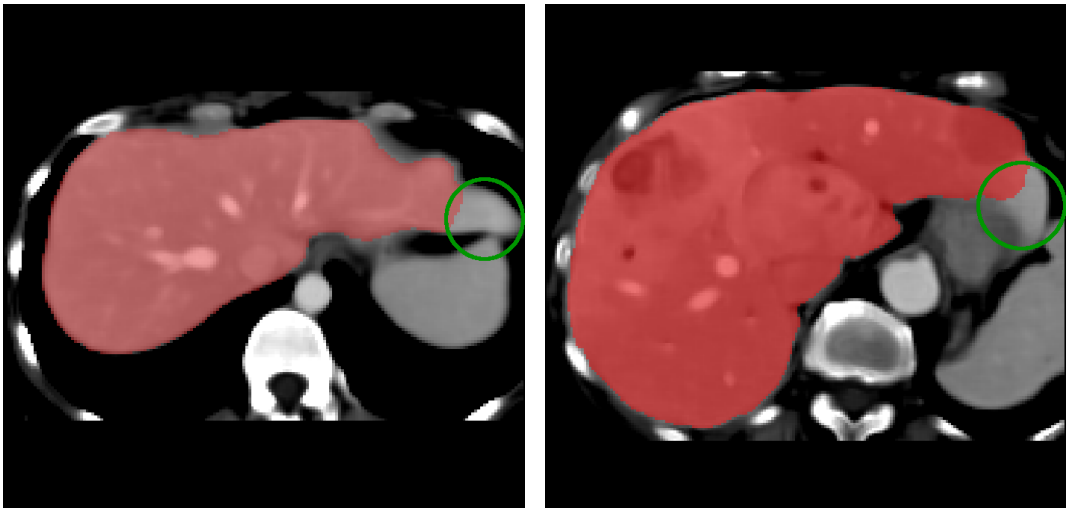

(a) (b)

Figure 5.3. Segmentation failure in left lobe of the liver. The green circle marks the missed part in the left lobe of the liver.

Our proposal is proven to handle tumorous cases and able to include pathologies even if they are close to the liver surface. However, there are exceptions. An example of such exception is shown in Figure 5.4. Considering our formulation, tumors get a

high weight form PA term and a low weight from intensity term. Most of the times, in tumorous regions, these terms seem to cancel each other and leave the decision to the boundary term. However, for some tumors, both intensity and vote terms assign a low weight to the region. Therefore, the graph is divided from the interior boundary between liver and tumor. One direct solution to the problem is increasing one of the weights. In our current proposal, only intensity distributions of liver and vessel are considered to form the intensity term. Besides, the regions between the initial segmentation and final segmentation can reveal the intensity distribution of tumor voxels if there is another tumor inside the liver apart from non-segmented one. Afterwards, the intensity distribution of tumors can be included in intensity term as well and one could re-run graph cut algorithm with updated probabilities.

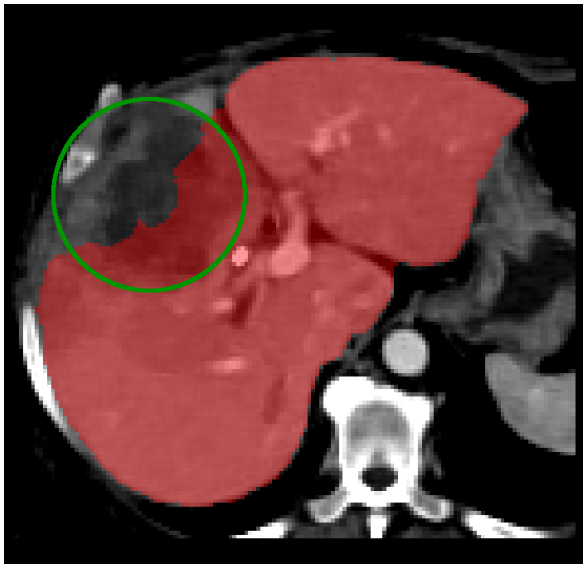

Figure 5.4. Part of the tumor inside green contour is missed.

Boundary term defined by kNN appearance models have obtained superior results compared to intensity difference based counterparts. Also, we have shown that a slight modification of kNN appearance model yielded better results. Utilizing the solution of Poisson equation instead of signed distance transform to define profile orientations improved the results in describing the boundaries of large tumors. The probability assignment results of kNN appearance model using both signed distance

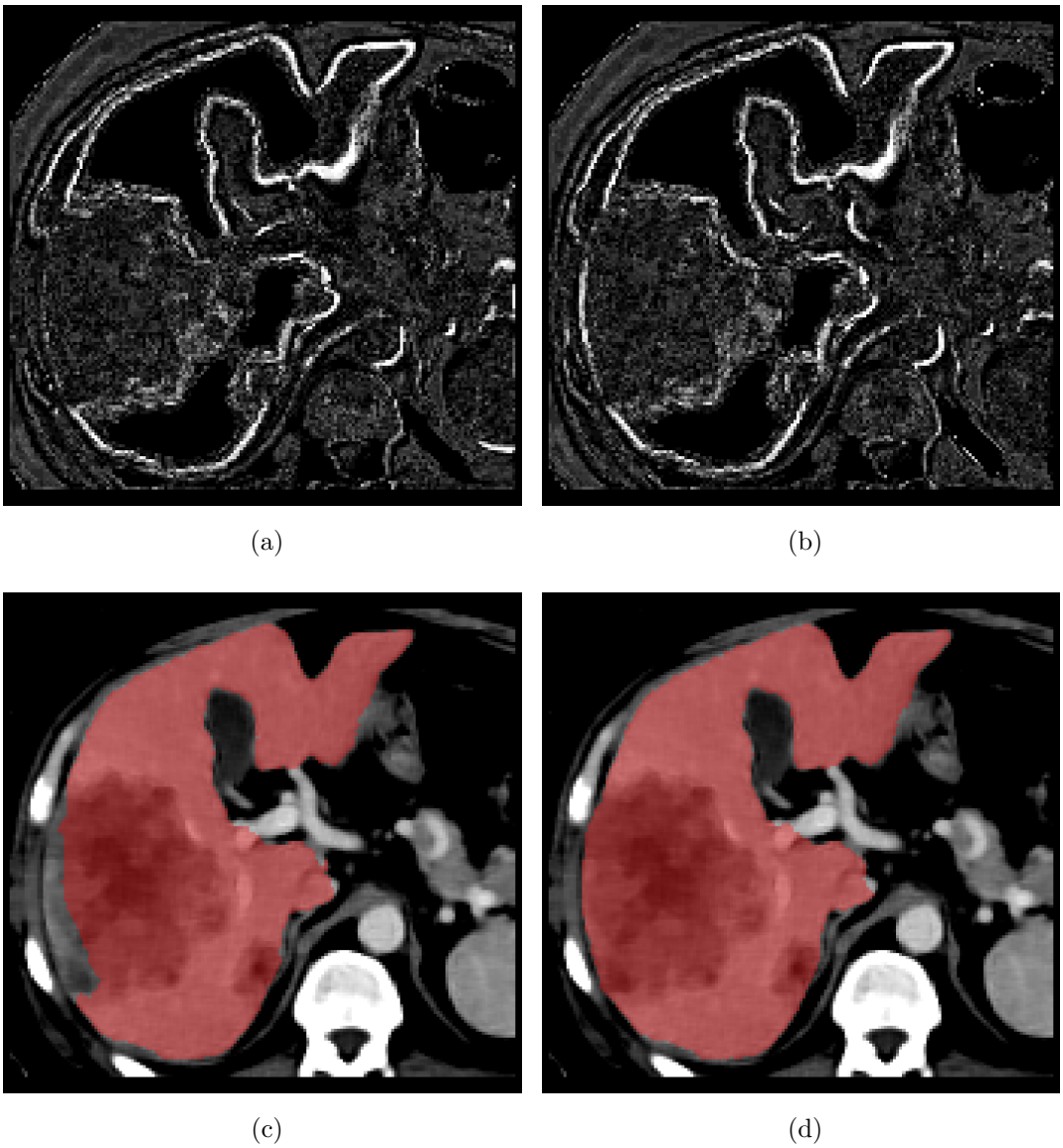

(a) (b)

(c) (d)

Figure 5.5. Boundary probability assignments using (a) SDF and (b) Poisson equation. Segmentation results employing results of (a) and (b) is given in (c) and (d) respectively.

function and Poisson equation solution is given in Figure 5.5. Corresponding segmentation results with same parameters are also presented in Figure 5.5. These results show that our proposal outperforms the existent procedure. In addition to that, edge enhancing diffusion is also responsible for acquiring improved results. By applying edge enhancing diffusion before sampling both training and query profiles, we are able to obtain clean boundary responses instead of noisy ones. An comparison of $P_v(p)$ maps estimated from noisy and smoothed profiles are given in Figure 5.6. As seen from Figure 5.6, edge enhancing diffusion clearly improved the results by locating boundaries more precisely.

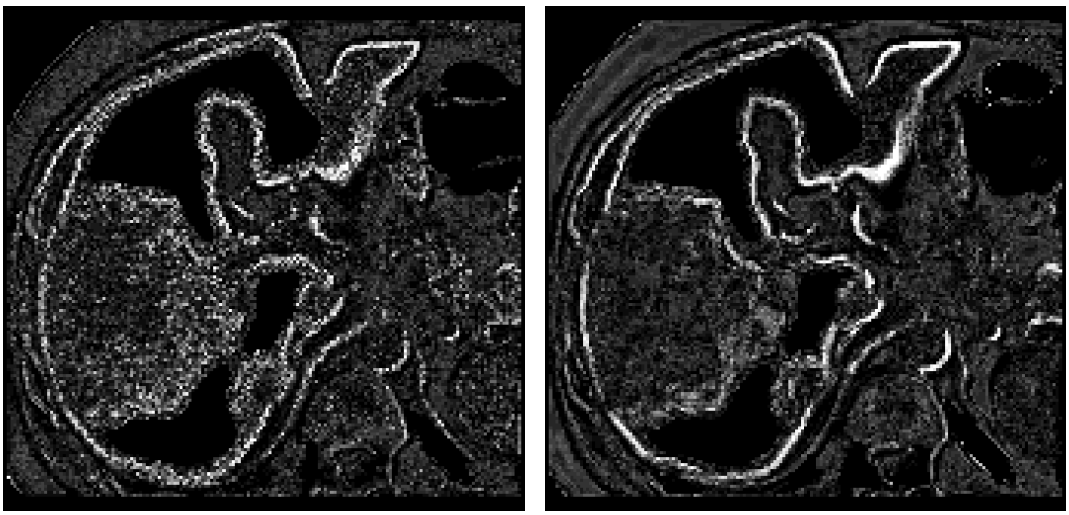

(a) (b)

Figure 5.6. Boundary probability assignments using (a) noisy and (b) smoothed profiles.

6. CONCLUSION

In this thesis, we have proposed a semi-automatic liver segmentation method in 3D CT data. The aim of this algorithm is to provide an accurate and robust liver segmentation for surgery planning of interventions and treatment planning for liver diseases. Liver is a challenging organ to segment because of the variation of both neighboring structures and structures within liver. In order to cope with these challenges, we tried to model the prior information about the liver such as intensity distributions, location and shape. For this purpose, we have proposed a combination of intensity distribution modeling, probabilistic atlases and graph cuts. Moreover, we have developed a novel way to construct PA based on the convex hulls of initial and reference segmentations and have discussed the ways of integrating PA to graph cut framework. Furthermore, we have also discussed the ways of incorporating gray level appearance models into graph cut formulation and proposed a slight modification of kNN appearance models with the help of Poisson equation.

In the evaluation, we have tested our segmentation algorithm on real CT scan of abdomen. For this purpose, we utilized two data sets of liver segmentation competition of "3D Segmentation in the clinic: a Grand Challenge" [12] workshop which is held at the Medical Image Computing and Computer-Assisted Intervention (MICCAI) 2007. These publicly available data sets are consisted of several healthy and pathological liver CTs that are scanned via various protocols and machines. Utilizing these data sets give us a chance to compare our algorithm against state-of-the-art liver segmentation methods in the literature.

Results of proposed algorithm show that our method is capable of segmenting the liver with high accuracy and could be practiced in the clinic. In most of the pathological cases, the proposed solution was able to include tumors inside segmentation. In addition to that, our method has proven to be robust for large tumors and tumors that are neighboring to surface of the liver due to inclusion of PA. An exception oc-

curs where both intensity and PA term are not able to identify the region as tumor. In such cases, segmentation follows either the inner surface between liver and tumor or arbitrary surface inside tumor and thus excludes tumor. On the other hand, our method has failed to segment high curvature regions of the left lobe. This problem is due to inability of PA to model these highly varying parts. Both of these problems indicate the necessity of personalized shape and intensity modeling. Although the intensity modeling in our method is personalized for each patient due to estimation of probabilities directly from the data for that patient, there is still room for improvement and this could be a subject for future work. For example intensity distributions of tumors can be estimated by the voxels that lie under difference of initial segmentation and final segmentation masks and this estimation can be used to update intensity term in graph cut segmentation. One of the potential solutions for shape modeling is to select an optimal subset of manual delineations before or after registration. By doing so, PAs are constructed employing only a subset of manual segmentations that are known to be somewhat similar to our test subject. A different solution is to define a local selection strategy based on a local similarity measure for registered reference segmentations. As a future work, both solution alternatives could be studied in detail. Another problem encountered is the tendency for creating under-segmented results. This problem is inherited from the construction of PA which is generally undersized. To solve this problem, one could ponder about a way to construct PAs such that the ramp of the probabilities correspond to vicinity of boundary as a future work.

APPENDIX A: RESULTS ON M1 DATA SET

In this appendix, we have presented segmentation results of our method on M1 data set. In Figure A.1, outlines of manual delineations and our segmentation results are depicted with red and blue contours respectively.

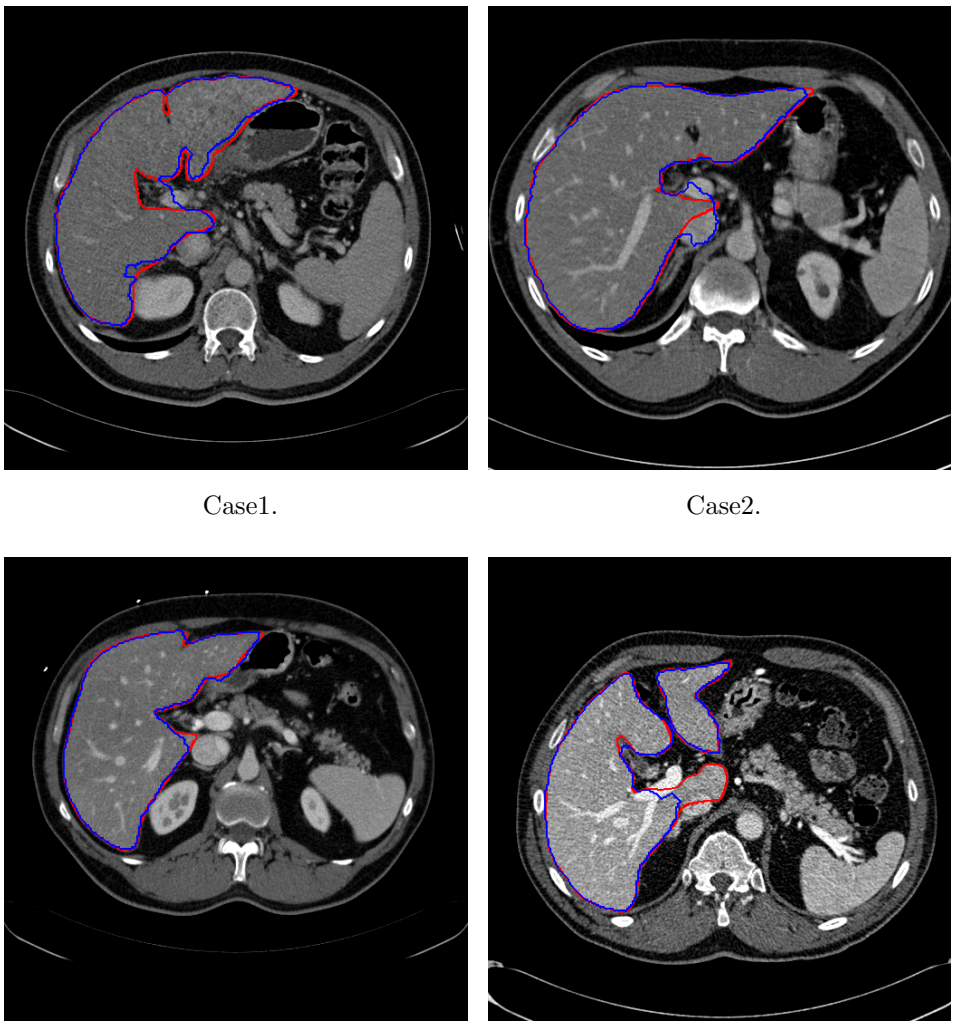

Case1. Case2.

Case3. Case4.

Figure A.1. Results on M1 data set.

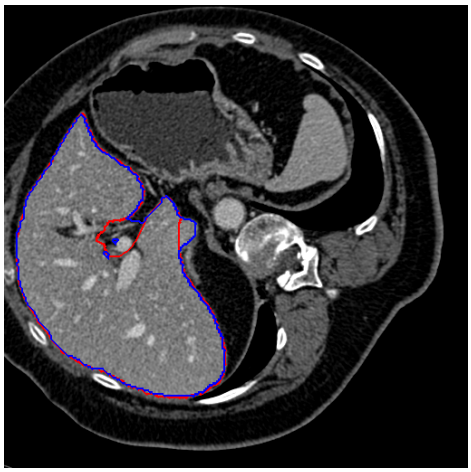

Case5.

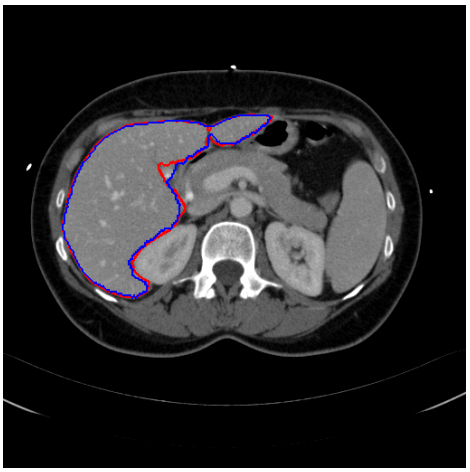

Case6.

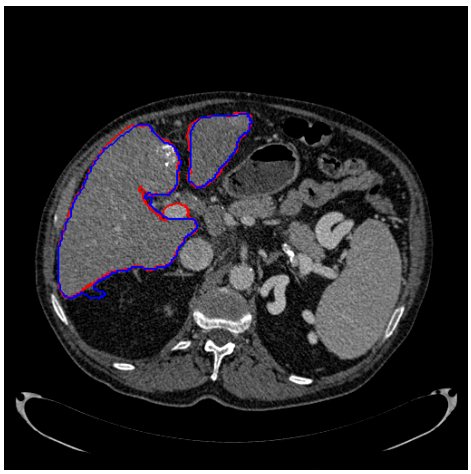

Case7.

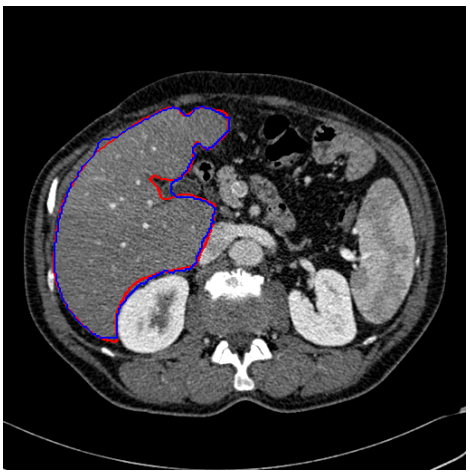

Case8.

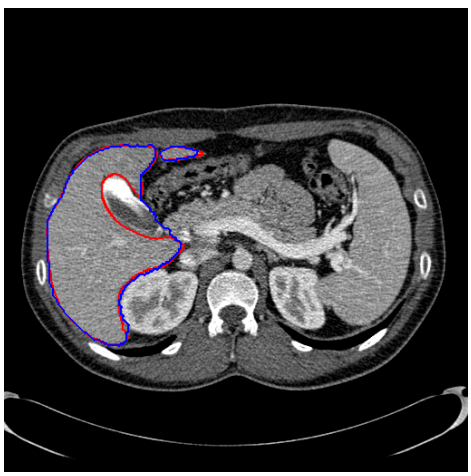

Case9.



Case10.

Figure A.1. Results on M1 data set cont.



Case11.

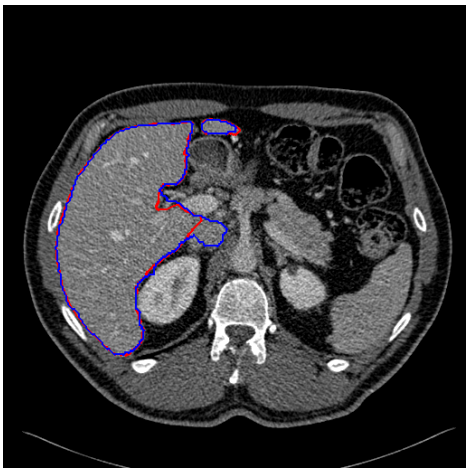

Case12.

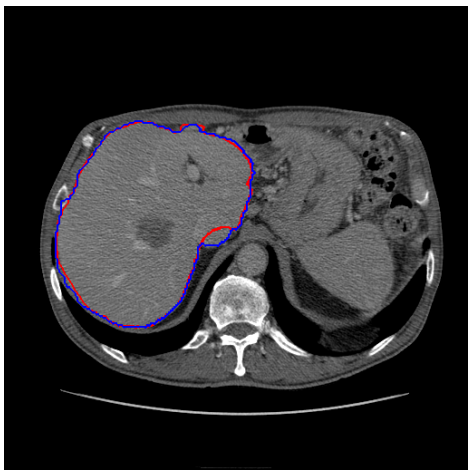

Case13.

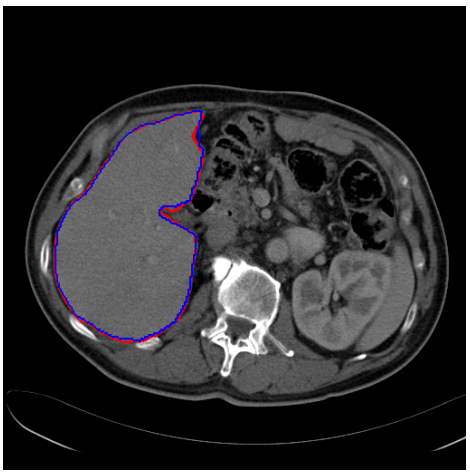

Case14.

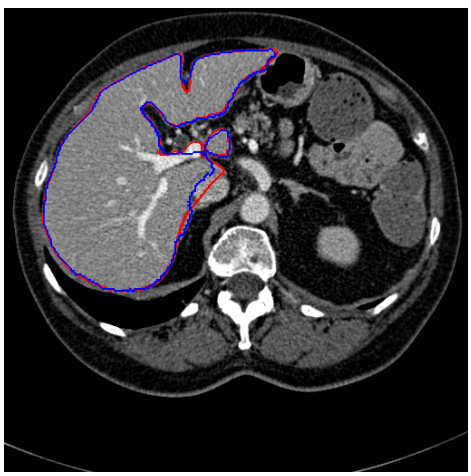

Case15.

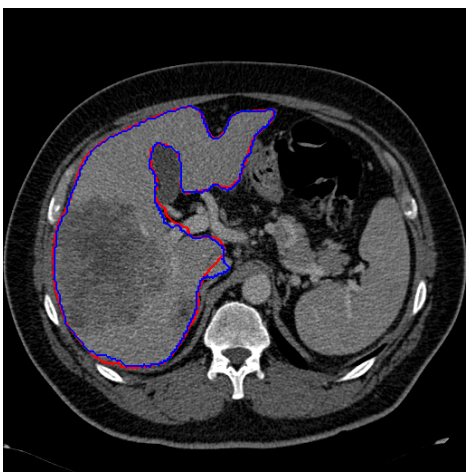

Case16.

Figure A.1. Results on M1 data set cont.

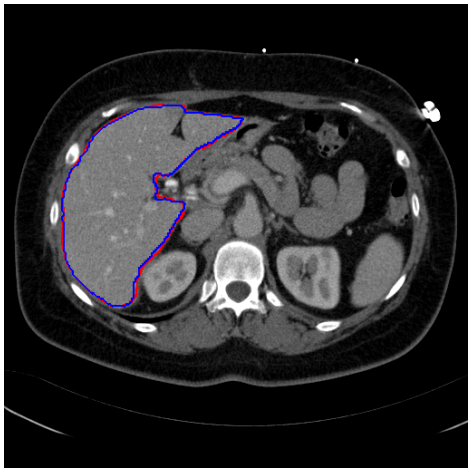

Case17.

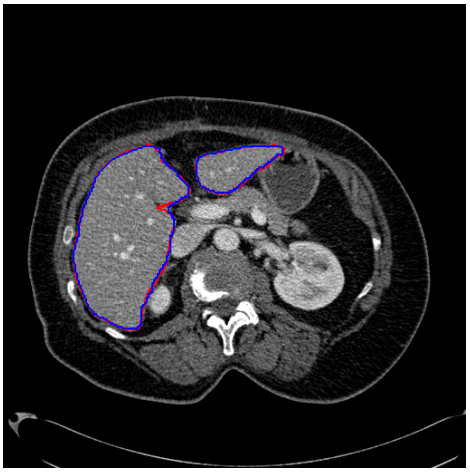

Case18.

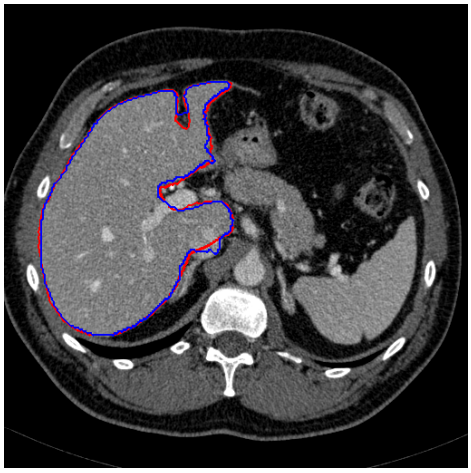

Case19.

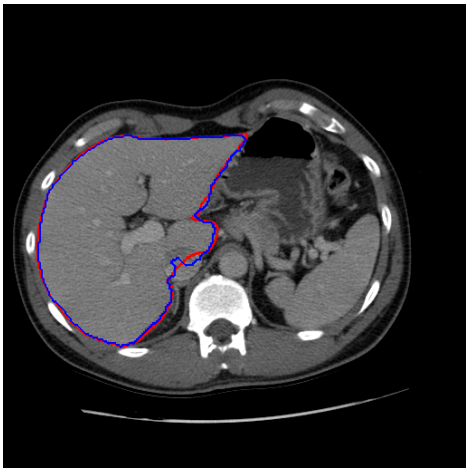

Case20.

Figure A.1. Results on M1 data set cont.

APPENDIX B: RESULTS ON M2 DATA SET

In this appendix, we have presented segmentation results of our method for three cases of M2 data set. Furthermore, to provide a comparison of our method with other methods, the results of five top ranking automatic or semi-automatic methods are also given. Both manual delineations and results of other methods are obtained from competition website.[2] In Figure B.1, B.2 and B.3, outlines of manual delineations are given by red contours while the results are denoted with blue contours.

[2]http://sliver07.isi.uu.nl/index.php, accessed at August 2011.

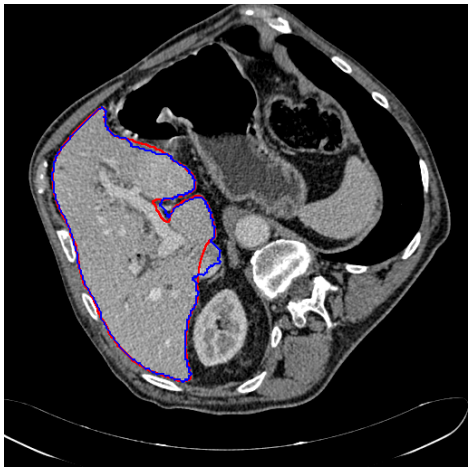

Our result.

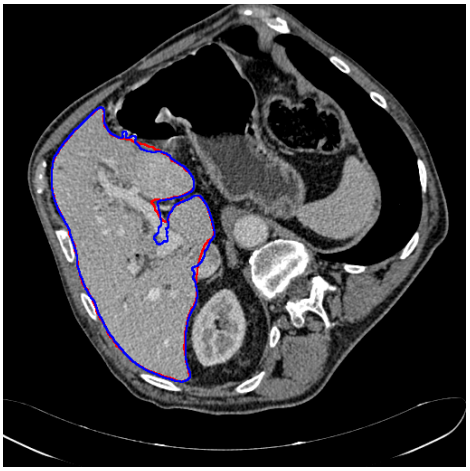

Result of modified version of [46].

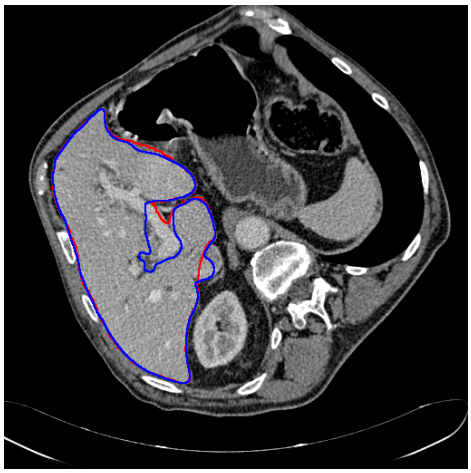

Result of [27].



Result of [47].

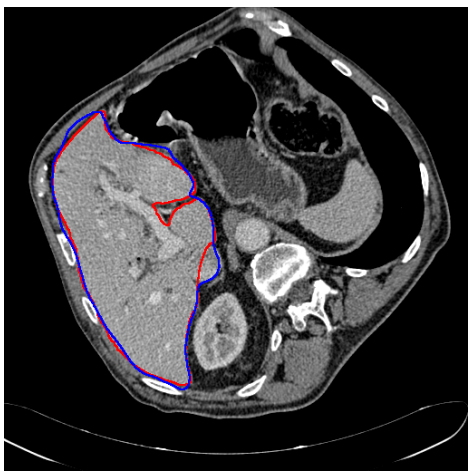

Result of [92].

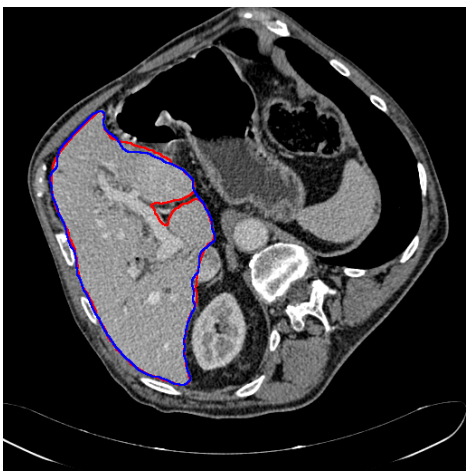

Result of [19].

Figure B.1. The results of our method and five top ranking automatic or semi-automatic methods on case 1 of M2 data set.

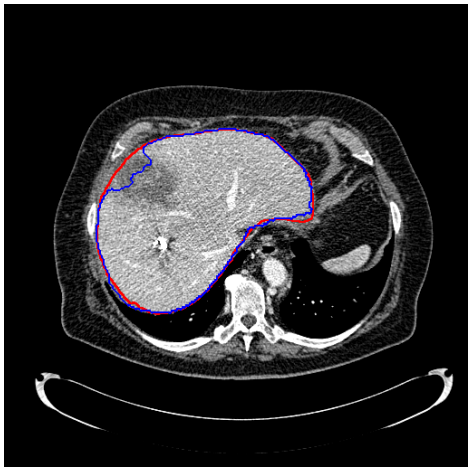

Our Result.

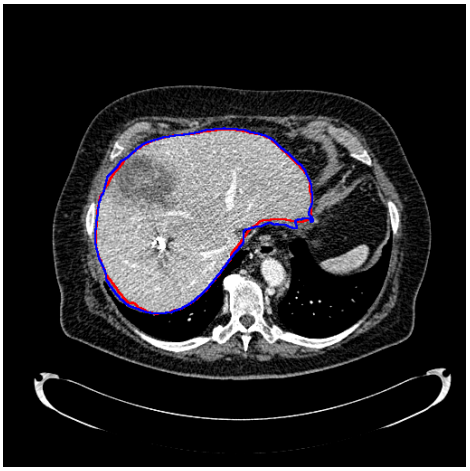

Result of modified version of [46].

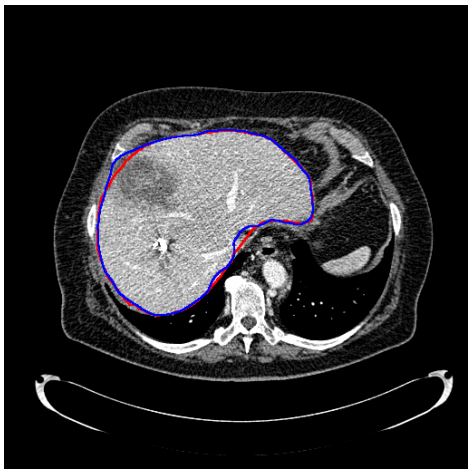

Result of [27].

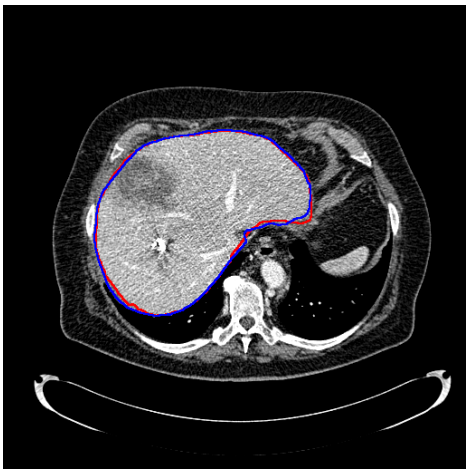

Result of [47].

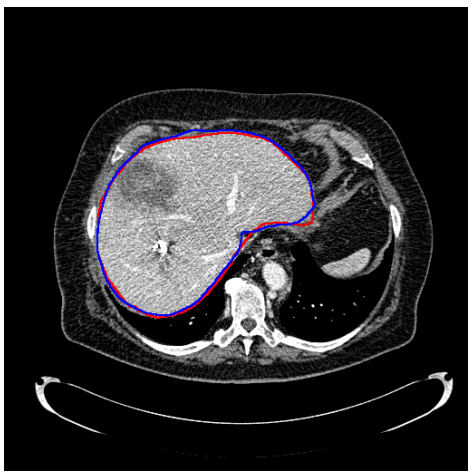

Result of [92].

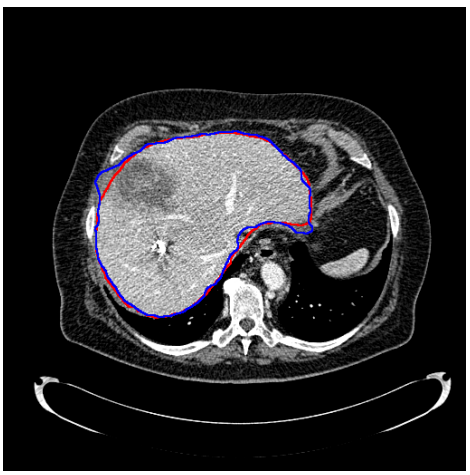

Result of [19].

Figure B.2. The results of our method and five top ranking automatic or semi-automatic methods on case 3 of M2 data set.

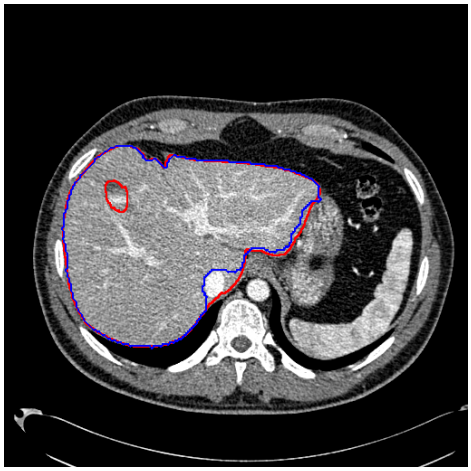

Our result.

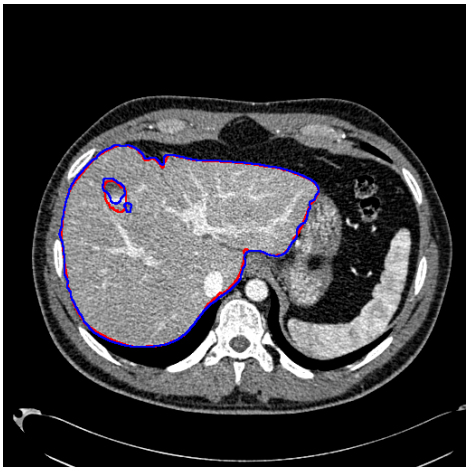

Result of modified version of [46].

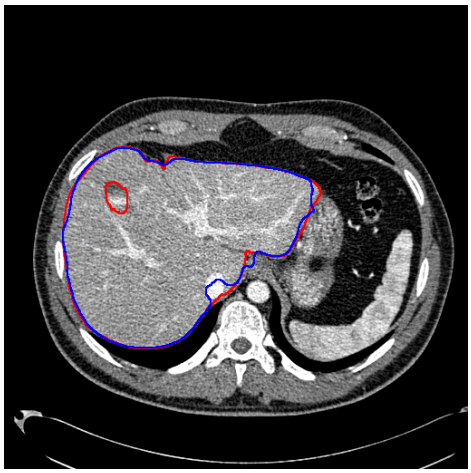

Result of [27].

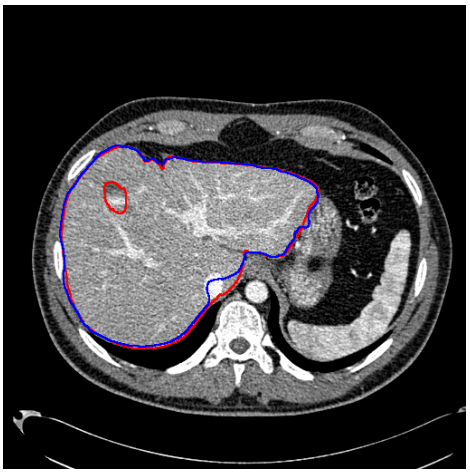

Result of [47].

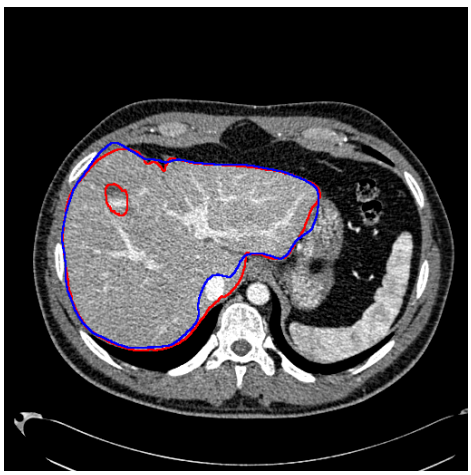

Result of [92].

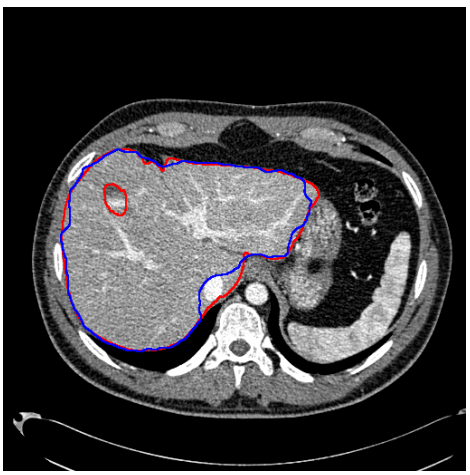

Result of [19].

Figure B.3. The results of our method and five top ranking automatic or semi-automatic methods on case 6 of M2 data set.

REFERENCES

1. World Health Organization (WHO), *Cancer Fact Sheet*, `http://www.who.int/mediacentre/factsheets/fs297/en`, accessed at August 2011.

2. Ruskó, L., H. P. Meinzer and I. Wolf, "Fully automatic liver segmentation for contrast-enhanced CT images", M. Styner, B. v. Ginneken and T. Heimann (Editors), *Proceedings of Medical Image Computing and Computer-Assisted Intervention Workshop 3D Segmentation in the Clinic: A Grand Challenge*, Brisbane, Australia, 2007, pp. 143–150, 2007.

3. van Rikxoort, E., Y. Arzhaeva and B. van Ginneken, "Automatic segmentation of the liver in computed tomography scans with voxel classification and atlas matching", M. Styner, B. v. Ginneken and T. Heimann (Editors), *Proceedings of Medical Image Computing and Computer-Assisted Intervention Workshop 3D Segmentation in the Clinic: A Grand Challenge*, Brisbane, Australia, 2007, pp. 101–108, 2007.

4. Heimann, T., B. van Ginneken, M. Styner, Y. Arzhaeva, V. Aurich, C. Bauer, A. Beck, C. Becker, R. Beichel, G. Bekes, F. Bello, G. Binnig, H. Bischof, A. Bornik, P. Cashman, Y. Chi, A. Cordova, B. Dawant, M. Fidrich, J. Furst, D. Furukawa, L. Grenacher, J. Hornegger, D. Kainmuller, R. Kitney, H. Kobatake, H. Lamecker, T. Lange, J. Lee, B. Lennon, R. Li, S. Li, H.-P. Meinzer, G. Nemeth, D. Raicu, A.-M. Rau, E. van Rikxoort, M. Rousson, L. Rusko, K. Saddi, G. Schmidt, D. Seghers, A. Shimizu, P. Slagmolen, E. Sorantin, G. Soza, R. Susomboon, J. Waite, A. Wimmer and I. Wolf, "Comparison and Evaluation of Methods for Liver Segmentation From CT Datasets", *IEEE Transactions on Medical Imaging*, Vol. 28, No. 8, pp. 1251–1265, 2009.

5. Gray, H., *Anatomy of the Human Body*, Lea and Febiger, Philadelphia, 1918, `www.bartleby.com/107/`, accessed at August 2011.

6. Park, H., P. Bland and C. Meyer, "Construction of an abdominal probabilistic atlas and its application in segmentation", *IEEE Transactions on Medical Imaging*, Vol. 22, No. 4, pp. 483–492, 2003.

7. Zhou, X., T. Kitagawa, T. Hara, H. Fujita, X. Zhang, R. Yokoyama, H. Kondo, M. Kanematsu and H. Hoshi, "Constructing a Probabilistic Model for Automated Liver Region Segmentation Using Non-contrast X-Ray Torso CT images", R. Larsen, M. Nielsen and J. Sporring (Editors), *Medical Image Computing and Computer-Assisted Intervention*, Copenhagen, 2006, Vol. 4191 of *Lecture Notes in Computer Science*, pp. 856–863, Springer Berlin / Heidelberg, Berlin, 2006.

8. Slagmolen, P., A. Elen, D. Seghers, D. Loeckx, F. Maes and K. Haustermans, "Atlas based liver segmentation using nonrigid registration with a B-spline transformation model", M. Styner, B. v. Ginneken and T. Heimann (Editors), *Proceedings of Medical Image Computing and Computer-Assisted Intervention Workshop 3D Segmentation in the Clinic: A Grand Challenge*, Brisbane, Australia, 2007, pp. 135–142, 2007.

9. Linguraru, M. G., Z. Li, F. Shah, S. Chin and R. M. Summers, "Automated Liver Segmentation using a Normalized Probabilistic Atlas", *Medical Imaging 2009 Biomedical Applications in Molecular Structural and Functional Imaging*, Vol. 7262, pp. 1–8, The International Society for Optical Engineering, 2009.

10. Hounsfield, G. N., "Computed medical imaging", *Science*, Vol. 210, pp. 22–28, 1980.

11. Wimmer, A., J. Hornegger and G. Soza, "Implicit active shape model employing boundary classifier", M. Ejiri, R. Kasturi and G. S. di Baja (Editors),

International Conference on Pattern Recognition, Florida, USA, 2008, Vol. 1–6, pp. 1–4, IEEE press, New York, 2008.

12. van Ginneken, B., T. Heimann and M. Styner, "3D Segmentation in the Clinic: A Grand Challenge", M. Styner, B. v. Ginneken and T. Heimann (Editors), *Proceedings of Medical Image Computing and Computer-Assisted Intervention Workshop 3D Segmentation in the Clinic: A Grand Challenge*, Brisbane, Australia, 2007, pp. 7–15, 2007.

13. Furukawa, D., A. Shimizu and H. Kobatake, "Automatic liver segmentation based on maximum a posterior probability estimation and level set method", M. Styner, B. v. Ginneken and T. Heimann (Editors), *Proceedings of Medical Image Computing and Computer-Assisted Intervention Workshop 3D Segmentation in the Clinic: A Grand Challenge*, Brisbane, Australia, 2007, pp. 117–124, 2007.

14. Tsai, D.-Y. and N. Tanahashi, "Neural-network-based boundary detection of liver structure in CT images for 3-D visualization", *IEEE International Conference on Neural Networks*, Florida, USA, 1994, Vol. 6, pp. 3484–3489, IEEE press, New York, 1994.

15. Garamendi, J., N. Malpica, J. Martel and E. Schiavi, "Automatic Segmentation of the Liver in CT Using Level Sets Without Edges", J. Martí, J. Benedí, A. Mendonça and J. Serrat (Editors), *3rd Iberian conference on Pattern Recognition and Image Analysis*, Girona, Spain, 2007, Vol. 4477 of *Lecture Notes in Computer Science*, pp. 161–168, Springer Berlin / Heidelberg, Berlin, 2007.

16. Massoptier, L. and S. Casciaro, "A new fully automatic and robust algorithm for fast segmentation of liver tissue and tumors from CT scans", *European Radiology*, Vol. 18, pp. 1658–1665, 2008.

17. Massoptier, L. and S. Casciaro, "Fully Automatic Liver Segmentation through

Graph-Cut Technique", *29th Annual International Conference of the IEEE Engineering in Engineering in Medicine and Biology Society*, Lyon, France, 2007, pp. 5243–5246, IEEE press, New York, 2007.

18. Lamecker, H., T. Lange and M. Seebass, *Segmentation of the Liver using a 3D Statistical Shape Model*, Tech. Rep. 04-09, Zuse-Institut Berlin, 2004.

19. Lee, J., N. Kim, H. Lee, J. B. Seo, H. J. Won, Y. M. Shin and Y. G. Shin, "Efficient liver segmentation exploiting level-set speed images with 2.5D shape propagation", M. Styner, B. v. Ginneken and T. Heimann (Editors), *Proceedings of Medical Image Computing and Computer-Assisted Intervention Workshop 3D Segmentation in the Clinic: A Grand Challenge*, Brisbane, Australia, 2007, pp. 189–196, 2007.

20. Zhang, X., J. Tian, K. Deng, Y. Wu and X. Li, "Automatic Liver Segmentation Using a Statistical Shape Model With Optimal Surface Detection", *IEEE Transactions on Biomedical Engineering*, Vol. 57, No. 10, pp. 2622–2626, 2010.

21. Erdt, M., M. Kirschner, S. Steger and W. Wesarg, "Fast automatic liver segmentation combining learned shape priors with observed shape deviation", *IEEE International Symposium on Computer-Based Medical Systems*, pp. 249–254, IEEE Computer Society Press, Los Alamitos, 2010.

22. Beck, A. and V. Aurich, "A hybrid approach for liver segmentation", M. Styner, B. v. Ginneken and T. Heimann (Editors), *Proceedings of Medical Image Computing and Computer-Assisted Intervention Workshop 3D Segmentation in the Clinic: A Grand Challenge*, Brisbane, Australia, 2007, pp. 225–234, 2007.

23. Cootes, T. F., C. J. Taylor, D. H. Cooper and J. Graham, "Active Shape Models-Their Training and Application", *Computer Vision and Image Understanding*, Vol. 61, No. 1, pp. 38–59, 1995.

24. Heimann, T., I. Wolf and H.-P. Meinzer, "Active Shape Models for a Fully Automated 3D Segmentation of the Liver - An Evaluation on Clinical Data", R. Larsen, M. Nielsen and J. Sporring (Editors), *Medical Image Computing and Computer-Assisted Intervention*, Copenhagen, Denmark, 2006, Vol. 4191 of *Lecture Notes in Computer Science*, pp. 41–48, Springer Berlin / Heidelberg, Berlin, 2006.

25. Heimann, T., H. P. Meinzer and I. Wolf, "A statistical deformable model for the segmentation of liver CT volumes", M. Styner, B. v. Ginneken and T. Heimann (Editors), *Proceedings of Medical Image Computing and Computer-Assisted Intervention Workshop 3D Segmentation in the Clinic: A Grand Challenge*, Brisbane, Australia, 2007, pp. 161–166, 2007.

26. Heimann, T., S. Münzing, H.-P. Meinzer and I. Wolf, "A Shape-Guided Deformable Model with Evolutionary Algorithm Initialization for 3D Soft Tissue Segmentation", N. Karssemeijer and B. Lelieveldt (Editors), *Information Processing in Medical Imaging*, Kerkrade, Netherlands, 2007, Vol. 4584 of *Lecture Notes in Computer Science*, pp. 1–12, Springer Berlin / Heidelberg, Berlin, 2007.

27. Kainmueller, D., T. Lange and H. Lamecker, "Shape constrained automatic segmentation of the liver based on a heuristic intensity model", M. Styner, B. v. Ginneken and T. Heimann (Editors), *Proceedings of Medical Image Computing and Computer-Assisted Intervention Workshop 3D Segmentation in the Clinic: A Grand Challenge*, Brisbane, Australia, 2007, pp. 109–116, 2007.

28. Okada, T., R. Shimada, Y. Sato, M. Hori, K. Yokota, M. Nakamoto, Y.-W. Chen, H. Nakamura and S. Tamura, "Automated Segmentation of the Liver from 3D CT Images Using Probabilistic Atlas and Multi-level Statistical Shape Model", N. Ayache, S. Ourselin and A. Maeder (Editors), *Medical Image Computing and Computer-Assisted Intervention*, Brisbane, Australia, 2007, Vol. 4791 of *Lecture Notes in Computer Science*, pp. 86–93, Springer Berlin /

Heidelberg, Berlin, 2007.

29. Okada, T., K. Yokota, M. Hori, M. Nakamoto, H. Nakamura and Y. Sato, "Construction of Hierarchical Multi-Organ Statistical Atlases and Their Application to Multi-Organ Segmentation from CT Images", D. Metaxas, L. Axel, G. Fichtinger and G. Széely (Editors), *Medical Image Computing and Computer-Assisted Intervention*, New York, USA, 2008, Vol. 5241 of *Lecture Notes in Computer Science*, pp. 502–509, Springer Berlin / Heidelberg, Berlin, 2008.

30. Montagnat, J. and H. Delingette, "Volumetric medical images segmentation using shape constrained deformable models", J. Troccaz, E. Grimson and R. Mösges (Editors), *Computer Vision, Virtual Reality and Robotics in Medicine and Medical Robotics and Computer-Assisted Surgery*, Grenoble, France, 1997, Vol. 1205 of *Lecture Notes in Computer Science*, pp. 13–22, Springer Berlin / Heidelberg, Berlin, 1997.

31. Saddi, K., C. Chefd'hotel, M. Rousson and F. Cheriet, "Region-Based Segmentation via Non-Rigid Template Matching", *11th IEEE International Conference on Computer Vision*, Rio de Janerio, Brazil, 2007, Vol. 1–6, pp. 2527–2533, IEEE press, New York, 2007.

32. van Ginneken, B., A. F. Frangi, J. J. Staal, B. M. ter Haar Romeny and M. A. Viergever, "Active shape model segmentation with optimal features.", *IEEE Transactions on Medical Imaging*, Vol. 21, No. 8, pp. 924–933, 2002.

33. Li, K., X. Wu, D. Z. Chen and M. Sonka, "Optimal Surface Segmentation in Volumetric Images-A Graph-Theoretic Approach", *IEEE Transactions on Pattern Analysis and Machine Intelligence*, Vol. 28, No. 1, pp. 119–134, 2006.

34. Seghers, D., P. Slagmolen, Y. Lambelin, J. Hermans, F. Maes and P. Suetens, "Landmark based liver segmentation using local shape and local intensity

models", M. Styner, B. v. Ginneken and T. Heimann (Editors), *Proceedings of Medical Image Computing and Computer-Assisted Intervention Workshop 3D Segmentation in the Clinic: A Grand Challenge*, Brisbane, Australia, 2007, pp. 135–142, 2007.

35. Ling, H., S. Zhou, Y. Zheng, B. Georgescu, M. Suehling and D. Comaniciu, "Hierarchical, learning-based automatic liver segmentation", *IEEE Conference on Computer Vision and Pattern Recognition*, Anchorage, USA, 2008, Vol. 1–12, pp. 405–412, IEEE press, New York, 2008.

36. Zheng, Y., A. Barbu, B. Georgescu, M. Scheuering and D. Comaniciu, "Fast Automatic Heart Chamber Segmentation from 3D CT Data Using Marginal Space Learning and Steerable Features", *IEEE 11th International Conference on Computer Vision*, Rio de Janerio, Brazil, 2007, Vol. 1–6, pp. 762–769, IEEE press, New York, 2007.

37. Caselles, V., R. Kimmel and G. Sapiro, "Geodesic Active Contours", *International Journal Of Computer Vision*, Vol. 22, No. 1, pp. 61–79, 1997.

38. Osher, S. and J. A. Sethian, "Fronts Propagating with Curvature-Dependent Speed: Algorithms Based on Hamilton-Jacobi Formulations", *Journal of Computational Physics*, Vol. 79, No. 1, pp. 12–49, 1988.

39. Leventon, M. E., W. E. L. Grimson and O. Faugeras, "Statistical shape influence in geodesic active contours", *IEEE Conference on Computer Vision and Pattern Recognition*, Hilton Head Island, USA, 2000, Vol. 1, pp. 316–323, IEEE Computer Society press, Los Alamitos, 2000.

40. Tsai, A., A. Yezzi, W. Wells, C. Tempany, D. Tucker, A. Fan, W. E. Grimson and A. Willsky, "A shape-based approach to the segmentation of medical imagery using level sets.", *IEEE Transactions on Medical Imaging*, Vol. 22, No. 2, pp. 137–154, 2003.

41. Rousson, M., N. Paragios and R. Deriche, "Implicit Active Shape Models for 3D Segmentation in MR Imaging", C. Barillot, D. Haynor and P. Hellier (Editors), *Medical Image Computing and Computer-Assisted Intervention*, Rennes, France, 2004, Vol. 3216 of *Lecture Notes in Computer Science*, pp. 209–216, Springer Berlin / Heidelberg, Berlin, 2004.

42. Charpiat, G., O. Faugeras, R. Keriven and O. G. C. O. Faugeras, "Approximations of Shape Metrics and Application to Shape Warping and Empirical Shape Statistics", *Foundations of Computational Mathematics*, Vol. 5, No. 1, pp. 1–58, 2004.

43. Cremers, D., S. Osher and S. Soatto, "Kernel Density Estimation and Intrinsic Alignment for Shape Priors in Level Set Segmentation", *International Journal of Computer Vision*, Vol. 69, No. 3, pp. 335–351, 2006.

44. Dambreville, S., Y. Rathi and A. Tannenbaum, "A Framework for Image Segmentation Using Shape Models and Kernel Space Shape Priors", *IEEE Transactions on Pattern Analysis and Machine Intelligence,*, Vol. 30, No. 8, pp. 1385–1399, 2008.

45. Saddi, K., M. Rousson, C. Chefd'hotel and F. Cheriet, "Global-to-Local Shape Matching for Liver Segmentation in CT Imaging", M. Styner, B. v. Ginneken and T. Heimann (Editors), *Proceedings of Medical Image Computing and Computer-Assisted Intervention Workshop 3D Segmentation in the Clinic: A Grand Challenge*, Brisbane, Australia, 2007, pp. 207–214, 2007.

46. Wimmer, A., G. Soza and J. Hornegger, "Two-stage semi-automatic organ segmentation framework using radial basis functions and level sets", M. Styner, B. v. Ginneken and T. Heimann (Editors), *Proceedings of Medical Image Computing and Computer-Assisted Intervention Workshop 3D Segmentation in the Clinic: A Grand Challenge*, Brisbane, Australia, 2007, pp. 179–188, 2007.

47. Wimmer, A., G. Soza and J. Hornegger, "A Generic Probabilistic Active Shape Model for Organ Segmentation", G.-Z. Yang, D. Hawkes, D. Rueckert, A. Noble and C. Taylor (Editors), *Medical Image Computing and Computer-Assisted Intervention*, London, UK, 2009, Vol. 5762 of *Lecture Notes in Computer Science*, pp. 26–33, Springer Berlin / Heidelberg, Berlin, 2009.

48. Song, Y., A. Bulpitt and K. Brodlie, "Liver Segmentation Using Automatically Defined Patient Specific B-Spline Surface Models", G.-Z. Yang, D. Hawkes, D. Rueckert, A. Noble and C. Taylor (Editors), *Medical Image Computing and Computer-Assisted Intervention*, London, UK, 2009, Vol. 5762 of *Lecture Notes in Computer Science*, pp. 43–50, Springer Berlin / Heidelberg, Berlin, 2009.

49. Florin, C., N. Paragios, G. Funka-Lea and J. Williams, "Liver Segmentation Using Sparse 3D Prior Models with Optimal Data Support", N. Karssemeijer and B. Lelieveldt (Editors), *Information Processing in Medical Imaging*, Kerkrade, Netherlands, 2007, Vol. 4584 of *Lecture Notes in Computer Science*, pp. 38–49, Springer Berlin / Heidelberg, Berlin, 2007.

50. Li, C., X. Wang, S. Eberl, M. Fulham, Y. Yin and D. Feng, "Fully automated liver segmentation for low- and high- contrast CT volumes based on probabilistic atlases", *17th IEEE International Conference on Image Processing*, Hong Kong, China, 2010, pp. 1733–1736, IEEE press, New York, 2010.

51. Greig, D. M., B. T. Porteous and A. H. Seheult, "Exact Maximum A Posteriori Estimation for Binary Images", *Journal of the Royal Statistical Society, Series B (Methodological)*, Vol. 51, No. 2, pp. 271–279, 1989.

52. Beichel, R., C. Bauer, A. Bornik, E. Sorantin and H. Bischof, "Liver segmentation in CT data: A segmentation refinement approach", M. Styner, B. v. Ginneken and T. Heimann (Editors), *Proceedings of Medical Image Computing and Computer-Assisted Intervention Workshop 3D Segmentation in the Clinic: A Grand Challenge*, Brisbane, Australia, 2007, pp. 235–245, 2007.

53. Shimizu, A., K. Nakagomi, T. Narihira, H. Kobatake, S. Nawano, K. Shinozaki, K. Ishizu and K. Togashi, "Automated Segmentation of 3D CT Images Based on Statistical Atlas and Graph Cuts", B. Menze, G. Langs, Z. Tu and A. Criminisi (Editors), *Medical Computer Vision, Recognition Techniques and Applications in Medical Imaging - International Medical Image Computing and Computer-Assisted Intervention Workshop*, Beijing, China, 2010, Vol. 6533 of *Lecture Notes in Computer Science*, pp. 214–223, Springer Berlin / Heidelberg, Berlin, 2011.

54. Freiman, M., O. Eliassaf, Y. Taieb, L. Joskowicz and J. Sosna, "A Bayesian Approach for Liver Analysis: Algorithm and Validation Study", D. Metaxas, L. Axel, G. Fichtinger and G. Széely (Editors), *Medical Image Computing and Computer-Assisted Intervention*, New York, USA, 2008, Vol. 5241 of *Lecture Notes in Computer Science*, pp. 85–92, Springer Berlin / Heidelberg, Berlin, 2008.

55. Pan, S. and B. M. Dawant, "Automatic 3D segmentation of the liver from abdominal CT images: a level-set approach", M. Sonka and K. M. Hanson (Editors), *Medical Imaging 2001: Image Processing*, Vol. 4322, pp. 128–138, The International Society for Optical Engineering, 2001.

56. Chan, T. and L. Vese, "Active contours without edges", *IEEE Transactions on Image Processing*, Vol. 10, No. 2, pp. 266–277, 2001.

57. Chi, Y., P. M. M. Cashman, F. Bello and R. I. Kitney, "A discussion on the evaluation of a new automatic liver volume segmentation method for specified CT image datasets", M. Styner, B. v. Ginneken and T. Heimann (Editors), *Proceedings of Medical Image Computing and Computer-Assisted Intervention Workshop 3D Segmentation in the Clinic: A Grand Challenge*, Brisbane, Australia, 2007, pp. 167–175, 2007.

58. Xu, C. and J. Prince, "Snakes, shapes, and gradient vector flow", *IEEE*

Transactions on Image Processing, Vol. 7, No. 3, pp. 359–369, 1998.

59. Kohlberger, T., M. Uzunbaş, C. Alvino, T. Kadir, D. Slosman and G. Funka-Lea, "Organ Segmentation with Level Sets Using Local Shape and Appearance Priors", G.-Z. Yang, D. Hawkes, D. Rueckert, A. Noble and C. Taylor (Editors), *Medical Image Computing and Computer-Assisted Intervention, MICCAI 2009*, London, UK, 2009, Vol. 5762 of *Lecture Notes in Computer Science*, pp. 34–42, Springer Berlin / Heidelberg, Berlin, 2009.

60. Ruskó, L., G. Bekes and M. Fidrich, "Automatic segmentation of the liver from multi- and single-phase contrast-enhanced CT images", *Medical Image Analysis*, Vol. 13, No. 6, pp. 871–882, 2009.

61. Susomboon, R., D. S. Raciu and J. Furst, "HepaTux-a semiautomatic liver segmentation system", M. Styner, B. v. Ginneken and T. Heimann (Editors), *Proceedings of Medical Image Computing and Computer-Assisted Intervention Workshop 3D Segmentation in the Clinic: A Grand Challenge*, Brisbane, Australia, 2007, pp. 151–160, 2007.

62. Gao, L., D. G. Heath, B. S. Kuszyk and E. K. Fishman, "Automatic liver segmentation technique for three-dimensional visualization of CT data.", *Radiology*, Vol. 201, No. 2, pp. 359–364, 1996.

63. Schmidt, G., M. A. Athelogou, R. Schönmeyer, R. Korn and G. Binnig, "Cognition network technology for a fully automated 3-D segmentation of liver", M. Styner, B. v. Ginneken and T. Heimann (Editors), *Proceedings of Medical Image Computing and Computer-Assisted Intervention Workshop 3D Segmentation in the Clinic: A Grand Challenge*, Brisbane, Australia, 2007, pp. 125–133, 2007.

64. Schenk, A., G. Prause and H.-O. Peitgen, "Efficient Semiautomatic Segmentation of 3D Objects in Medical Images", S. Delp, A. DiGoia and

B. Jaramaz (Editors), *Medical Image Computing and Computer-Assisted Intervention*, Pittsburgh, USA, 2000, Vol. 1935 of *Lecture Notes in Computer Science*, pp. 71–131, Springer Berlin / Heidelberg, Berlin, 2000.

65. Falcão, A. X., J. K. Udupa, S. Samarasekera, S. Sharma, B. E. Hirsch and R. d. A. Lotufo, "User-steered image segmentation paradigms: live wire and live lane", *Graphical Models and Image Processing*, Vol. 60, No. 4, pp. 233–260, 1998.

66. Bishop, C. M., *Pattern Recognition and Machine Learning (Information Science and Statistics)*, Springer, New York, 2006.

67. Dempster, A. P., N. M. Laird and D. B. Rubin, "Maximum Likelihood from Incomplete Data via the EM Algorithm", *Journal of the Royal Statistical Society, Series B (Methodological)*, Vol. 39, No. 1, pp. 1–38, 1977.

68. Weickert, J., *Anisotropic Diffusion in Image Processing*, Teubner, Stuttgart, 1998.

69. Perona, P. and J. Malik, "Scale-space and edge detection using anisotropic diffusion", *IEEE Transactions on Pattern Analysis and Machine Intelligence*, Vol. 12, No. 7, pp. 629–639, 1990.

70. Weickert, J., "Coherence-Enhancing Diffusion Filtering", *International Journal of Computer Vision*, Vol. 31, No. 2–3, pp. 111–127, 1999.

71. Li, S., "Markov random field models in computer vision", J.-O. Eklundh (Editor), *3rd European Conference on Computer Vision*, Stockholm, Sweden, 1994, Vol. 801 of *Lecture Notes in Computer Science*, pp. 361–370, Springer Berlin / Heidelberg, Berlin, 1994.

72. Boykov, Y. and O. Veksler, "Graph Cuts in Vision and Graphics: Theories and Applications", N. Paragios, Y. Chen and O. Faugeras (Editors), *Handbook of Mathematical Models in Computer Vision*, chap. 5, pp. 79–96, Springer US, New

York, 2006.

73. Boykov, Y. and G. Funka-Lea, "Graph Cuts and Efficient N-D Image Segmentation", *International Journal of Computer Vision*, Vol. 70, No. 2, pp. 109–131, 2006.

74. Kass, M., A. Witkin and D. Terzopoulos, "Snakes: Active contour models", *International Journal of Computer Vision*, Vol. 1, No. 4, pp. 321–331, 1988.

75. Zhu, S. C. and A. Yuille, "Region competition: unifying snakes, region growing, and Bayes/MDL for multiband image segmentation", *IEEE Transactions on Pattern Analysis and Machine Intelligence*, Vol. 18, No. 9, pp. 884–900, 1996.

76. Mortensen, E. N. and W. A. Barrett, "Interactive Segmentation with Intelligent Scissors", *Graphical Models and Image Processing*, Vol. 60, No. 5, pp. 349–384, 1998.

77. Boykov, Y. and M.-P. Jolly, "Interactive graph cuts for optimal boundary and region segmentation of objects in N-D images", *8th IEEE International Conference on Computer Vision*, Vancouver, Canada, 2001, Vol. 1, pp. 105–112, IEEE Computer Society press, Los Alamitos, 2001.

78. Mumford, D. and J. Shah, "Optimal approximations by piecewise smooth functions and associated variational problems", *Communications on Pure and Applied Mathematics*, Vol. 42, No. 5, pp. 577–685, 1989.

79. Boykov, Y. and V. Kolmogorov, "Computing geodesics and minimal surfaces via graph cuts", *9th IEEE International Conference on Computer Vision*, Nice, France, 2003, Vol. 1, pp. 26–33, IEEE Computer Society press, Los Alamitos, 2003.

80. Boykov, Y., V. Kolmogorov, D. Cremers and A. Delong, "An Integral Solution to Surface Evolution PDEs via Geo-Cuts", *9th European Conference on*

Computer Vision, Graz, Austria, 2006, Vol. 3953 of *Lecture Notes in Computer Science*, pp. 409–422, Springer Berlin / Heidelberg, Berlin, 2006.

81. Ford, L. R. and D. R. Fulkerson, *Flows in Networks*, Princeton University Press, New Jersey, 1962.

82. Besag, J., "Spatial Interaction and the Statistical Analysis of Lattice Systems", *Journal of the Royal Statistical Society, Series B (Methodological)*, Vol. 36, No. 2, pp. 192–236, 1974.

83. Boykov, Y., O. Veksler and R. Zabih, "Markov random fields with efficient approximations", *IEEE Computer Society Conference on Computer Vision and Pattern Recognition*, Santa Barbara, USA, 1998, pp. 648–655, IEEE Computer Society press, Los Alamitos, 1998.

84. Soler, L., H. Delingette, G. Malandain, J. Montagnat, N. Ayache, C. Koehl, O. Dourthe, B. Malassagne, M. Smith, D. Mutter and J. Marescaux, "Fully automatic anatomical, pathological, and functional segmentation from CT scans for hepatic surgery", *Computer Aided Surgery*, Vol. 6, No. 3, pp. 131–142, 2001.

85. Artaechevarria, X., A. Munoz-Barrutia and C. Ortiz-de Solorzano, "Combination Strategies in Multi-Atlas Image Segmentation: Application to Brain MR Data", *IEEE Transactions on Medical Imaging*, Vol. 28, No. 8, pp. 1266–1277, 2009.

86. Sethian, J. A., *Level Set Methods and Fast Marching Methods: Evolving Interfaces in Computational Geometry, Fluid Mechanics, Computer Vision, and Materials Science*, 2 edn., Cambridge University Press, Cambridge, 1999.

87. de Bruijne, M., B. van Ginneken, M. Viergever and W. Niessen, "Adapting Active Shape Models for 3D Segmentation of Tubular Structures in Medical Images", C. Taylor and J. Noble (Editors), *Information Processing in Medical*

Imaging, Ambleside, UK, 2003, Vol. 2732 of *Lecture Notes in Computer Science*, pp. 136–147, Springer Berlin / Heidelberg, Berlin, 2003.

88. Gorelick, L., M. Galun, E. Sharon, R. Basri and A. Brandt, "Shape Representation and Classification Using the Poisson Equation", *IEEE Transactions on Pattern Analysis and Machine Intelligence*, Vol. 28, No. 12, pp. 1991–2005, 2006.

89. Cahill, N., G. Vesom, L. Gorelick, J. Brady, J. Noble and J. Brady, "Investigating implicit shape representations for alignment of livers from serial CT examinations", *5th IEEE International Symposium on Biomedical Imaging: From Nano to Macro*, Paris, France, 2008, Vol. 1–4, pp. 776–779, IEEE press, New York, 2008.

90. Song, Z., N. J. Tustison, B. B. Avants and J. C. Gee, "Integrated Graph Cuts for Brain MRI Segmentation", R. Larsen, M. Nielsen and J. Sporring (Editors), *Medical Image Computing and Computer-Assisted Intervention*, Copenhagen, Denmark, 2006, Vol. 4191 of *Lecture Notes in Computer Science*, pp. 831–838, Springer Berlin / Heidelberg, Berlin, 2006.

91. Boykov, Y. and V. Kolmogorov, "An experimental comparison of min-cut/max-flow algorithms for energy minimization in vision", *IEEE Transactions on Pattern Analysis and Machine Intelligence*, Vol. 26, No. 9, pp. 1124–1137, 2004.

92. Dawant, B., R. Li, B. Lennon and S. Li, "Semi-automatic segmentation of the liver and its evaluation on the MICCAI 2007 grand challenge data set", M. Styner, B. v. Ginneken and T. Heimann (Editors), *Proceedings of Medical Image Computing and Computer-Assisted Intervention Workshop 3D Segmentation in the Clinic: A Grand Challenge*, Brisbane, Australia, 2007, pp. 215–221, 2007.